Exploration of Small Peptide Binding Interactions with Inorganic Surfaces Across Timescales

Rachel Nicole Gebhart

A dissertation

submitted in partial fulfillment of the

requirements for the degree of

Doctor of Philosophy

University of Washington

2020

Reading Committee:

Gary Drobny, Chair

Robert Synovec

Jim Pfaendtner

Program Authorized to Offer Degree:

Chemistry

University of Washington

Abstract

Exploration of Small Peptide Binding Interactions with Inorganic Surfaces Across Timescales

Rachel Nicole Gebhart

Chair of the Supervisory Committee:
Professor Gary Drobny
Chemistry

Peptide adhesion presents a novel method of binding surfaces which could not otherwise be permanently bound through conventional methods. Two such surfaces of practical interest are titanium dioxide (the surface of osseous implants) and hydroxyapatite (the primary mineral component of bone). The work described in this thesis strives to ascertain whether or not peptide adhesion could provide a more reliable bond between these through surfaces. In order to answer this question, research within this volume is performed to understand what features of peptides make them amenable to certain surfaces. In this work, two peptides are studied to determine their mode of selective binding to these surfaces. Titanium Binding Peptide (TBP) is investigated for its ability to bind to various surfaces through binding isotherms, and its mode of binding is interrogated through mutation studies, solid state NMR, DEST, NOSEY, and STD-

NMR experiments. Likewise, the α-1 fragment of osteocalcin was investigated via binding isotherms for its ability to bind to both hydroxyapatite and titania, and its method of binding to the later was studied through solid state NMR in order to determine a free and bound structure. From these structures, we used our chemical intuition to deduce a likely candidate for a binding motif.

TABLE OF CONTENTS

LIST OF FIGURES

LIST OF TABLES

List of Abbreviations

CP: Cross Polarization

CS: Chemical Shift

CSA: Chemical Shift Anisotropy

ΔCS: Change in Chemical Shift

DARR: Dipolar Assisted Rotational Recoupling

DCM: Dichloromethane

DFT: Density Functional Theory

DEST: Dark state Exchange Saturation Transfer spectroscopy

dhOC-α_1: α_1 fragment of the decarboxylated Osteocalcin protein

DIC: Diisopropylcarbodiimide

DLS: Dynamic Light Scattering

DMF: Dimethyl formamide

ESI: Electron Spray Ionization

FID: Fourier Induction Decay

FMOC: Fluorenylmethyloxycarbonyl

HAP: Hydroxyapatite

HCl: Hydrochloric Acid

hOC- α_1: α_1 fragment of the carboxylated Osteocalcin protein

HPLC: High Performance Liquid Chromatography

MAS: Magic Angle Spinning

MS: Mass Spectrometry

NMR: Nuclear Magnetic Resonance

NOESY: Nuclear Overhauser Effect SpectroscopY

ppm: Parts per Million

RF: Radiofrequency

RGD: arginine-glycine-aspartic acid peptide

ssNMR: Solid State NMR

STD-NMR: Saturation Transfer Difference NMR, technique

TBP: Titania Binding Peptide

TBP-D: TBP-6 with 99% ^{13}C isotopically enriched glutamic acid

TBP-D2A: RKLPAA

TBP-K: TBP-6 with 99% ^{13}C isotopically enriched glycine

TBP-K2A: RALPDA

TBP-P4A: RLKADA

TBP-R: TBP-6 with 99% ^{13}C isotopically enriched arginine

TBP-R2A: AKLPDA

TFA: Trifluoroacetic acid

TiBALDH:

TOCSY: TOtal Correlational SpectroscopY

UV: Ultraviolet light

ACKNOWLEDGEMENTS

Graduate school is never easy, but I have to extend a heartfelt thanks to everyone who made it more manageable. First and foremost, Gary: you welcomed me into the group with the most unusual threat, and I appreciate that this plague has not forced you to follow through on it. Thank you for pushing me to be a better and more accountable researcher, and to come to meetings prepared. Adrienne: I have no idea where I would be without your helping hand and constant questioning looks. You've been the steady rock that has seen me through this entire journey - ups and downs, beginning to end. To my family: you've asked me to justify every twist and turn in my academic career, and I can't thank you enough for forcing that conversation. Yes, I know I'm still in school and unmarried, but one of those things will be changing soon. Erika, Mengjun, Helen, Steve, and Prashant: thank you for showing me the ropes and answering my barrage of sometimes uninformed questions and listening to me on my bad days. Lizzy: your MRS solidarity has been invaluable, and sometimes the only thing keeping me sane. To the Washington hiker community: I was once given the advice to find one thing that I love and never stop doing it. Thank you for helping me take that advice. To the herding community: who would have thought that the best career advice I could get would be to get a working breed dog? You've taught me so much about what it's like to live outside the Ivory Tower, how to embrace personal growth, and have lent me some truly monumental friendships. Thank you to Toni in particular for giving me the confidence to believe I'm employable. Jen, thank you for reminding me to breathe, watch my body language, and show outwardly that I am enjoying what I'm doing. To my friends scattered across this country: thank you for listening to my various freak outs about graduate school, masked as freak outs about my dogs. Malcom and Zoe: thank you for humbling me every day and lighting

a fire under me to keep fighting to move forward to the next thing. You'll never read this, because you're both dogs, but know that all of those sucky nights in were me working hard for our better future together.

DEDICATION

To the pups. You're both going to be responsible for me needing knee replacements, so better I work on this problem now rather than waiting until it's too late.

Chapter 1. INTRODUCTION

1.1 SURFACE ADSORPTION

Broadly defined, surface adsorption of a protein or peptide is the non-penetrating adherence of the macromolecule to the exterior of a surface, typically dominated by electrostatic, ionic, and hydrophobic interactions.[1–3] The mechanism of this adherence is categorized as either cooperative or non-cooperative. Non-cooperative binding is the simplest theoretical mechanism, in which a peptide's binding sites adhere reversibly to a single binding site on the surface of a material. This one-to-one interaction is modeled computationally via the Langmuir Isotherm model, and assumes a large excess of ligand.[4] The fractional occupancy of this type of binding can be computationally determined as shown in Equation 1.1:

$$f_L = \frac{[L]}{K_D + [L]} \quad (1.1)$$

Where f_L is the fractional occupancy, *[L]* is the concentration of the ligand – which is often synonymous with the peptide throughout this thesis – and K_D is the dissociation constant, which can be calculated by comparing the concentration of free ligand [L] and binding site [S] to the population of bound ensemble [LS]:

$$K_D = \frac{[L][S]}{[LS]} \quad (1.2)$$

Cooperative binding, as the name implies, proceeds by recruitment of multiple peptides to a single binding site, either by forming peptide bundles which together form a binding domain, or on the surface where bound peptides actively recruit other free molecules to adhere to the surface. This interaction is typically captured and modeled by the Hill Equation, as shown in Equation 1.3.[5]

$$f_H = \frac{[L]^n}{K_D^n + [L]^n} \quad (1.3)$$

The Hill Equation most noticeably differs from the Langmuir Equation through the exponent of n, the Hill Constant. When n=1, there is no difference between the Hill and Langmuir equations. However, when n>1, there is a level of cooperativity, which suggests that the binding site has a higher level of binding affinity than a simple 1:1 mechanism. Visually, this difference in affinities can be seen in the transition of the plotted binding isotherm from a non-cooperative hyperbolic binding curve to a cooperative sigmoidal shape.

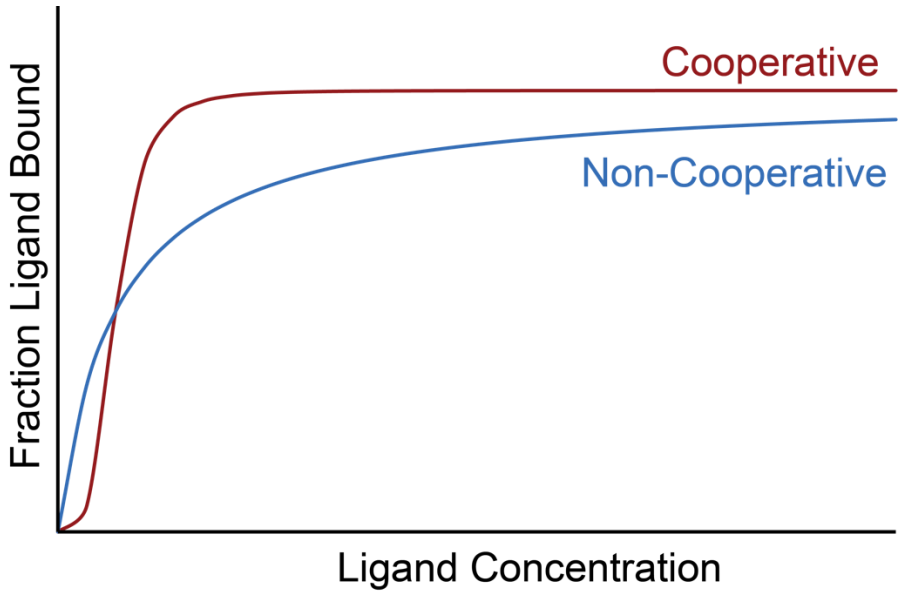

Figure 1-1: Illustration of isotherm plot behavior in the case of cooperative binding (red) and non-cooperative binding (blue). The cooperative isotherm is modeled through the Hill Equation (Equation 1.3) while the non-cooperative isotherm can be modeled using the Langmuir Isotherm Equation (Equation 1.1)

Which mechanism a particular peptide uses to adhere to a surface is dependent on a number of factors, including its stereochemistry and sequence, as well as the surface chemistry of the material it is binding to.[6] The following sections highlight the nuances and considerations involved in investigating peptides adsorbing to surfaces.

1.1.1 *Peptide Considerations*

Over the past few decades, much attention has been paid to the mechanisms of peptide-surface interactions, and particularly what parts of a peptide makes it amenable to mineral precursors and surface functional groups.[7–12] In particular, studies into the Sn15 peptide of the salivary protein Statherin, as well as the R5 fragment of the silicifying protein *sil1p* have helped elucidate the role that different classes of amino acid residues play in building binding domains within a protein, but our understanding of peptide interactions is not limited to just these studies.[1,8,9,13–18] Additionally, other binding surface-selective peptides such as titania binding peptide (TBP) and RGD integrin binding factors have been investigated, and theoretical studies of both capped and fragmented residues using both DFT and MD simulations have also weighed in on the issue of surface binding interactions.[3,19–23]

The culmination of these studies have painted a relatively straightforward picture of how proteins interact with surfaces, which is corroborated with basic chemical intuition. Polar residues such as arginine, lysine, glutamic acid, and aspartic acid show high affinity to surfaces with a non-zero surface charge, suggesting an electrostatic mechanism of interaction between these residues and charged surface functional groups on the surface.[24–26] Unsurprisingly, residues with multiple functional moieties show a larger binding affinity and greater free binding energy than those with fewer points of contact.[20,23] A large body of solid state Nuclear Magnetic Resonance (ssNMR), Molecular Dynamics (MD) studies of amino acids and their functional group analogues, solution Nuclear Magnetic Resonance (NMR) Dark State Exchange Saturation Transfer (DEST) experiments, and polypeptide adsorption studies have corroborated these findings.[8,9,21,23,27–35]

Hydrophobic packing has also been shown to play a role in how peptides bind, either due to hydrophobic regions providing local sites which minimize the free packing energy when filled

with a hydrophobic sidechain, by driving peptide bundling, which encourages cooperative peptide binding, or through pi-orbital stacking interactions with the polar surface.[36–39]

This bundling effect also highlights the importance of protein structure in its ability to adhere to a surface. Competing interactions between an attractive and repulsive sidechain in a protein with a functional group on the surface could reduce the binding energy, thereby driving down the kinetics of binding and preventing a protein from adhering to a surface. Therefore, favorable stereochemistry and the ability of a protein to facilitate structural reconfiguration as to allow a favorable binding interaction have been identified as a defining feature in these binding sequences. Proteins such as osteocalcin and statherin have been shown to pack in the presence of Ca^{2+}/Pb^{2+} ions and hydroxyapatite respectively to expose a binding domain.[40–42] Mutation studies of Titania Binding Peptide (TBP) have suggested the necessity of the proline residue in binding, which is assumed to force a steric constraint which facilitates the availability of binding residues at each end of the peptide to the surface at once.[20,22] The elongated, random structure of R5 allows it to coordinate readily with trimethyl silicate, allowing it to template and facilitate regular nucleation of silicon dioxide.

Together, these factors electrostatic, hydrophobic, and ionic-mediated binding interactions mesh seamlessly with our understanding of protein thermodynamics, organometallic interactions, and biochemistry, creating a compelling theory of how proteins and surfaces interface.

1.1.2 *Titanium Oxide*

Modern orthopedic and dental implants are predominantly comprised of titanium due to its lack of toxicity as well as its good mechanical properties.[43–45] This observed biocompatibility can largely be attributed to the TiO_2 oxide layer that forms on the oxygen-exposed surface of the metal.

Recently, titania has gained much attention for its catalytic properties as well as its applications in solar technologies.[46–51] Titanium dioxide (titania) naturally occurs in two crystallographic forms: anatase, and the more predominant rutile. For the purposes of this thesis, the following section will focus on the rutile phase of titania. Rutile titania forms a tetrahedral crystal structure, whose exposed face is comprised of two species of oxygen – neutral bridging oxygens, and terminal oxygen species as illustrated in Figure 1-2.[52]

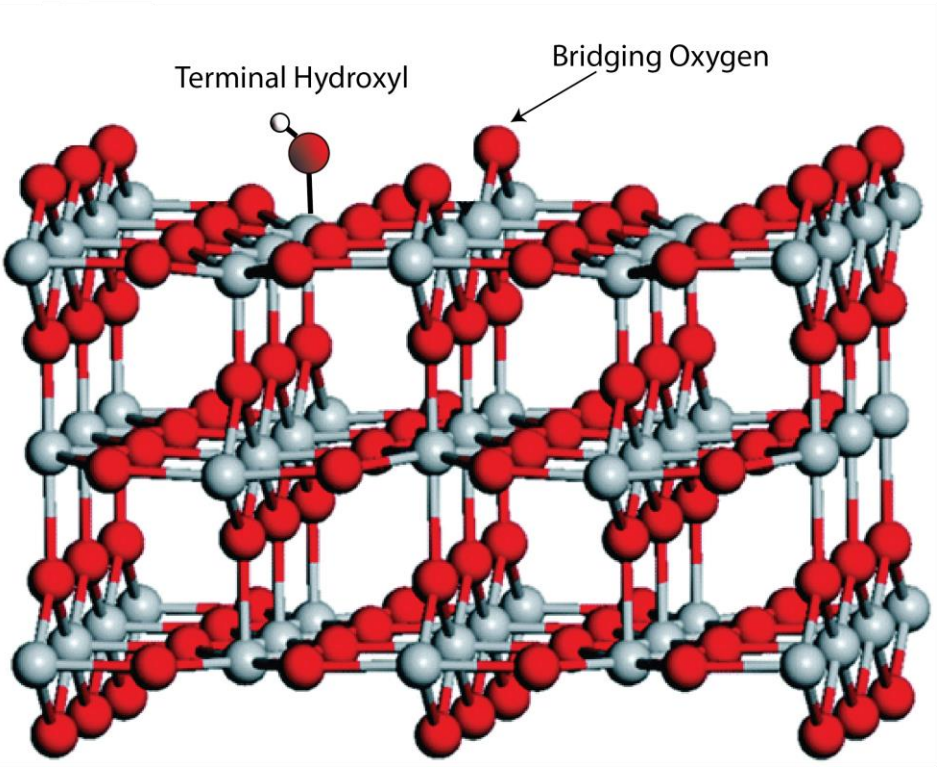

Figure 1-2. Visual representation of the surface of rutile titania. Red atoms represent oxygen species, grey atoms represent titanium, and white atoms represent hydrogens. The tetragonal structure exposes two species of oxygen atoms to the binding surface: bridging oxygens which connect two titanium atoms, and terminal hydroxyls deposited by exposure of water molecules.

While bridging oxygens occur as a result of the crystal lattice, surface hydroxyls are the result of ambient water adhesion.[53,54] These terminal hydroxyl species can take three forms: deprotonated (-1 charge), monoprotonated (+0 charge), and di-protonated (+1 charge).[55,56] All three species can

exist on the titania surface at any given time, but the negative zeta potential at neutral pH indicates that the deprotonated species is dominant in comparison to the di-protonated species. These theoretical assertions are supported by experimental work which gives evidence of the adsorption of both basic lysine and aspartic acid.[57,58] Through this framework, titania emerges as a complicated amphoteric surface which offers a wide range of potential binding sites to a peptide. Additionally, the oxides used in this study are high surface area nanoparticles, whose surface topography is riddled with pores and ridges, creating further pockets of surfaces which have additional inhomogeneity due to local curvature effects.[59,60] These pockets have been previously shown to influence peptide binding interactions.[61,62]

1.2 Nuclear Magnetic Resonance

First emerging in the first half of the 20th century, Nuclear Magnetic Resonance (NMR) has emerged as one of the most powerful tools available to chemists. Technological advances over the years have greatly simplified experimental setup, and streamlined acquisition, but have not in any way diminished the plethora of information contained within a single spectrum. In this section, two different classes of NMR experiments will be highlighted. The first class is solution state NMR experiments, in particular, Saturation Transfer Difference (STD), Nuclear Overhauser Effect SpectroscopY (NOESY), and Dark state Exchange Saturation Transfer (DEST) experiments. The second class is solid state experiments (ssNMR), which employ Cross Polarization (CP) and Magic Angle Spinning (MAS) techniques to improve the resolution of an otherwise ambiguous 2D correlational Dipolar Assisted Rotational Recoupling (DARR) spectrum.

1.2.1 *Basics of Spin Physics*

While a more expansive explanation of NMR theory can be found in multiple texts, the relevant basics are highlighted here.[63,64] Atomic composition determines fundamental properties of nuclei, such as their spin and associated dipole moment. Isotopes with a non-integer (n/2) nuclear spin (^{1}H, ^{13}C, ^{15}N, ^{31}P, etc.) possess a dipole moment which reacts much like a bar magnet would inside of a magnetic field. In standard benchtop conditions, the combination of a weak magnetic field from the earth, local electromagnetic fields from surrounding objects, intermolecular, and dynamic forces within a system randomizes these vectors. Summation of these moments would result in a null vector in a non-magnetic sample. However, when a strong, uniform magnetic field is applied by inserting a sample into the bore of an NMR, the dipole moments within these nuclei respond, and the bulk of the nuclear moment vectors aligns with the magnetic fields.

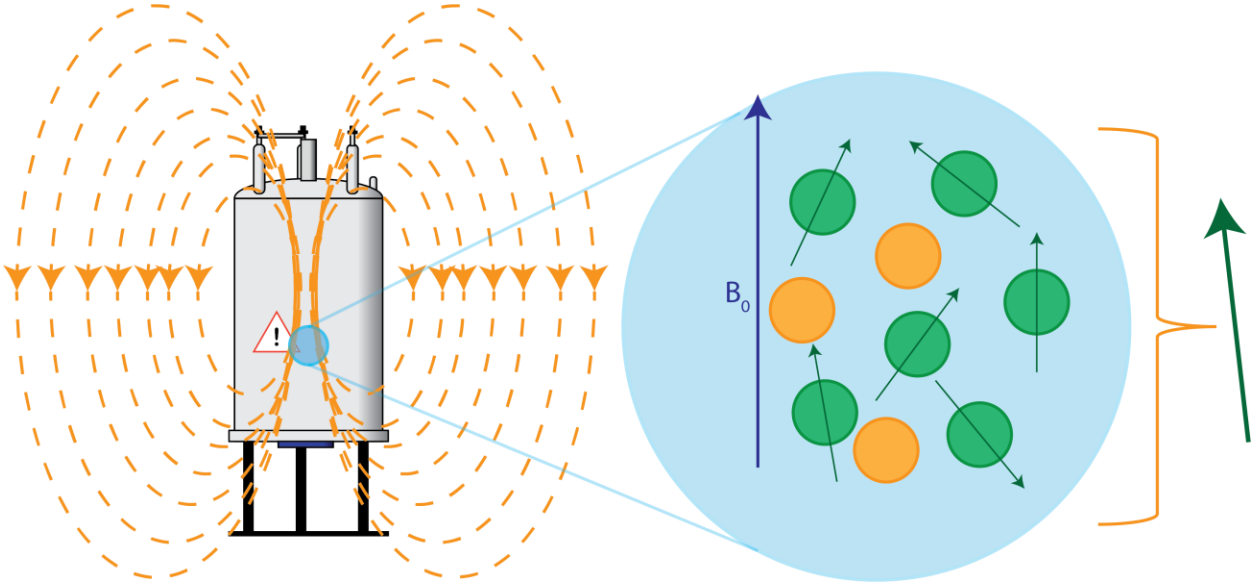

Figure 1-3: Schematic of nuclear reaction to an applied magnetic field. The B_0 field generated by the coil in the magnet points vertical along the Z axis, polarizing the nuclei within the sample along its gradient. This alignment is not perfect due to local steric and electrostatic interactions, but the sum of the induced magnetic moments generally falls along the B_0.

While this alignment is not perfect, the sum of nuclear moments within the sample does point in the general direction of the B_0 field supplied by the magnet, and is consequentially considered to be in alignment. Due to the nuclear spin, these nuclei precess around the center of the magnetic field at a frequency determined by its nuclear composition. When an RF field at a matched frequency is applied, these nuclei are rotated in accordance with the right hand rule.

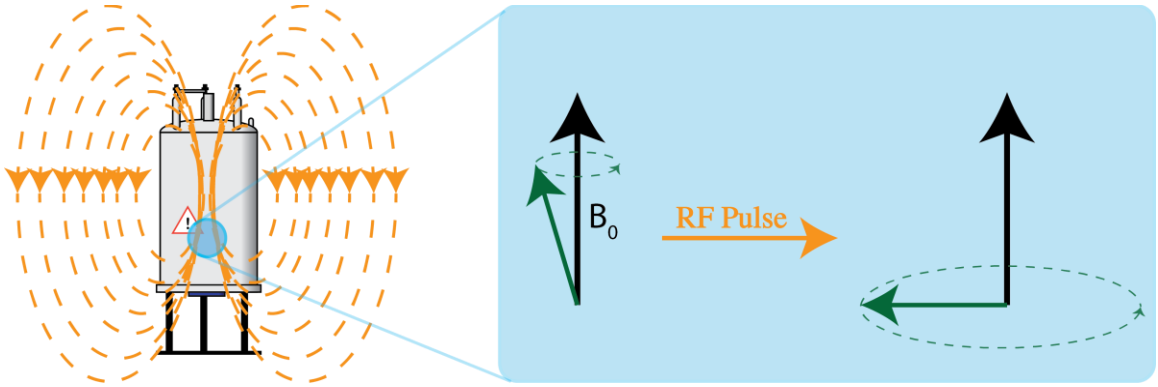

Figure 1-4. Illustration of the effect of frequency matched RF pulses on aligned nuclei.

In the most basic of NMR experiments, this method of rotating the bulk sum of nuclei is used to rotate the nuclei by a factor of pi/2, aligning the vector within the center of the receiving coil of the NMR probe. As the vector precesses, it generates an alternating current which can be detected by the electronic systems in the NMR console. After the RF pulse is turned off, the nuclei will relax to once again align with the B_0 field of the magnet, causing the generated signal within the coil to decrease over time. This generates a decaying signal profile, commonly referred to as a Free Induction Decay (FID).

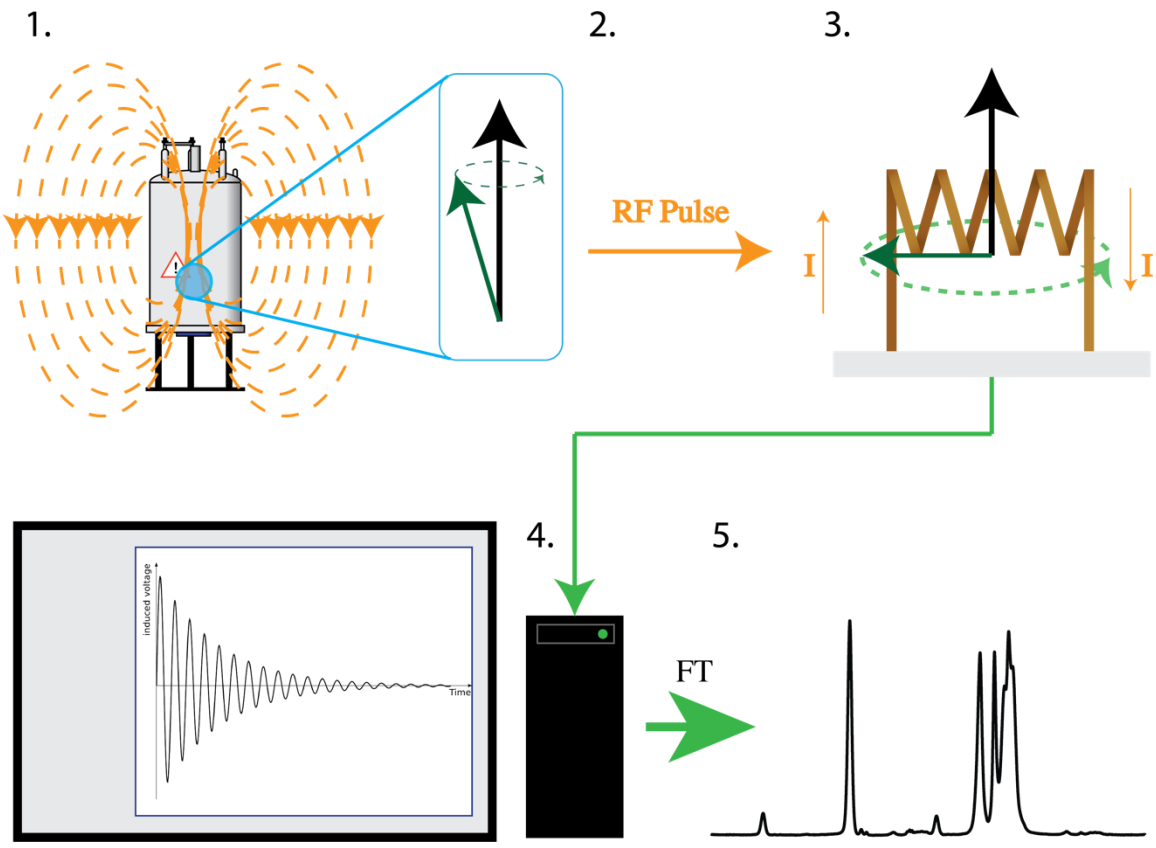

Figure 1-5. Illustration demonstrating the generation of a FID.

By applying a Fourier transform to the FID curve, a single Lorentzian peak is resolved for each contributing nuclei. In this experiment, if the acquisition window is focused on the frequency range associated with ^{13}C and a spectrum of glycine is recorded, two peaks will appear: the carbonyl carbon and the C_a.

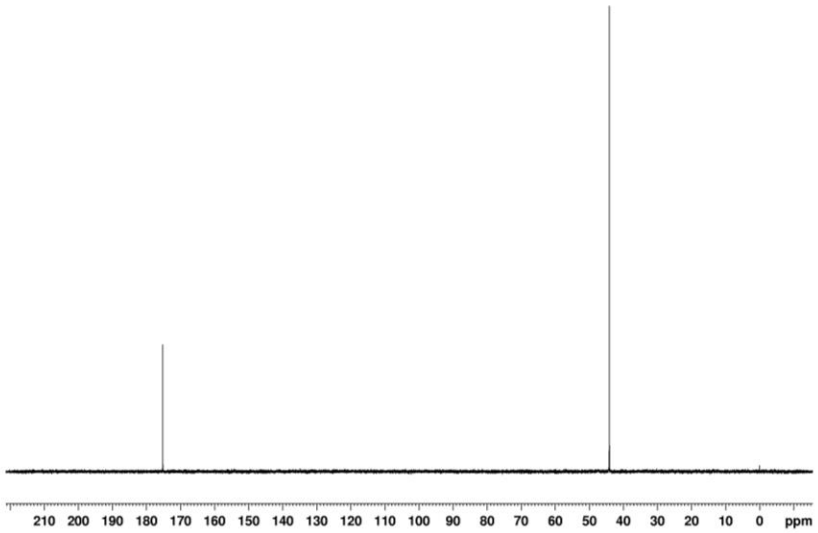

Figure 1-6. Neat ^{13}C liquids spectrum of glycine showing the ^{13}Co peak at 175 ppm and the $^{13}C\alpha$ peak at 43 ppm.

This experiment can be conducted for samples both in solution and in solid phase, however, the resulting spectra of these two classes of samples will look vastly different. Random motion of the sample molecules due to Brownian collisions with the solvent allows the molecules to be observed in multiple configurations, averaging out the dipolar and anisotropic effects which would be observable in a less mobile system. This averaging results in a very narrow Lorentzian lineshape which can be easily resolved from other peaks in the spectrum. The same sample recorded with the same experiment in the absence of solvent would produce a very wide powder pattern whose peaks are indistinguishable from one another. By varying the power, frequencies, and spacing, and number of pulses applied to a sample, a number of properties can be isolated and measured. The subsequent sections will discuss a number of experiments optimized for measuring samples in solution state (DIPSI, STD-NMR, NOSEY, and DEST) and in solid phase (CP-MAS, DARR).

1.2.2 *Chemical Shifts*

In order to interpret a spectrum, a standard system of referencing must be in place to allow for universal interpretation of data. Chemical shift is the unit of measurement choses by IUPAC for measuring the position of peaks within an NMR spectrum. Each peak generated by applying a Fourier transform to the recorded FID has a central maximum which is measured in units of frequency. This position is benchmarked against the frequency generated by a known standard such as trimethyl silane (TMS), and the difference in the two frequencies is divided by the resonant frequency to produce a chemical shift value measured in ppm as according to the following equation:

$$\delta\ (ppm) = \frac{\nu_{sample}(Hz) - \nu_{ref}(Hz)}{\nu_{resonant}\ (Hz)}$$

Assigning the chemical shifts of a spectrum allows for unique peak labeling as well as assignment within a molecule. Nuclei in different chemical environments experience the effects of an applied magnetic field differently due to the density of the electron cloud surrounding them. This electron cloud density has an inverse relationship to the effective local magnetic field, meaning that the more dense the molecular orbital around a nucleus, the less susceptible it is to perturbations from both the magnet field and the applied radio frequency pulses. This difference in susceptibility causes the nucleus to precess at a different rate, causing its peak position to be predictably different from other peaks. Tables of chemical shift ranges provide average chemical shift ranges for various functional groups, but accurate assignment is often accomplished through analyzing correlational spectra, and J-coupling where relevant.

1.2.3 *Solution NMR*

The following subsections specifically address experiments optimized for samples dissolved in an aqueous matrix which contains >10% deuterated matrix. These experiments are best performed on neat, soluble molecules which are not surface bound.

1.2.3.1 Correlational 2D Spectroscopy

While assignment of chemical shifts can lend a researcher much insight into the nature of a spectral peak, often times in larger molecules peaks are not well resolved from one another. A way to help unambiguously assign peaks would be to employ the use of 2D correlational spectra. This class of spectra uses a combination of preparation pulses and mixing periods to probe the correlation of spin systems either through space or through bond depending on the experiment. While heteronuclear and homonuclear experiments are both possible, the work in this thesis comprises of only homonuclear correlational experiments, specifically the TOtal Correlational SpectroscopY (TOCSY) experiment.[65] The pulse program for this experiment is outlined in Figure 1-7. Briefly, the nuclei are first aligned using a single $\frac{\pi}{2}$ pulse, and then allowed to evolve over a period of t_1. After the nulcei are allowed to evolve, a mixing pulse or sequence is applied. This period allows a transfer of magnetization between J-coupled nuclei. Unlike in the simpler COrrelational SpectroscopY (COSY) experiment which uses a single high powered pulse to transfer magnetization, the TOCSY experiment uses two lower powered pulses separated by a mixing time τ_{mix} in which an anisotropic mixing scheme is applied. This block, known as a TOCSY block, spin-locks the nuclei, allowing free transfer of magnetization between spatially proximal nuclei and results in cross peaks in the 2D spectrum as shown in Figure 1-7.

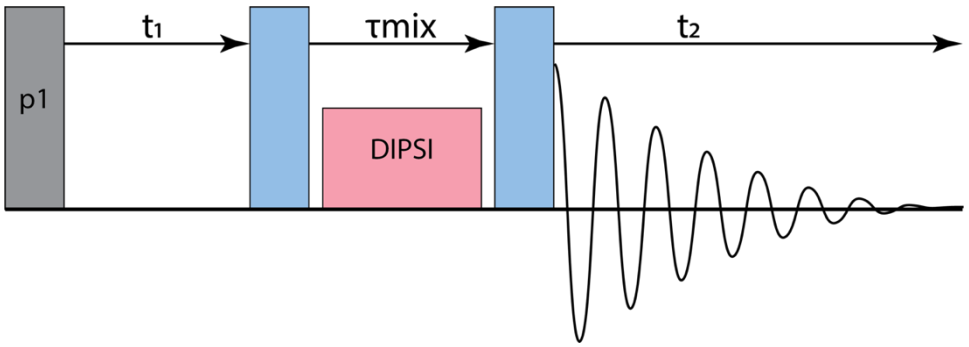

Figure 1-7. TOCSY pulse sequence.

The length of the mixing time τ_{mix} controls the distance on communication between nuclei – in other words, the longer the delay, the longer the more interactions between spin systems can be observed.

The result of this experiment is a 2D plot with units of ppm on the F1 and F2 axis. If sliced diagonally, this slice would look identical to the 1D spectrum. Any peak with significant intensity that appears anywhere off this diagonal is produced by the transfer of magnetization between two spatially proximal nuclei. By tracing these networks of cross peaks, each nuclei can be assigned to a particular peak in the spectrum, which allows the full, unambiguous assignment. Often times in aqueous NMR experiments in which a mix of deuterated and non-heavy water are used in combination, the resulting background water peak from the solvent overwhelms the signal of the ligand of interest. Throughout all solution NMR experiments, a Watergate solvent suppression pulse sequence was employed.[66]

1.2.3.2 Saturation Transfer Difference NMR

Employed widely across fields, Saturation Transfer Difference (STD) experiments measure the binding interactions between a small ligand (such as a peptide) and a larger system (such as a nanoparticle). Larger objects in solution are less effected by the battering effects driving Brownian

motion, and therefore tumble at a slower rate. This slow tumbling leads to increased relaxation (T_2) rates relative to smaller, more mobile molecules, which leads to dramatic peak broadening. Often, these peaks are so broad that they cannot be observed within the sweep width of a recorded spectrum. When the center of this peak is irradiated with an RF pulse of equal frequency, magnetization is transferred between nuclei in slow tumbling systems and nuclei proximal to them. The most direct way to measure what is binding to a larger structure would be to foster this transfer of magnetization between an opportune nucleus on the surface of a particle and a ligand molecule of interest. Unfortunately, candidate nuclei are often not available in inorganic nanoparticle systems, and if they are, their resonant frequencies are difficult to pin down. However, in aqueous systems, a polylayer of closely bound water molecules is known to bind to surfaces and molecules upon solvation, adopting the tumbling rate of the surface it is attached to. Because water is ubiquitous, readily adsorbs and desorbs, and exists in both a bound and free state, it is easy to determine the resonant frequency of water. Additionally, it is a reasonable assumption that the transfer of magnetization between a slowly tumbling molecule and a smaller ligand in solution is a communication between surface bound water and an adsorbing molecule, and any observed changes to the spectrum reflect surface binding.

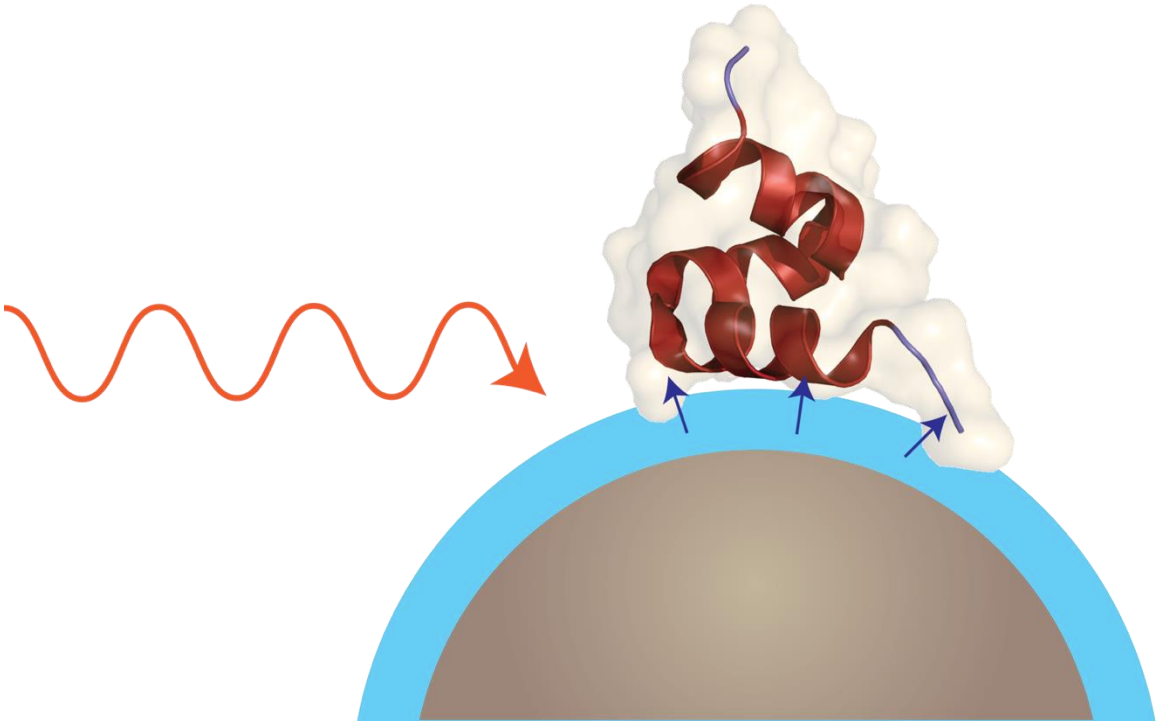

Figure 1-8. Cartoon of magnetization transfer between surface bound water and a peptide in the STD-NMR experiment.

As would be expected, this transfer of magnetization between slowly tumbling nuclei which are not visible in our experiments to fast tumbling nuclei which are visible as narrow peaks in these experiments causes a reduction in signal in the affected nuclei. Therefore, it is useful to capture two spectra: the first (S_0) with an irradiation pulse placed well off of the resonant frequency of water (60 ppm) and a second spectrum (S) with the RF pulse placed at the apex at the peak corresponding to mobile water (4.71 ppm). These two spectra capture the behavior of the system without a pulse perturbing the system directly, and one with a pulse transferring magnetization respectively. Differences in peak intensity caused by magnetic transfer are captured by subtracting the S spectrum from the S_0, and any peaks present in this difference spectrum indicate the transfer of magnetization due to the nucleus being close to the surface adsorbed water layer on the particle.

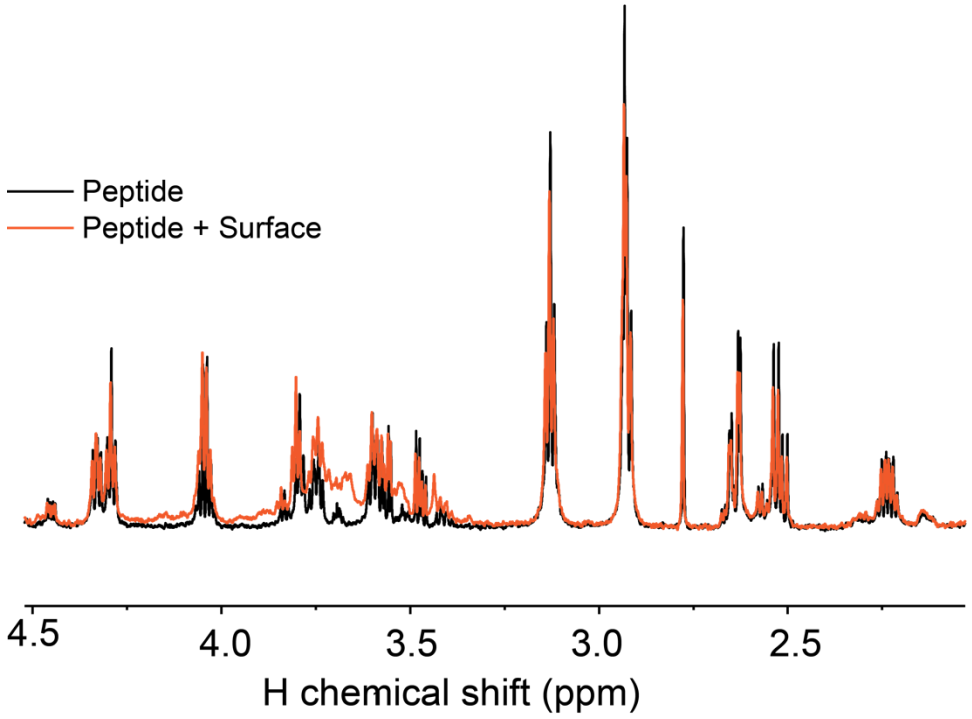

Figure 1-9. Example STD-NMR dataset.

Since the position of spectral peaks does not change as a result of these RF pulses, complete assignment of the 1D spectrum can be used to analyze which nuclei experience the effects of the particle and which nuclei do not. However, this technique does experience some limitations. Observation of these differences relies on the fast (μs timescale) exchange between a peptide ligand and a binding site on a much larger construct, meaning that this experiment only captures exchanges which fall within this kinetic range. In summary, differences between the two spectra in the STD-NMR experiment are attributed to their proximity to surface bound water. Differences are caused by interactions between ligands and the surface adsorbed water facilitated by the binding of the ligand to the surface.

1.2.3.3 Nuclear Overhouser Effect Spectroscopy

As can be inferred by the above discussion, no nucleus exists in a vacuum within a sample. Proximal nuclei (< 5 Å) interact with one another, coupling through dipolar interactions in a way

which affects the z-magnetization of the systems. This interaction, referred to as the Nuclear Overhouser Effect (NOE), can be measured using a class of 1D and 2D pulse programs. The work including within this thesis uses the 2D Nuclear Overhouser Effect SpectroscopY (NOESY) experiment, which generates a positive or negative crosspeaks on a 2D spectrum between nuclei which are interacting through dipolar coupling. While both a 1D NOE and 2D NOESY experiment exist, it is often advantageous to use the 2D version of this experiment for the same reason it is advantageous to use 2D coupling correlational experiments such as COSYs and TOCSYs – the increased dimension provides increased spectral resolution and aids in the interpretation of data.

The 2D NOSEY experiment looks very similar to the TOCSY pulse sequence (Figure 1-10). Unlike in the TOCSY pulse program, however, the nuclei are allowed to freely diffuse during the mixing time instead of being manipulated by a block of phase cycling.

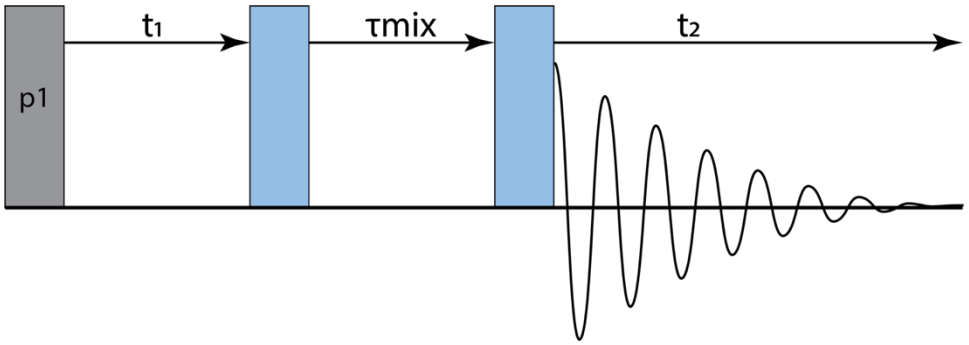

Figure 1-10 NOESY pulse sequence.

Unlike in through-bond correlational spectroscopy, NOSEY peaks can have both a positive and negative phase depending on how the spins of the nuclei change relative to their base states. Positive peaks typically correspond to immobilized ligands in contact with a slow-tumbling surface or aggregate, and are therefore considered to be indicative of surface binding interactions or sidechain packing. Conversely, negative peaks are typically seen in the case of small ligands

tumbling rapidly in solution, and are often attributed to fast motion of the observed nucleus. In structural biology, the strength of the cross peaks is assigned, which corresponds to a range of internuclear distances. These connections can be used as constraints in energy-minimization simulations, and can aid in deducing likely structural models for a given protein. In this thesis, cross peaks are used far more simplistically – their presence merely indicates a through-space interaction, and gives a qualitative measure of peptide folding. In summary, if there are no cross-peaks present on an NOESY spectrum, the peptide is considered to be random coil. However, if cross peaks are observed, the peptide is said to be folded.

1.2.3.4 Dark State Exchange Saturation Transfer

Dark state Exchange Saturation Transfer (DEST) experiments are another class of saturation transfer experiments closely related to STD-NMR experiments, but operate on a much longer exchange timescale of 500 μs – 1s.[67] As was previously discussed, when an object is large, it tumbles at a slow rate, broadening the signal produced by a given nucleus so much that it is unobservable within a 12ppm window. DEST capitalizes on this phenomenon: nuclei of the particle adhered to the larger particle tumble slowly and experience very little re-orientational movement, becoming ‘dark state’ nuclei. When these bound species which are saturated by a low-power radiofrequency pulse desorb from the particle, they retain these ‘dark state’ properties for a short period of time on par with the acquisition timeframe, causing an attenuation in signal.

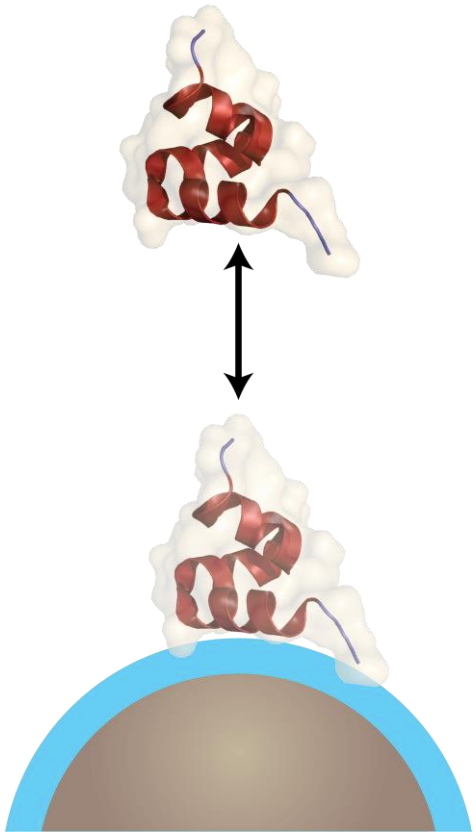

Figure 1-11. Simple peptide adsorption and desorption model from a nanoparticle surface. When the peptide in in contact with the surface, its binding regime adopts the local tumbling and relaxation rates of the solid nanoparticle. Upon desorption from the surface, these resonances will quickly adopt the tumbling rates of the free molecule. However, the application of an interacting radio frequency pulse can prolong the longevity of these effects, resulting in overall signal attenuation.

However, unlike in STD-NMR, the frequency required to saturate these species is unknown. During a DEST experiment, a large array of RF pulses is applied, starting well away from any potential resonant frequencies (-100 ppm), sweeping through 0ppm, and continuing symmetrically to a frequency which should no longer be exciting any resonances (+100 ppm). This procedure produces two spectra which should act as a control S_0, and several S spectra which experience signal attenuation. Peaks are assigned using 1D and 2D correlational spectroscopy, and the S/S_0 ratio of peak intensities are plotted as a function of frequency. This experiment is repeated for the

ligand without any system it can bind to, and the generated curves are then compared to one another.

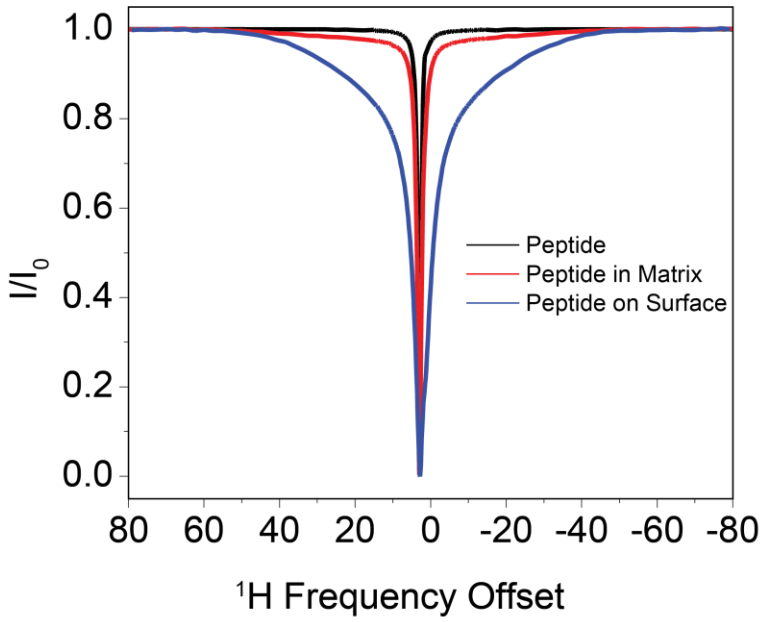

Figure 1-12. Example DEST profile of a nucleus binding to a surface. Three traces represent the peptide neat (black), within the supporting agarose matrix (red), and in the presence of an interacting surface (blue). The absence of a binding interaction between a peptide and the surface would produce a trace which does not broaden markedly in comparison to the neat peptide, such as the red trace. Conversely, a strong binding interaction would produce a significant broadening of the trace as is seen in blue. The slight asymmetry is due to Nuclear Overhauser (NOE) effects to proximal nuclei within the molecule.

If the ligand does not interact with the surface, the width of the inverted peak will be the same, showing that the ligand is only bound to a surface layer of water that adsorbs upon solvation. However, broadening of this signal would indicate that the ligand is binding more strongly to a larger system. The width of this peak can be used to qualitatively determine the strength of the binding site interaction: wider peaks correspond to a stronger surface interaction than a narrower peak. Quantitatively, the Bloch-McConnel equations can be used with an appropriate binding

model to calculate the binding constant of each binding nucleus. In summary, broadening of the DEST peak indicates that a particular nucleus on a ligand is experiencing slow relaxation due to its proximity to a surface, suggesting a binding interaction.

1.2.4 *Solid State NMR Experiments*

While understanding the free structure of peptides in solution is useful in many applications, the insoluble nature of surfaces and particles makes them non-ideal candidates for most solution state experiments which rely on a homogenous distribution of peptide through the sample chamber. Additionally, because many of the surfaces of interest are non-translucent and do not form a regular crystal pattern when mixed with a peptide, they are bad candidates for X-Ray Crystalography studies. For this reason, it is advantageous to have a class of experiments which operate in the absence of a solution matrix. These experiments are capable of directly probing the nature of static interactions between a solid surface and an adsorbed molecule. With the absence of solution comes a different set of sample acquisition considerations, some of which will be discussed in the following sections.

1.2.4.1 Magic Angle Spinning

Removing solution from a sample matrix removes the anisotropic, quadrapolar, and dipolar averaging effects lent by Brownian tumbling, rendering otherwise sharp peaks broad and irregular. The width of these peaks make them impossible to resolve from one another, and therefore impossible to assign or analyze. It therefore stands to reason that it would be important to find a way to re-introduce this averaging effect in order to make the data useful for analysis. To understand how it can be re-introduced, it is useful to first introduce the NMR Hamiltonian. This operator is constructed of two classes of sub-operators: external, and internal.

$$\widehat{H}_{NMR} = \widehat{H}_{internal} + \widehat{H}_{external}$$

While the external portion of the NMR Hamiltonian captures the effects of the magnetic field and the applied RF pulses, the internal portion of the NMR Hamiltonian captures the effects experienced by the observed nuclei during the NMR experiment. This sub-operator is constructed of five terms: chemical shift, dipole-dipole interactions (both short and long range), J-coupling, and quadripolar coupling.

$$\hat{H}_{internal} = \hat{H}_{CS} + \hat{H}_{Short\ Range\ Dipolar} + \hat{H}_{Long\ Range\ Dipolar} + \hat{H}_{J-Coupling} + \hat{H}_{Quadrapolar}$$

If we expand these terms, we discover that the dipolar and the anisotropic portion of the chemical shift terms have an angular dependence. The chemical shift operator contains an orientational term d_{ij} which describes the secular homonuclear dipolar interaction term, which has an orientational dependence.

$$\hat{H}_{Dipolar}(\Theta_{jk}) = \frac{b_{jk}}{2}(3\cos^2(\Theta_{jk}) - 1)(3\hat{I}_{jz}\hat{I}_{kz} - \hat{I}_j \cdot \hat{I}_k)$$

Therefore, by changing the angle of the sample such that the angular terms become zero, it is physically possible to annihilate this contribution. In specially fitted MAS probes, a sample is packed within a rotor, and inserted into the staedter which is either permanently fixed or pneumatically rotated to what is commonly referred to as the magic angle of 54.74°. The chemical shift Hamiltonian term does not have the same angular dependence, but rather is defined by a 3x3 tensor commonly referred to as the Chemical Shift Tensor. As has already been stated, molecular motion in solid powder samples is restricted due to the lack of solvent, which casts this tensor into an orientationally dependent operator, referred to as the chemical shift anisotropy (CSA) term.

$$\hat{H}_{CSA}(\Theta) = -\gamma_j B^0 \delta_{zz}^j(\Theta)\hat{I}_{jz}$$

In this equation, δ is the chemical shift tensor. Each crystal or adsorbed molecule within a sample may point in a different direction, and as would be suggested by this operator, this difference in

orientation would produce a different chemical shift. This variety of chemical shifts is what normally leads to a broad, multifeatured peak often referred to as a powder pattern.

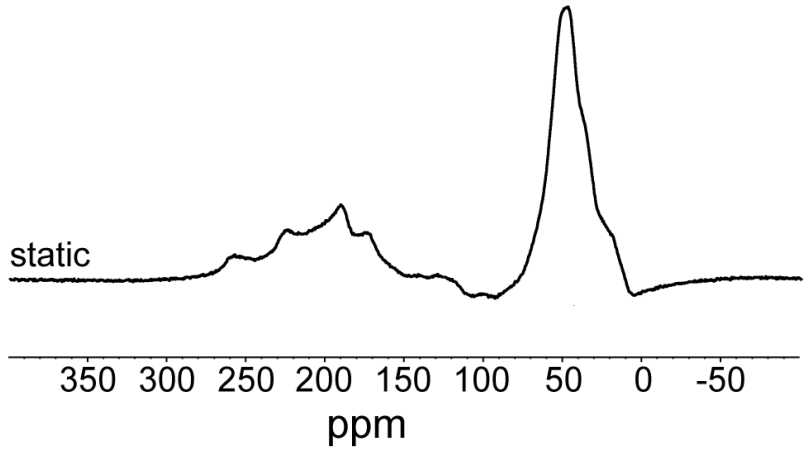

Figure 1-13. Static ^{13}C glycine spectrum recorded by Dr. Erika Buckle. Broad linewidths and multiple apexes show the resultant effects of removing the ability for the peptide to orientationally average by removing water.

By physically rotating the sample within the probe, the direction of the crystals change, and at sufficiently high spinning speeds, the nucleus will pass through multiple orientations during the acquisition periods much like what would happen in a liquid sample.[68,69] Increased sampling causes the average CSA value to be the predominant measurement in accordance with the law of large numbers, thereby causing the distribution of CS peaks to converge into a much narrower and more intense peak. The faster the rate of sample spin, the narrower and taller the peak, signaling that the CSA tensor has been more completely averaged.

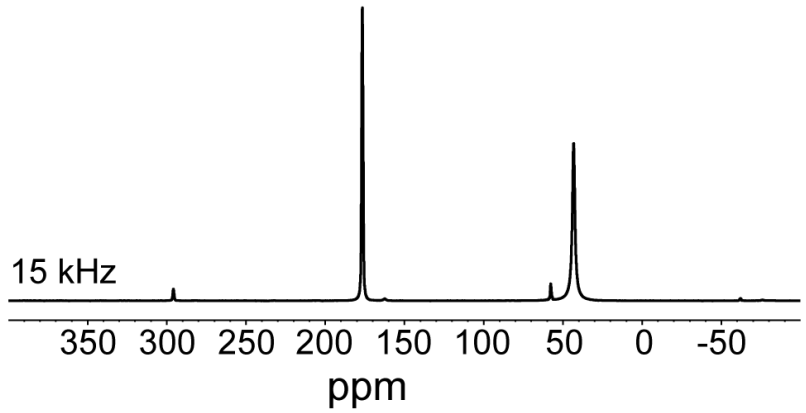

Figure 1-14. ^{13}C CP-MAS spectrum recorded by Dr. Erika Buckle of neat uniformly labeled glycine. Compared to Figure 1-13, the peaks have collapsed into two narrow resonances corresponding to the ^{13}Co and ^{13}Cα nuclei, and the peak widths have become much narrower.

The combination of both rotating the sample within the probe to the magic angle and spinning at speeds of 5 kHz and higher produces a peak shape that is Lorentzian, and far narrower than the powder pattern. This technique of solid sample manipulation is commonly referred to as Magic Angle Spinning (MAS). Even within a well shimmed magnet, the linewidth of a solid MAS peak will never approach that which would be produced within a solution state NMR experiment. However, these peaks generally are narrow enough to be resolved from one another in a small molecule or with the assistance of a 2D correlational experiment.

It should be noted that the quadripolar term in the NMR Hamiltonian also has an angular dependent term, however, none of the nuclei studied within this thesis have a significant quadripolar moment, and therefore does not require further discussion.

1.2.4.2 Cross Polarization

While MAS can greatly narrow the linewidth of a peak, increasing its intensity, often the nuclei of interest in solid state NMR (ssNMR) are those with magnetic susceptibility, and therefore do not

generate very strong peaks. In order to generate a usable amount of signal, many transients - or measurement repeats- are required, increasing the time and resources required to collect publishable data. Therefore, there is a clear need to develop a technique to increase the signal generated during these experiments.

Fortunately, there exist a readily available population of nuclei within most organic samples which are highly susceptible to the magnetic field and the RF pulses. Proton (^{1}H) are ubiquitous, have a gyromagnetic ratio γ of 26.7 $\frac{10^7 \text{rad}}{\text{s}*\text{T}}$, and a natural abundance of 99.99%. Comparatively, ^{13}C has a γ of 6.73 $\frac{10^7 \text{rad}}{\text{s}*\text{T}}$ and a natural abundance of 1.07%. While isotopic labeling of dilute nuclei such as ^{13}C can raise the population of magnetically susceptible nuclei, the lower in γ captures the inability of carbon to produce as much signal as hydrogen in the same conditions. γ is a fundamental property of the nucleus which is related to the splitting energy of a spin flip transition.

$$E_m = m\hbar\gamma B_0$$

Where m is the spin of the nucleus, B_0 is the field strength of the magnetic field, and $\hbar$ is the reduced Planck's constant. Because carbon and hydrogen have very different gyromagnetic ratios, they do not have the same transitional energy, and therefore they do not experience the effects of one another's spin transitions. However, if the processional rates of these two nuclei are made equal using a radiofrequency pulse, their transitional energies become normalized, and magnetic susceptibility is able to diffuse between the two populations. Figure 1-15 illustrates visually illustrates how this susceptibility is transferred between proximal populations.

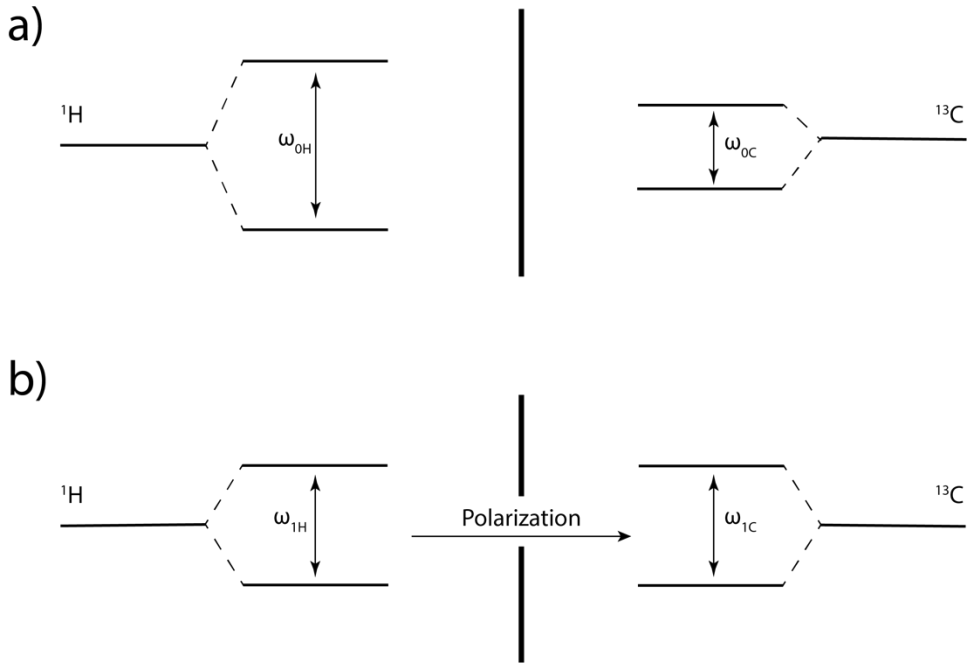

Figure 1-15. Diagram of spin flip energy transitions in an NMR system.

This phenomenon is referred to as the Hartman-Hahn matching condition (also referred to above in liquid correlational spectroscopy), and experimentally captured in cross polarization (CP) experiments. The basic pulse scheme for CP is shown in Figure 1-16.

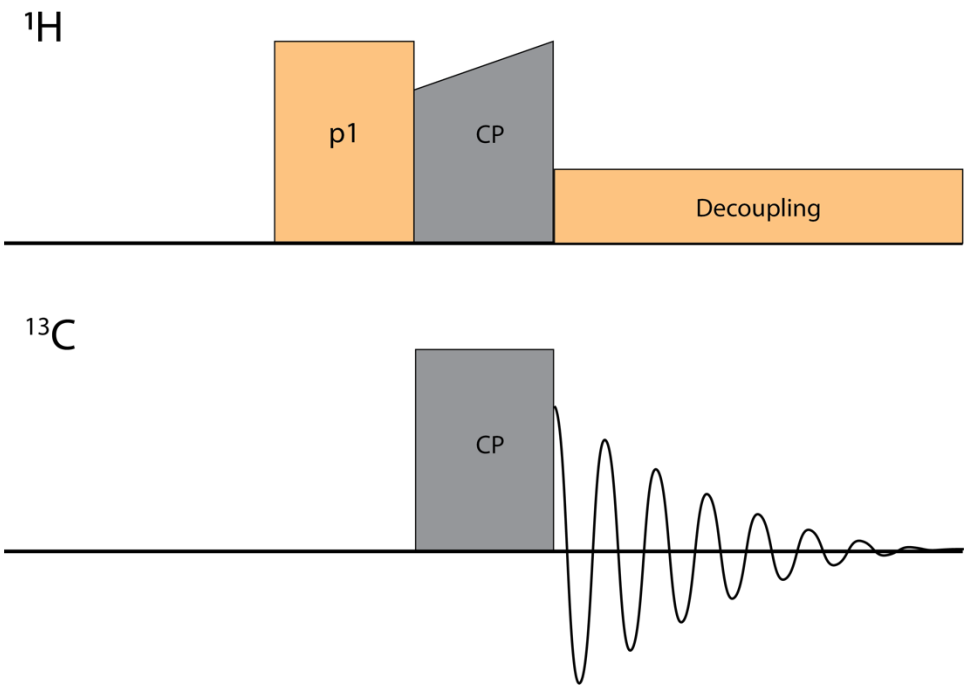

Figure 1-16. Cross polarization pulse sequence between hydrogen and carbon.

The first hard $\frac{\pi}{2}$ pulse is applied to the abundant proton nuclei to create the matching conditions to put it in contact with the less abundant carbon nuclei. Next, a combination of a hard pulse on the carbon and a ramped pulse on the protons facilitates the transfer of magnetization between these two populations as the carbon nuclei are rotated into the transverse plane. After the nuclei have been rotated, a decoupling pulse destroys any interactions between the two populations while the behavior of the carbon nuclei is observed.

The combination of CP and MAS creates the backbone of most modern ssNMR experiments. CP-MAS is a block which can be used in combination with dipolar recoupling, relaxation, and heteronuclear experiments to improve signal from dilute nuclei.

1.2.4.3 Dipolar Assisted Rotational Recoupling

Much like in above discussion of 2D correlational spectroscopy in solution NMR experiments, a similar need for a second dimension by which to resolve peaks exists in ssNMR. In fact, the broad

nature of solid state peaks renders these correlational experiments even more necessary for unambiguous interpretation of data. Within the body of this thesis, the presented work relies on the use of the homonuclear Dipolar Assisted Rotational Recoupling (DARR) experiment, whose pulse sequence is illustrated in Figure 1-17.[70,71]

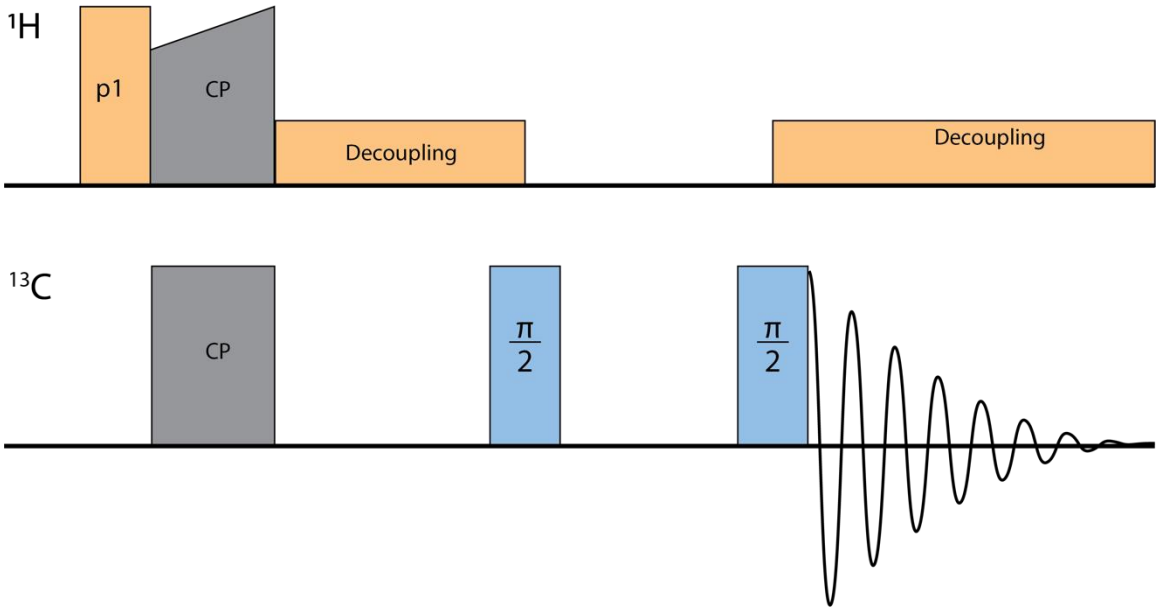

Figure 1-17. DARR pulse sequence schematic.

The pulse sequence begins with a cross polarization block to enhance the signal of the observed carbon nuclei, and then proceeds in a very similar manner to a TOCSY. The hard $\frac{\pi}{2}$ pulse during cross polarization rotates the nuclei into the transverse plane, and the second hard pulse in the carbon channel rotates the nuclei back up into the Z axis where it resides during a mixing time τ_{mix}. During this time, dipole-dipole interactions cause an interaction between proximal nuclei. The length of this mixing time is variable, and controls the distance of interactions observed. Long mixing times produce cross peaks between nuclei which are distantly coupled, while short mixing times only produce peaks from short range interactions. The third and final pulse on the carbon channel rotates the nuclei back into the transverse plane, and acquisition begins. The resulting spectrum is a 2D homonuclear correlational spectrum.

1.2.4.4 Change in Chemical Shift Analysis

In addition to being dependent on the orientation of the molecule within the sample relative to the magnetic field, the chemical shift of a nucleus in a sample depends greatly on its local environment. Reorientation of a peptide's secondary structure and binding interactions with a surface can both be considered changes in local environment, leading to measurable chemical shifts. Often times, a change in peptide structure will be observed as a change in chemical shift in backbone (C_o, C_α, C_β) residues while binding interactions will be observed as changes in the chemical shift of sidechain residues.[72–78] Binding interactions can drive structural reorientation, so changes in chemical shift can be observed throughout the peptide. Changes in the backbone chemical shifts are often hard to quantify without the use of software (discussed in section 1.3), however, interpretation of sidechain chemical shift changes is relatively straightforward. If the molecular orbital of a molecule is altered by a binding interaction with a charged center on a surface, the electronic shielding of the nucleus will change according to how much it now feels the applied magnetic field. In the case of a residue binding to a negatively charged functional center on a surface, the binding nuclei will have increased electron density, and therefore be more shielded from the magnetic field. This greater shielding would cause the resulting chemical shift to move upfield to a lower ppm value. Conversely, binding to a positively charged center would cause electronic deshielding, producing the opposite effect.

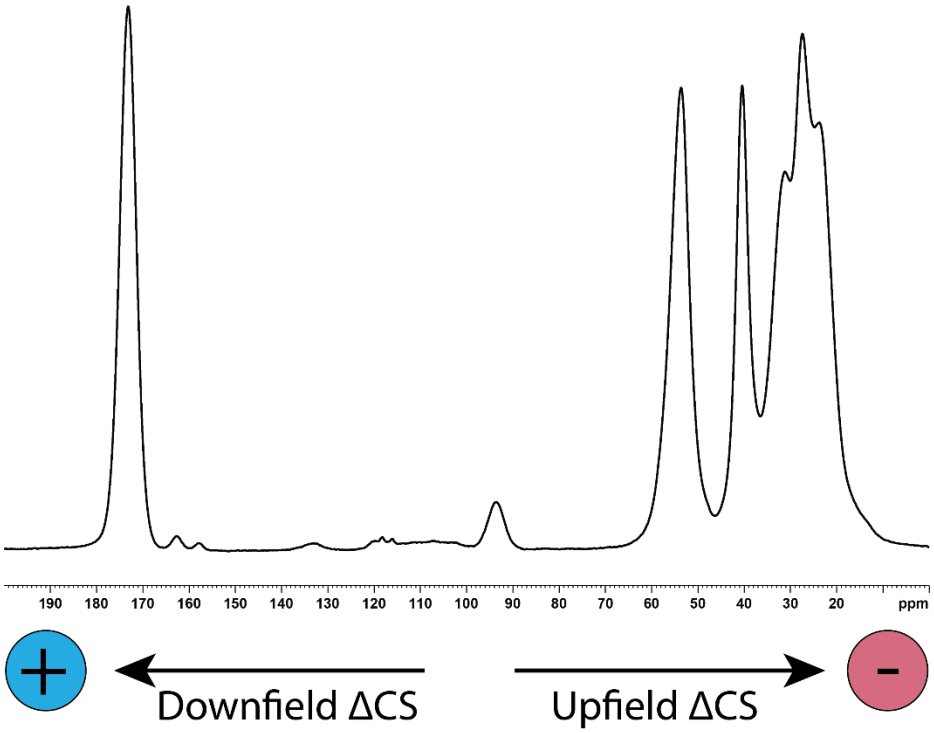

Figure 1-18. Legend of chemical shift changes as a function of binding interactions with a charged surface.

Comparing the chemical shift produced by a molecule in the absence of a surface (CS_{free}) to the chemical shift of the same molecule in the presence of it (CS_{bound}). By subtracting CS_{bound} from CS_{free}, the change (ΔCS) can be measured and interpreted. If the $\Delta CS = 0$, the nucleus is not affected by the presence of the surface, and therefore is not involved in a binding interaction. However, a nonzero ΔCS suggests that the local environment surrounding the nucleus has changed due to its proximity to the surface. The direction and magnitude of this change tells the nature and qualitative strength of the interaction, however a simple qualitative model of these interactions does not exist yet. Often additional binding studies, Density Functional Theory (DFT) simulations, and/or predictive shift fitting algorithms are required to interpret this data. One of these algorithms, TALOS-N, is discussed in Chapter 1.3.

1.3 TALOS-N

While no qualitative interpretation of changes in chemical shift exists, large datasets of interpreted NMR chemical shifts and improvements in data mining methods have allowed the generation of neural network engines which can pair patterns of chemical shifts with known structural features. TALOS-N is one of these such engines.[79] TALOS-N pulls the calculated chemical shift values of over 9500 protein residues along with their known torsion (ϕ and ψ) angles as well as 580 experimentally measured secondary chemical shifts and their corresponding torsion angles from proteins with known structure. Chemical shifts from a peptide with an unknown structure submitted to this algorithm will be subtracted from a second database of chemical shifts of unstructured 'random coil' residues, and those changes in chemical shift will be analyzed in conjunction with its nearest three neighbors on each side. A database search returns the 10 closest chemical shift matches, which are used to calculate both the predicted ϕ and ψ angles, as well as the predicted uncertainty. Uncertainty is tested via the 'leave one out' validation method. A subset of the database is removed before the fit is calculated. After TALOS-N generates a fitting algorithm which returns torsion angles within the acceptable limits, the algorithm is tested on the subset of structures which was held back. Both the accuracy and reproducibility of these measurements are then used to calculate the uncertainty of the prediction. This is repeated for every residue measured within a peptide, and a list of angles is returned as an output.

The list of angles can then be input into a visualization software such as Chimera, which returns a visualized structure given a written sequence and ϕ/ψ angles.[80] By constructing a visualization of the neat peptide structure and a second visualization of the peptide's structure when exposed to a

surface, backbone changes and energy minimized sidechain orientations can be observed, suggesting a possible binding mode.

1.4 SUMMARY

While no single experiment is adequate to give a full picture of the interaction between a peptide and a surface, a combination of experiments can provide a more complete story. Within this thesis the work presented relies upon multiple techniques to lend understanding to the recorded data.

Chapter 2 of this work investigates the mode of binding between the hexemeric surface binding peptide TBP. The presented work uses 2D solid state NMR methods to study the interactions between the arginine, lysine, and aspartic acid residues and the titanium dioxide surface in the absence of binding kinetics. Carbon change in chemical shift studies reveal a mode of binding, which is corroborated by previous literature and recent binding studies.

Chapter 3 approaches the question of how TBP binds through conducting DEST liquid state binding studies of alanine mutants of TBP in dynamic contact with the titania surface. While previous studies have looked at the effect on peptide binding strength as a function of replacing polar residues with alanine, and binding studies have been conducted looking at how the native peptide binds to titania, this work looks at how the mode of binding is affected by mutation studies. This work both helps validate the use of DEST for peptide-surface binding investigations, and lends mechanistic insight into the interplay between structure and binding mode in TBP.

Finally, chapter 4 focuses on elucidating how a fragment of the bone binding protein human Osteocalcin binds with both the mineral hydroxyapatite and titania through a combination of liquid and solid NMR studies. Two forms of this protein exist in nature. One form contains three post-

translationally modified glutamic acid residues within the first alpha helix, while the second form contains no such modifications. In this study, the decarboxylated form (dhOC-α_1) is investigated in this study. Binding isotherm studies prove that both fragments bind to both titania and hydroxyapatite. Circular dichroism and ssNMR studies show that the peptide remains unstructured in solution, and suggests that the peptide remains random coil even upon adsorption. Solid state NMR studies are then performed to measure structural change upon adsorption and to identify binding domains within the peptide.

Chapter 2. SURFACE BINDING OF TITANIA BINDING PEPTIDE

2.1 INTRODUCTION

Despite its near exclusive use in prosthetic design, relatively little is known about the detailed binding mechanisms of peptides to titania. Multiple studies of proteins have attempted to elucidate the nature of these interactions, however, the study of a small peptide could aid in this understanding.[8,9,20,21,30,81–85] First discovered by Shiba and Sano in 2003 through a phage display assay, the 12-mer Titania Binding Peptide (TBP) was shown to bind strongly and selectively to titania, silica, and silver.[22] Alanine mutation studies showed that the peptide could be reduced to the first six residues (RKLPDA) and retain the same binding affinity. Within these six residues, mutation of the arginine, proline, and aspartic acid produced a significant decrease in measured peptide binding to titania, while alanine replacement of the lysine residue caused the peptide to have a greater surface affinity. The authors postulated that arginine and aspartic acid created the binding domain between acidic and basic terminal hydroxyls respectively, and that the basic nature of lysine and its close proximity to the arginine created a competing reaction that could 'knock' the arginine loose. Proline is known to induce kinks within a peptide and is suspected of forcing a stereochemistry, which aligns the arginine and aspartic acid in such a way they could bind favorably.

Later studies attempt to corroborate this proposed binding mechanism, but the result of their findings creates a rather muddled picture of TBP-6 binding. Nuclear Overhouser Effect studies by Mirau and Naik and AFM studies by Hayashi, Shiba, and Sano both confirm the importance of the arginine and aspartic acid in binding, while dismissing the role of lysine in its interaction with the surface.[84,86] The findings of the AFM studies go further, suggesting that proline plays an

integral role in the binding mechanism. However, STD-NMR studies of TBP-6 binding to titania suggest that only the arginine and lysine residues come into contact with the oxide surface.[87] This finding is corroborated by molecular dynamics simulations, which postulate a water-mediated interaction between these basic residues and the negatively charged surface hydroxyl groups on the titania.[20]

Work by our group has focused on interpreting the underlying mechanisms which have produced these varying results using a broad range of NMR techniques. The work in this study contributes to this effort by embarking on a ssNMR ΔCS investigation of the interactions between the functional sidechain residues of the three polar residues (R, K, D) and the TiO_2 surface in order to understand how the peptide binds on a long timescale. In particular, research focused on understanding which residues interact with the surface, by what mechanism these sidechains interact, as well as how the structural conformation may change as a result of binding.

2.2 Experimental Methods

2.2.1 *Materials*

All Fluorenylmethyloxycarbonyl (Fmoc) protected amino acids were purchased from P3 Biosystems (Louisville, KY), and preloaded Fmoc-protected alanine Wang resins were purchased from EMD Millipore (Burlington, MA). Isotopically enriched Fmoc protected residues were purchased from Cambridge Isotope Laboratories (Tewksbury, MA). All other reagents, unless otherwise noted, were purchased from Sigma Aldrich (St. Louis, MO), and used without further purification. All solvents were HPLC grade.

2.2.2 *Peptide Synthesis*

Naturally abundant and isotopically enriched peptides (RKLPDA) were synthesized in the solid phase using a CEM Liberty Blue peptide synthesizer with a standard Fmoc and tert-butyl protection scheme as previously described.[88] Dimethylformamide (DMF) was used to swell the pre-loaded Wang resin (Fmoc-Ala, 0.67 mmole/g) before deprotection with piperidine (20% v/v in DMF) and microwave heat (50 C for 15 sec, 90 C for 50 sec). The resin was then washed with DMF. A solution of the desired amino acid in DMF (0.2 M) was then added to the reaction vessel and coupled with N,N'-Diisopropylcarboiimide (DIC) (0.492 M in DMF), Diisopropylethylamine (DIEA) solution (1 M oxyma and 97.6 mM DIEA in DMF) and microwave heat (75 C for 15 sec, 90 C for 110 sec). Excess amino acid was drained, and the resin washed with DMF. This coupling procedure was repeated for each residue. The resin/peptide mixture was then washed in dichloromethane (DCM) and allowed to dry overnight. Peptides were cleaved from the resin by adding 95:2.5:2.5 trifluoroacetic acid (TFA):triisopropylsilane:water to a 15 mL centrifuge tube and agitating for two hours. The peptide was precipitated from the liquid phase by adding it drop wise to approximately 40 mL of cold t-butyl methyl ether. The product was centrifuged into a pellet and washed with 25 mL of cold t-butyl methyl ether three times and dried overnight in a vacuum desiccator. The pellet of solid peptide was then dissolved in 15:0.2:84.8 acetonitrile:TFA:water at a concentration of 10 mg/mL, filtered with a 0.2 µm nylon syringe filter, and purified via HPLC, as described in the subsequent section. Product was confirmed via Electrospray Ionization Mass Spectrometry (ESI-MS).

2.2.3 *Peptide Purification*

All HPLC was carried out on a Vairan ProStar reverse phase high pressure liquid chromatograph. Solvents for purification were water (A) and acetonitrile (B) with 0.2% TFA (*v/v*) added to each

solvent. Presence of the analyte was measured by UV lamp at 220 nm. The chromatograph was equipped with an Altima WP C4 semi-prep column (250 x 22 mm, 5 μm particle size) running a gradient of 22-40% mobile phase B over 20 minutes at a flow rate of 8 mL/min. The peptide of interested eluted at ~10 minutes, was collected and lyophilized to isolate the pure peptide.

2.2.4 *ESI-MS*

ESI-MS (Bruker EsquireLC) was used to verify the product and its purity. Analytes were ionized using a positive ESI using the following conditions: 3 kV spray voltage, 350 °C drying gas at 10 L/min, 30 psi nebulizer, 4 kV capillary voltage. Data was collected in full scan mode (mass range 50-2200 m/z) with a scan resolution of 13000 m*sec/z. Ion optic voltages were: 1, 30 V skimmer; 2, 6 V skimmer; 3 V octapole; 100 Vpp octapole RF; 2 V octapole Δ; -5 V lens 1; -60 V lens 2. Bruker Daltonics DataAnlysis software, version 3.0, was used for data acquisition and analysis.

2.2.5 *Binding Isotherms*

Titanium dioxide (60 mg) was added to a 1.5 mL microcentrifuge tube and mixed with 250 μL TBP (0.75, 1.25, 2.5, 5, 7.5, 10, 12.5, 15, 17.5, 20, 22.5, 25 mM) in 100 mM phosphate buffer solution (pH 7). Samples were shaken overnight at room temperature to ensure equilibration of binding, then centrifuged to form a pellet (2.8k RPM, 30 minutes). The supernatant was decanted, and a 50 μL injection was used for HPLC analysis of each sample. Quantitation of TBP for isotherms was carried out on the same Varian ProStar RP-HPLC equipped with a Grace Econosphere C18 analytical column (250 mmx 4.6 mm, 5 μm particles). Solvents for purification were water (A) and acetonitrile (B) with 0.1% TFA (*v/v*). A gradient of 25-55% mobile phase B for 15 minutes was used. The resulting peak was integrated using The R Project software package and compared against a standard curve generated by TBP (0.125, 0.25, 0.5, 1.25, 2.5, 5 mM) in

100 mM phosphate buffer to yield the concentration of free TBP.[89] The amount of bound peptide was calculated via:

$$TBP_{bound} = TBP_{initial} - TBP_{free}$$

2.2.6 *NMR Sample Preparation*

TBP was dissolved in a 100 mM phosphate buffer solution (pH = 7) to form a 10 mM solution, and 1 mL was added to every 70 mg of TiO2 nanoparticles. The slurry was then vortex mixed overnight. A centrifuge was used to separate the solids from the supernatant, which was then decanted. Titania nanoparticles were then dried in vacuo overnight before packing into a 3.2mm Bruker MAS rotor.

2.2.7 *Solid-State NMR Experiments*

Spectra were recorded on a 11.4 T (^{1}H 500.13 MHz, ^{13}C 125.79 MHz) Oxford Instruments magnet outfitted with a Bruker AV III console and HXY TriGamma 3.2mm MAS probe. Samples were spun at 10 KHz ± 5 Hz for all experiments. ^{1}H to ^{13}C cross polarization-magic angle spinning (CP-MAS) spectra were recorded using a 3 μs ^{1}H 90° pulse, a recycle delay of 3-4 s, and 2-16k scans depending on the sample. A 1.0 ms contact time was used with a 30% descending linear ramp on ^{1}H power during CP. Two-dimensional (2D) Dipolar Assisted Rotational Resonance (DARR) experiments were collected with the same CP conditions, a 2.0 s recycle delay, and 30 ms mixing time.[70] Between 256 and 512 scans were collected with 1024 points in the direct dimension and 128 scans in the indirect. High powered Two-Pulse Phase Modulated (TPPM) ^{1}H decoupling was used during data acquisition with an RF field strength of 80 kHz.[90] All ^{13}C chemical shifts were referenced indirectly to TMS by setting the CH resonance of adamantane at 38.48 ppm.[91]

2.3 RESULTS

The binding of TBP-6 to TiO_2 was confirmed via binding isotherm studies, finding the binding constant to be 4.1 mM in accordance with previous literature. Binding constants were calculated using the Langmuir model (Equation 1.1).

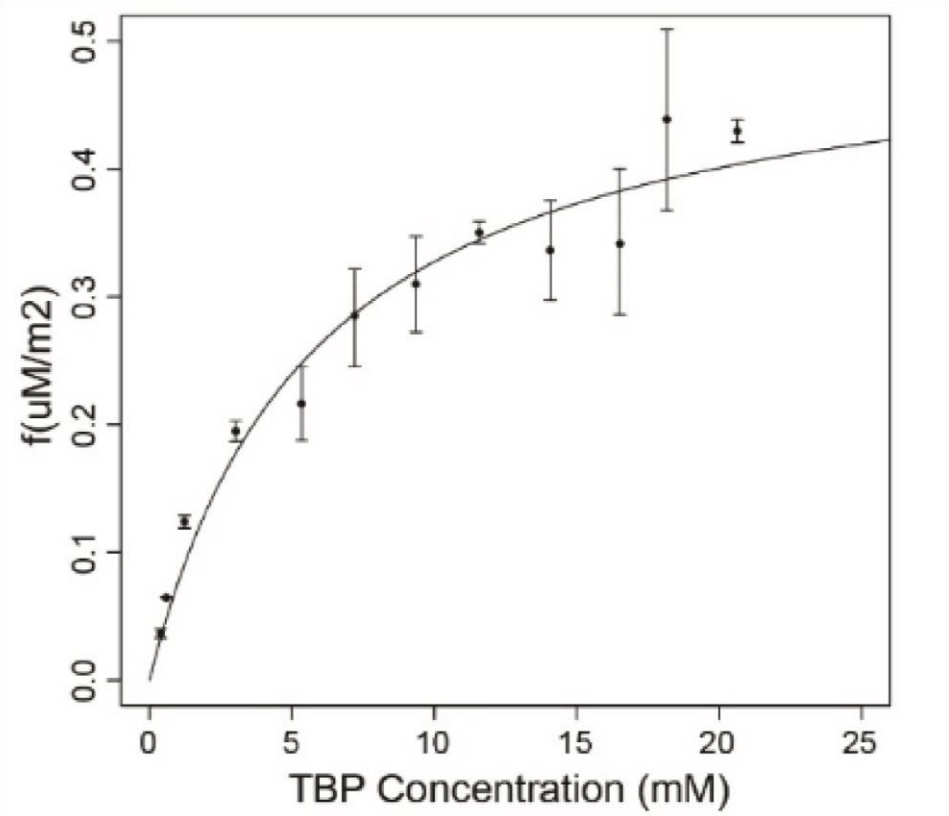

Figure 2-1. Binding isotherm of TBP-6 on TiO2. The mode of adsorption appears to be non-cooperative, and therefore can be modeled using the Langmuir binding isotherm model. Fitting of this equation results in a measured binding constant Kd=4.1 mM.

Three uniformly ^{13}C isotopically enriched TBP samples were synthesized to investigate the binding interactions between the polar residues and the surface as outlined in Table 2-1. Polar residues were selectively chosen for this investigation due to prior evidence of their interaction with surfaces. While hydrophobic residues have been implicated previous binding interactions, to

date neither leucine nor alanine has been implicated as an active participant in the binding to titania.[9,24,30]

Table 2-1. Labeling scheme for TBP-6. A proceeding asterisk signifies the uniform $^{13}C/^{15}N$ labeling of a particular residue

Sample Name	**Sequence**
TBP-R	***R**KLPDA
TBP-K	R***K**LPDA
TBP-D	RKLP***D**A

Correlational ^{13}C DARR spectra were recorded of each of these samples neat and adsorbed to titania. Neat spectra were used to unambiguously assign each peak to a residue, and the difference in recorded chemical shift values between the neat and absorbed samples were calculated using the equation:

$$\Delta CS\ (ppm) = CS_{bound}\ (ppm) - CS_{neat}\ (ppm)$$

2D spectra and their assignments can be found in Appendix A (Figure A-4 and Figure A-5). The differences in chemical shifts between peptides bound and free can be visualized by a plot of ΔCS as a function of residue position as shown in Figure 2-2. A table of ΔCS values can also be found in Appendix A (Table A-1 through Table A-4).

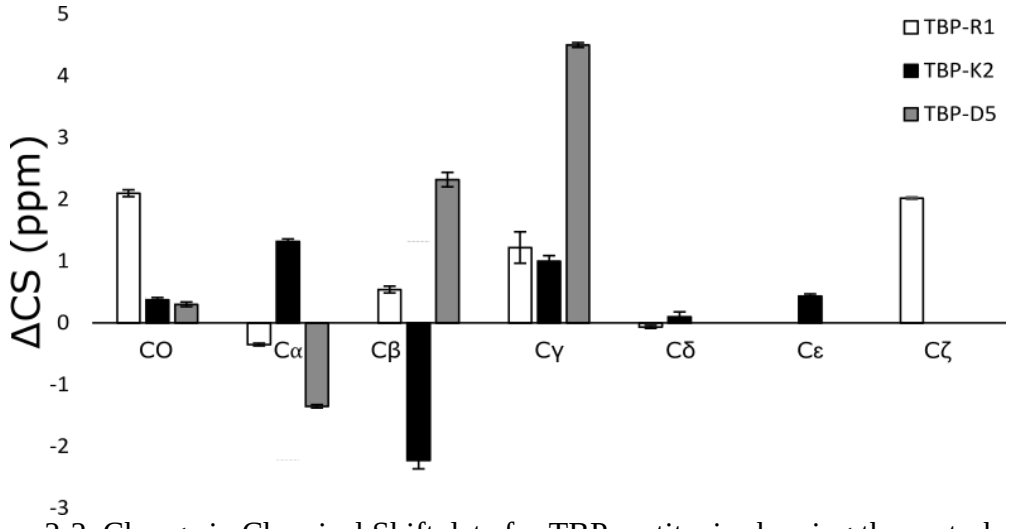

Figure 2-2. Change in Chemical Shift data for TBP on titania showing the perturbations of R1 (white), K2 (black), and D5(grey) for each position.

Analysis of this data can be broken into two sections: analysis of the backbone carbons (^{13}CO, ^{13}Cα, and ^{13}Cβ), and analysis of sidechain carbons (^{13}Cγ, ^{13}Cδ, ^{13}Cε, and ^{13}Cζ). Several significant (|ΔCS| >1) shifts can be observed along the backbone at the R1 ^{13}CO, K2 ^{13}Cα and ^{13}Cβ, and the D5 ^{13}Cα and ^{13}Cβ positions. This signifies possible structural rearrangement of the peptide backbone upon titania adsorption, but without further computational studies, this is the extent of what can be concluded about the backbone. Next looking at the sidechain residues, large downfield perturbations of the D5 ^{13}Cγ (+4.5 ppm) and the R1 ^{13}Cζ (+2.0 ppm) are observed. The small downfield perturbation in the K2 ^{13}Cε (0.4 ppm) is significantly smaller than previously reported ΔCS values from binding interactions, suggesting that its local environment is not experiencing a significant change, and therefore K2 not involved in surface binding.

2.4 DISCUSSION

Analysis of the change in ^{13}C chemical shift via solid state NMR has been used extensively to study binding interactions between peptides and inorganic surfaces. Unlike many other spectroscopic techniques, ssNMR is uniquely adapted to probe static solid phase surface

interactions due to its tolerance of solid mixed media as well as direct probe of NMR-active isotopes incorporated within the interface. A wide range of experiments can investigate system properties including sidechain dynamics, crystal structure, homonuclear and heteronuclear correlational interactions within the peptide and between the peptide and the surface, and measure the distance between heteronuclei using recoupling techniques.[18,92] However, due to the combination of relatively low natural abundance and high quadripolar moment of both ^{47}Ti and ^{49}Ti, ssNMR investigations of peptide systems on this oxide have primarily focused on teasing out secondary structure and pinpointing residues that are likely binding candidates through change in chemical shift (ΔCS) measurements.

To date, such an approach at studying binding has not been attempted with TBP. Previous NMR studies have investigated TBP binding by employing saturation transfer difference (STD) and nuclear Overhouser effect (NOE) studies. While valid measures of binding, these techniques are limited to only detecting transient modes of binding which exchange on a fast timescale, and are unable to detect slower, more strongly bound species which could be contributing to binding as well. Unpublished work by our group investigating this system using dark state exchange saturation transfer (DEST) experiments combined with structural constraints from NOESY experiments suggest that TBP is binding through its R1 and K2 residues. The D5 residue is packed closely to the titania surface, however its decreased relaxation time suggests that it is not a primary anchor for the peptide.

As a direct probe of the changes nuclei experience as their environment is altered, perturbations in chemical shift can suggest changes to both the secondary structure as well as binding interactions between the sidechains and the surface. Typically, changes in chemical shift within the backbone

carbons (^{13}Co, ^{13}Cα, ^{13}Cβ) are ascribed to changes in the secondary structure upon binding to the surface. Similarly, changes in chemical shift observed within the sidechain carbons (^{13}Cγ, ^{13}Cδ, ^{13}Cε, ^{13}Cζ) are commonly attributed to changes in their electronic shielding due to proximity to the oxide surface. A downfield chemical shift of the R1 ^{13}Co (2.1 ppm) and D5 ^{13}Cβ (2.3 ppm) as well as the upfield shift of the K2 ^{13}Cβ (-2.2 ppm) suggest a conformational rearrangement of the peptide backbone. Compared to the backbone chemical shifts observed in other systems, these perturbations are relatively small, suggesting a mild reorientation.[8,9,30] While normally these chemical shifts would be input into the structural prediction program TALOS-N and the backbone torsion angles calculated, TBP is too small and the density of carbon resonances is too low for structural determination. However, binding interactions can still be inferred from this dataset. Large changes in the chemical shifts between the neat and surface adsorbed peptide at the terminal carbon residues are observed in the R1 ^{13}Cζ (2.0 ppm) and D5 ^{13}Cγ (4.5 ppm) residues. Similar downfield perturbations of the ^{13}Cζ residues of arginine have been observed in the binding of R5 to titania, and are attributed to the arginine sidechain coming into close proximity with the nearby lysine.[9] This change in chemical shift could also be reflective of the arginine terminus finding itself in close proximity to either a basic terminal hydroxyl, or a sodium ion introduced by the buffer. Additionally, prior work by Buckle et al on SNa15 cite downfield shifts of the D2 and D3 ^{13}Cγ residues as well as the ^{13}Cδ residues of E4 and E5 on titania as evidence of proximity to the surface.[8] Similar work by Fernandez found that chemical shifts of the terminal carboxyl of poly-glutamic acid adsorbed to the titania surface produced a downfield chemical shift of 2 ppm.[24] These studies both explain the downfield chemical shift as evidence of the terminal side chain to a basic center, presumably the OH_2^+ terminal surface hydroxyl. A similar comparison of the recorded lysine ^{13}Cζ chemical shifts can be performed between the recorded shifts in both papers.

While a large ΔCS>1 is attributed by experimental findings and ssNMR measurements to be indicative of the residue coming into proximity to an electron dense environment, anything less than that is considered to be non-binding. Through this framework, it is apparent that K3 is not involved with binding to the surface. The large changes in chemical shift along the backbone ^{13}Ca and ^{13}Cb could suggest a deflection of the lysine residue that would make it not amenable for surface interactions. Additionally, this lack of a large ΔCS perturbation in the terminal ^{13}Cε would also suggest that the arginine and lysine termini are not interacting strongly with one another. From this interpretation, it seems most likely that the arginine sidechain is in close proximity to the positive charge center intermediate anchoring the aspartic acid residue to the titania surface, and that the lysine residue is deflected away from this interaction.

These findings point to strong interactions involving the R1 and D5 residues, which closely aligns with the findings of early alanine mutation studies which found that the arginine, proline, and aspartic acid residues have a strong positive association with binding.[22] Additionally, the ΔCS measurements suggest that the R1 ^{13}Cζ could be in close proximity to the binding domain of the D5 ^{13}Cγ, which corroborates unpublished DEST work by our group on TBP. However, these findings do not align with previous STD-NMR and NOESY work presented by Suzuki et all, which found that only the R1 and K2 residues are involved in binding, leaving the aspartic acid free as part of an untethered tail.[87] Because the work put forward by Suzuki selectively investigates the behavior of the peptide during fast exchanges, it is possible that the reported results are only capturing one of multiple modes of TBP binding. Analogously, the ssNMR experimental data presented here only investigates the binding of titania in a static state in which exchanges are not possible, and does not capture fast exchange interactions. Work by Sampath et al conclude that surface inhomogeneity due to crystal defects and surface morphology can produce different modes

of binding, which each bind with different dissociation constants.[21] Indeed, this work confirms these findings, and brings another viewpoint to round out our understanding of this system across both timeframes, as well as an imperfect surface. TBP is able to bind through multiple motifs that are most advantageous given the features of the titania surface within each region of the oxide nanoparticle.

2.5 CONCLUSIONS

Building from previous work investigating TBP interactions with titania, this study is the first solid state NMR investigation of the subject. Focusing on the three residues most likely involved in surface interaction, ΔCS measurements track how the local environments of these residues change upon peptide binding to the rutile oxide. Unlike previous studies which have investigated TBP interactions on a medium or fast binding timescale, this work solely focuses on very slow timescale interactions. Due to the impractical nature of directly measuring peptide coupling to the NMR active nuclei in the oxide, this work chooses to approach its investigation through qualitative measurements.

In both the cases of R1 and D5, large downfield chemical shifts of the terminal $^{13}C\zeta$ and $^{13}C\gamma$ functional carbons respectively signal the proximity of their polar functional groups to the polar titania surface. In the context of previous literature, these interactions are interpreted to be indicative of surface binding interactions. The lack of such a change in chemical shift in the terminal carbon of K2 $^{13}C\varepsilon$ reveals it to be not involved in binding in this time domain, suggesting a mode of binding very similar to what was first proposed by Shiba and Sano through alanine mutation studies. Future DFT studies may explain the orientation and proximity of this residue to the TiO2 surface, and lend clarity to its behavior in static experiments In context with other

previous literature, this study rounds out our understanding of how TBP binds across a range of timescales: it exchanges quickly with the titania surface via binding interactions mediated by its basic R1 and K2 residues, and slowly with the surface through its R1 and D5 residues. The predominance of each binding mode is encouraged by the degree of hydroxylation found within segments of the titania surface.

Chapter 3. MUTATION STUDIES OF TITANIA BINDING PEPTIDE

3.1 INTRODUCTION

In addition to investigating the static interaction between labeled peptides and oxide surfaces using ssNMR, binding interactions can be probed as a function of mutation studies. Alanine substitution studies have been used in a number of peptides to investigate the role of individual amino acids on peptide binding affinity.[93–100] The structure of alanine is very simple, containing only the peptide backbone and a methyl sidechain, and by substituting an alanine residue in place of one with a functional group (i.e. lysine, aspartic acid, or leucine), the functional group is effectively removed, and the binding contribution of that group can be selectively explored by omission. If substitution of a particular residue with alanine causes a decrease in peptide adsorption, the functional group is assumed to be contributing to the binding interaction. Analogously, residue substitution that causes an increase in peptide binding shows which residues on a peptide inhibit binding, and any residue which does not affect the binding affinity upon alanine substitution is considered to not participate in binding. This process can be repeated iteratively throughout the peptide to indirectly analyze which residues contribute as binding motifs.

In their foundational work, Shiba and Sano performed alanine mutation studies on the original 12-mer peptide (RKLPDAPGMHTW).[22] Substitution of the R1, P4, and D5 residues with alanine showed a large decrease in peptide binding, while substitution of the K2 residue resulted in an increase in binding. The authors postulated that the guanidino moiety of arginine was electrostatically interacting with the deprotonated surface hydroxyls on the titania surface. Because both the arginine and lysine residues are basic, logic would suggest that both residues would contribute positively to binding through electrostatic interactions with the ubiquitous

deprotonated hydroxyl groups on the titania surface. However, Shiba and Sano postulate that since both residues have long functional sidechains, and are sequential, arginine and lysine may compete for available binding sites. Because of its structure, the guanidino group has the higher binding affinity in comparison to the amine, which results in an increase in binding upon alanine substitution of the lysine.[19,23] While alanine substitution of the arginine ablates the competitive interaction with the lysine, the lower binding affinity of its functional group in comparison to arginine is reflected in the measured reduction in peptide binding. Proline's contribution to binding is assumed to be structural rather than electrostatic. Known as the helix breaker, proline is known to induce backbone kinks as a direct result of its pyrrolidine side chain, which in the case of TBP is assumed to force both the basic and aspartic acid residues of the peptide into contact with the titania surface, thereby facilitating electrostatic interactions.[22,101,102] In the absence of proline, the peptide may not adopt this same structure, making those binding interactions less favorable, which would result in the decrease in peptide binding as observed by the mutation studies.

In order to confirm the analysis presented above of how mutations alter the binding profile of TBP, four mutants of TBP were synthesized with alanine point mutations at each of the four previously discussed residues (R1, K2, P4, and D5). The binding of these peptides to titania powder is subsequently directly studied using DEST, STD, and NOESY solution state NMR experiments. The results of these experiments reveal very distinct variations in binding as a direct result of these mutations, and point to the importance of arginine and lysine within the binding domain of TBP within a dynamic environment. In conjunction with Chapter 2, this data is analyzed to comment on the overall binding profile of TBP and the cause of these incongruous results.

3.2 EXPERIMENTAL METHODS

Peptide materials, and the method of synthesis, purification, and characterization of TBP and its mutants can be found in section 2.2.

3.2.1 *NMR Samples*

30 mM peptide stock solution was prepared in 20 mM phosphate buffer pH7 with 99.9% D_2O.

Samples without TiO_2 nanopowder in the presence of agarose gel were prepared by mixing 1% *w/w* agarose in 900 µL of 20 mM phosphate buffer (pH 7, 99.9% H_2O). The mixture was placed in a boiling water bath for 5 min, then removed to a block heater to cool. When the temperature of the sample is equilibrated to between 50 and 60 °C, 10 µL of peptide stock solution was added, resulting in a final TBP concentration of 3 mM. The warm solution was transferred to an NMR tube and allowed to cool at room temperature before acquisition.

Samples that contained TiO_2 nanopowder in the presence of gel were prepared by mixing 1% *w/w* TiO_2 nanopowder and 1% *w/*w agarose in 900 µL of 20 mM phosphate buffer (pH 7, 99.9% H_2O). The mixture was placed in a boiling water bath for 5min before being allowed to cool to 50-60 °C on a block heater. 10 µL of the deuterated peptide solution was then added to the physical mixture, resulting in a final peptide concentration of 3 mM. The warm solution was then transferred to an NMR tube and allowed to cool to room temperature before measurement.

3.2.2 *Liquids NMR Instrumentation*

All solution NMR experiments were recorded at 25C on a Bruker Avance III 500 MHz spectrometer fitted with a 5 mm BBI probe operating at a ^1H frequency of 499.89 MHz. Resonance assignments for all spectra were accomplished using total correlational spectroscopy (TOCSY)

which employs a DIPSI decoupling sequence and WATERGATE solvent suppression. TOCSY were recorded with a 15 ppm spectral width in both directions, 2048 and 512 complex points in the direct and indirect dimension respectively, and 32 transients following 32 dummy scans. A DIPSI decoupling pulse of 2.524 W was applied for a mixing time of either 30 ms or 70 ms. In all experiments, each transient utilized a 90 pulse of 15 W, and employed a 2.5-3 s recycle delay. Water suppression employed a 1 ms square pulse

3.2.3 *DEST Experiments*

^{1}H-DEST experiments were measured at multiple saturation fields (50 Hz, 150 Hz, and 300 Hz) using a ^{1}H DEST pulse scheme.[103] 1D ^{1}H spectrums were recorded in steps of 0.25 or 2.5 ppm with the position of the ^{1}H B1 field ranging from -100 ppm to +100 ppm, and an offset of -100 ppm was used for normalization. The saturation field was applied for 1 s, and a repetition delay of 3 s. NMR spectra were processed using Topspin 4.0 and spectra were analyzed using Bruker dynamics center.

3.2.4 *STD-NMR Experiments*

Two sets of spectra were recorded of each peptide in the presence of titania with a 60 ms gaussian saturation pulse applied at the offset frequency of water (S spectrum) and at 60 ppm (S_0 spectrum). Spectra were processed within Topspin, and the difference automatically calculated.

3.2.5 *NOESY Experiments*

NOESY spectra were recorded using the same experimental parameters as were employed for the DIPSI experiments.

3.2.6 *Data Analysis*

Data was processed in OriginPro (OriginLab Corporation, Northampton, MA, USA) using the Peak Analyzer toolkit. The DEST profiles were normalized to the intensity of the recorded peak with RF irradiation at -100 ppm (I_0).

3.3 RESULTS

3.3.1 *DEST*

Temporary immobilization of nuclei due to binding interactions often results in broadened linewidths and increased transverse relaxation rates (R_2), both of which are properties easily measured via standard NMR experiments. These changes can be visually observed within a 1D spectrum and quantified through the comparison of DEST measurements of a peptide neat, within a suspending matrix, and exposed to a surface.

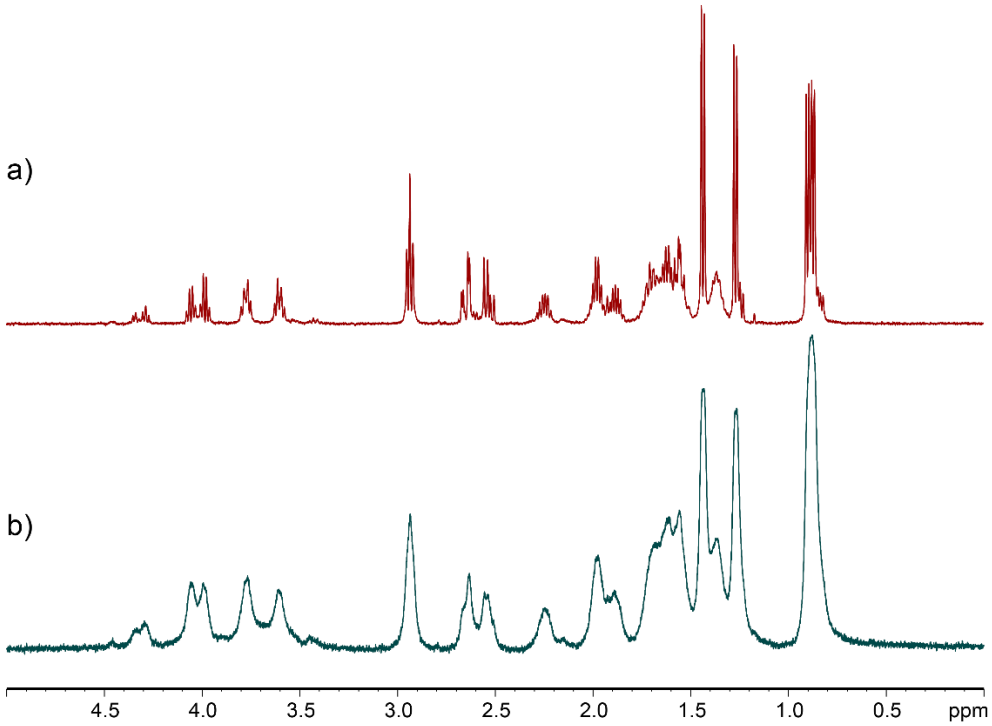

Figure 3-1. Stacked spectrum of TBP-R1A a) neat and b) suspended within agarose gel and exposed to titania.

In DEST experiments, the result of peak broadening results in the broadening of the DEST profile upon the addition of a mineral surface and stabilized by an agarose gel to the peptide sample. The degree and shape of this broadened profile can provide many insights into the strength and nature of this binding interaction. Because of the insoluble nature of titnia nanoparticles, agarose gel is used to suspend the insoluble matrix while leaving pores large enough to permit the diffusion of the peptide within the liquid matrix throughout the space. However, agarose is not a fully neutral molecule, and therefore DEST measurements should be recorded of the peptide in its presence, and broadening assessed benchmarked against the profile of the peptide within the agarose matrix. Upon the substitution of alanine for the arginine in TBP (TBP-R1A), mild broadening is observed in the ^{1}Hζ of K2, and slightly stronger broadening is observed in the ^{1}Hδ of L3 and the alanine residues, as well as the ^{1}Hδ of L3. Neither the P4 ^{1}Hβ nor the D5 ^{1}Hβ show peak broadening relative to the agarose gel upon the addition of titania to the sample. However, there is an obvious

broadening observed between the ^{1}Hβ of proline and the agarose gel, which is not observed in other residues. This suggests that the proline is interacting strongly with the polymer matrix.

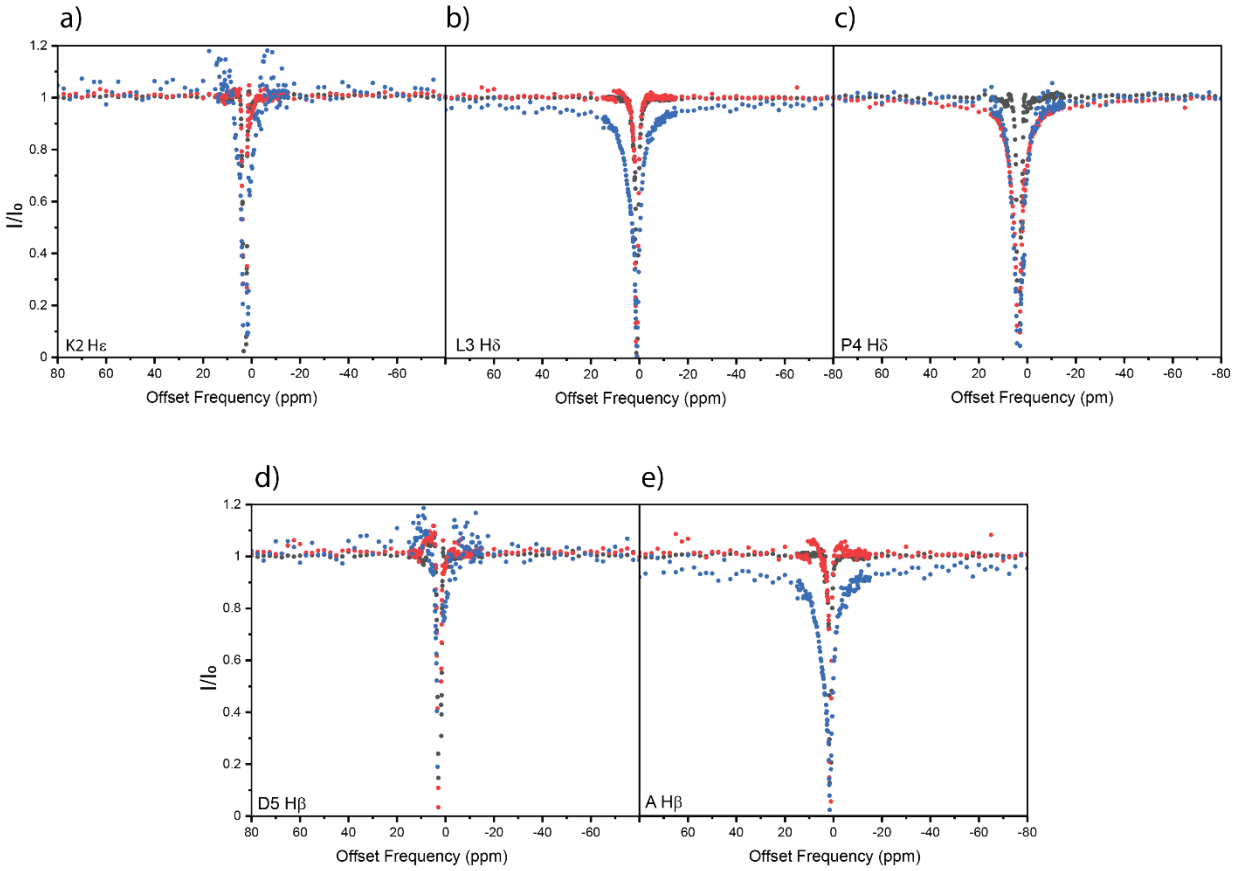

Figure 3-2. DEST profiles of individual residues within TBP-R1A neat (grey), in agarose (red), and exposed to titania (blue). Selected profiles are shown for a) alanine ^{1}Hε, b) leucine ^{1}Hδ, c) proline ^{1}Hδ, d) aspartic acid ^{1}Hβ, and e) alanine ^{1}Hβ.

Substitution of the K2 residue for an alanine in TBP (TBP-K2A) produced a similar series of DEST profiles. Much like in TBP-R1A, the ^{1}Hβ of D5 and the alanine residues as well as the ^{1}Hδ of L3 show moderate binding while the ^{1}Hβ of P4 shows no peak broadening. However, the ^{1}Hδ of R1 displays a large degree of broadening, suggesting a stronger interaction than what is experienced by the A2, L3, D5, and A6 residues, and a much stronger interaction compared to the K2 in TBP-

R1A. Interestingly, these peas seem to be broadened unilaterally, rather than uniformly as is seen in the Figure 3-2b.

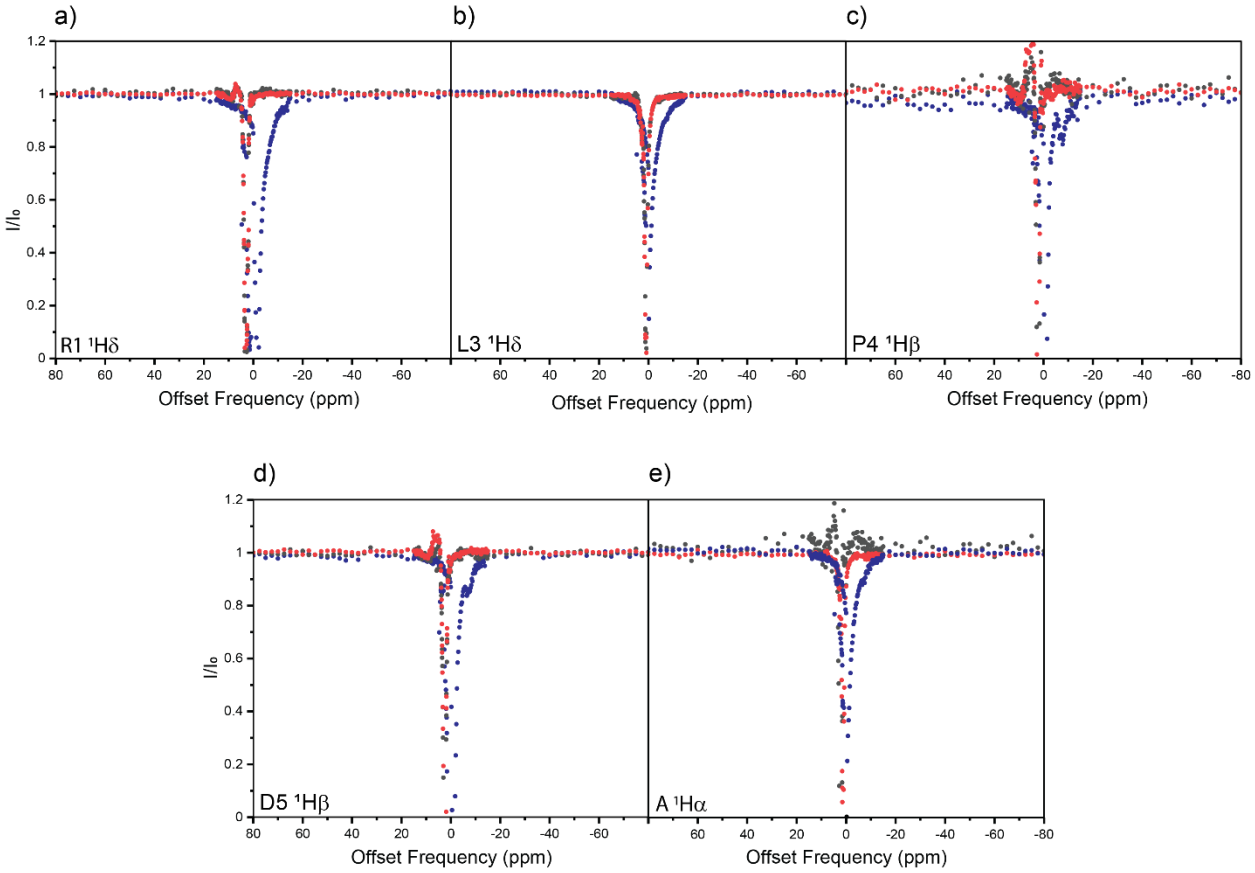

Figure 3-3. DEST profiles of TBP-K2A neat (grey), in agarose (red), and exposed to titania within an agarose matrix.

A very different series of DEST profiles are observed when applied to TBP-P4A. Each of the five unique residues exhibit a large degree of broadening upon the addition of TiO_2, suggesting a very strong, potentially immobile binding interaction between the peptide and the mineral surface.

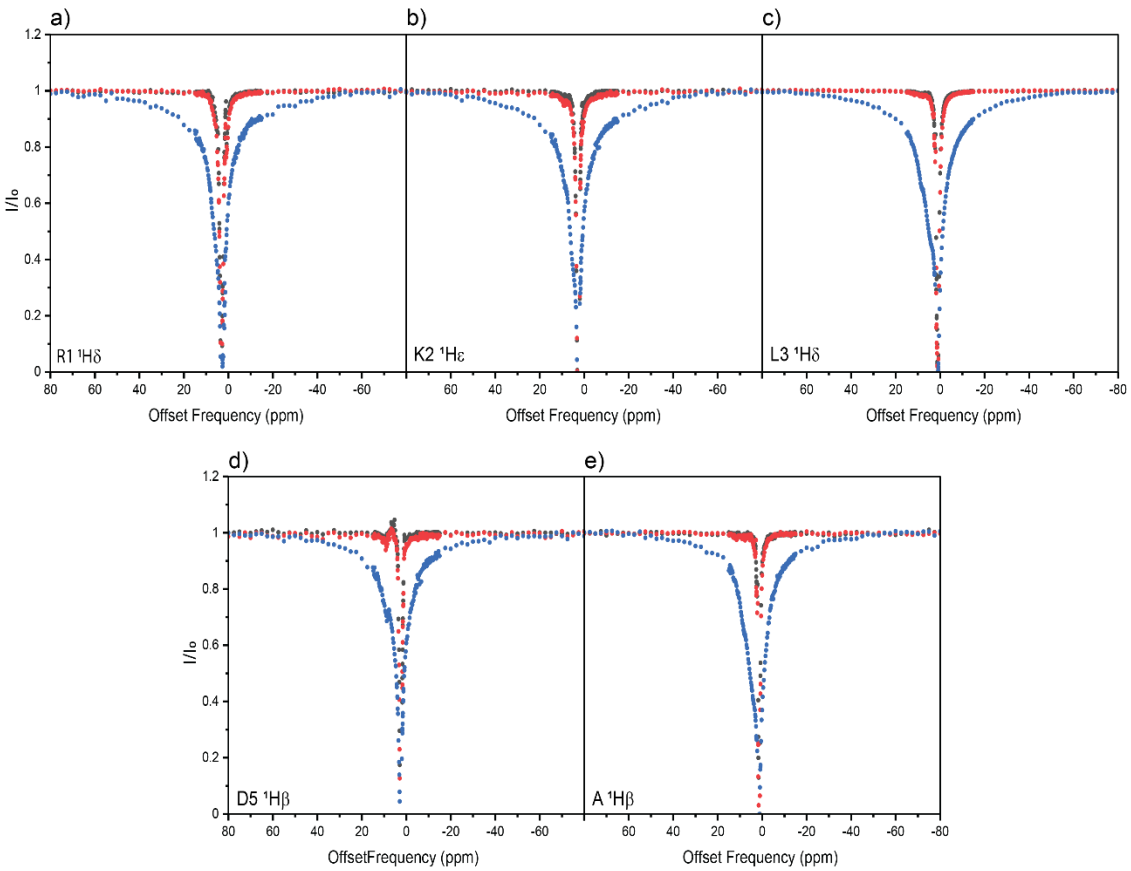

Figure 3-4. DEST profiles of TBP-P4A neat (grey), in agarose (red) and exposed to titania in an agarose matrix (blue). Representative profiles show DEST profiles recorded for a) R1 ^{1}Hδ, b) K2 ^{1}Hε, c) L3 ^{1}Hδ, d) D5 ^{1}Hβ, and e) A ^{1}Hβ.

Similar to what is observed in TBP-P4A, the substitution of alanine for the D5 residue in the same peptide (TBP-D5A) results in a profound broadening upon TiO_2 addition, suggesting a strong interaction of all residues within the peptide with the surface.

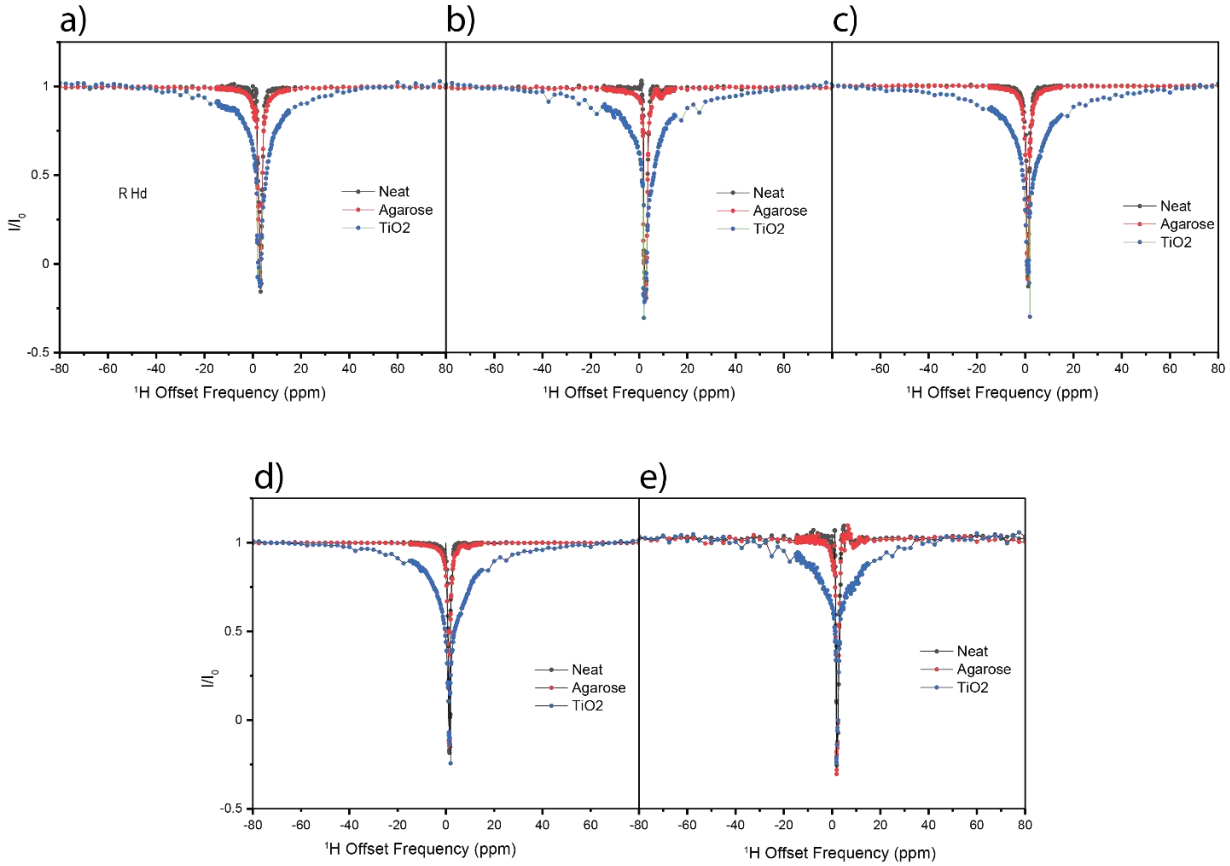

Figure 3-5. ^{1}H DEST Profiles of TBP-P5A at 300Hz neat (black), suspended in agarose gel (red), and in the presence of titania nanoparticles in agarose gel (black) for a) Hδ of arginine, b) Hε of lysine, c) Hδ of leucine, d) Hβ of proline, and e) Hβ of the alanine residues.

3.3.2 *STD-NMR*

Saturation transfer difference experiments were performed on each mutant of TBP neat in solution, within the agarose matrix, and in the presence of TiO_2 nanoparticles as shown in Figure 3-6.

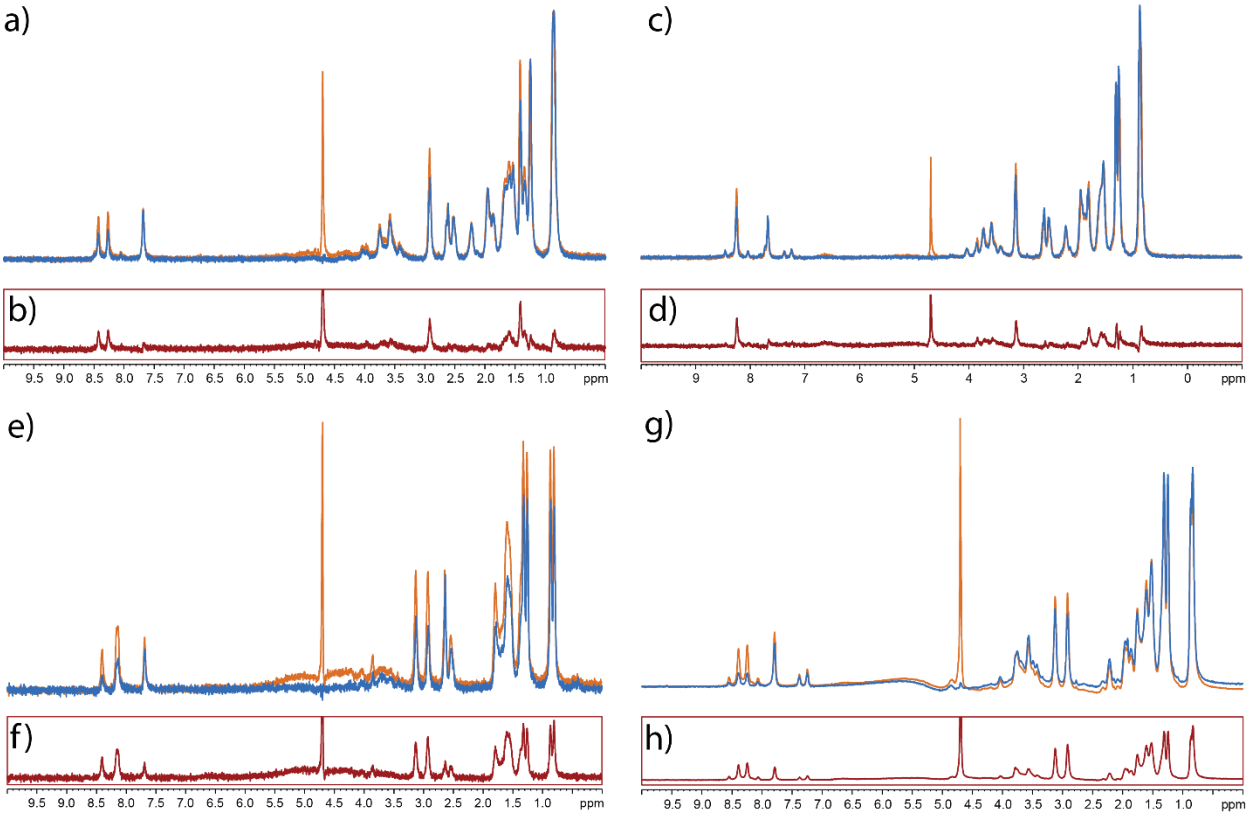

Figure 3-6. STD NMR of TBP Mutants exposed to TiO_2 within an agarose matrix. Overlays show the recorded S and S_0 spectra for TBP-R1A (a), TBP-K2A (c), TBP-P4A (e), and TBP-D5A (g). Difference spectra are shown below each set of overlays for TBP-R1A (b), TBP-K2A (d), TBP-P4A (f), and TBP-D5A (h).

Differences observed between the S_0 reference spectra and the S spectra in which a RF pulse transfers magnetization between surface immobilized water and the peptide suggest the interaction of these nuclei with surface water, and by extension, a binding interaction with the surface. The difference spectrum of TBP-R1A (Figure 3-6b) shows extensive difference peaks corresponding to K2 (^{1}Hε, ^{1}Hζ), L3 (1Hβ, ^{1}Hγ, ^{1}Hδ), P4 (^{1}Hβ, ^{1}Hγ, ^{1}Hδ), D5 (^{1}HN, ^{1}Hβ), and A (^{1}Hα, ^{1}Hβ). In the difference spectrum of TBP-K2A (Figure 3-6d), only peaks corresponding to the R1 (^{1}HN, ^{1}Hβ, ^{1}Hδ) and P4 (^{1}Hδ) residues are present. In the case of TBP-P4A (Figure 3-6f), differences are recorded in R1 (^{1}Hβ and ^{1}Hδ), K2 (^{1}Hε), L3 (^{1}Hβ, ^{1}Hγ, ^{1}Hδ), D5 (^{1}Hβ), and A (^{1}HN, ^{1}Hα, ^{1}Hβ). Lastly, the same analysis of the residual peaks of TBP-D5A (Figure 3-6 h) results in a large number

of peaks corresponding to R1 (^{1}HN, ^{1}Hβ, ^{1}Hγ, ^{1}Hδ), K2 (^{1}HN, ^{1}Hδ, ^{1}Hε), L3 (^{1}Hδ), P4 (^{1}Hβ, ^{1}Hγ, ^{1}Hδ), and A (^{1}HN, ^{1}Hα, ^{1}Hβ). Tables of difference peaks and their corresponding residues can be found in Appendix B (Table B-5 to B-8).

A similar analysis was performed on the recorded STD-NMR spectra of the TBP mutants in agarose gel, and the integrated area of the difference peaks were subtracted from the integrated area of the difference peaks observed in the titania-containing samples. The combined results of this analysis ae captured in the ΔA_{STD} value, as shown in Table 3-1. Tables of the calculated A_{STD} values can be found in Tables B-5 through B-8.

Table 3-1. ΔA_{STD} measurements for TBP A mutants. ΔA_{STD} values are calculated by subtracting the A_{STD} for agarose from the A_{STD} recorded in the presence of titania. NB signifies a clear non-binding interaction.

Peptide	**R1**	**K2**	**L3**	**P4**	**D5**	**A**
TBP-R1A	--	24%	4%	NB	NB	5%
TBP-K2A	2%	--	7%	NB	NB	7%
TBP-P4A	44%	46%	33%	--	22%	29%
TBP-D5A	34%	40%	33%	13%	--	34%

Table summarizes the measured amplitude of the STD difference spectrum normalized against the corresponding amplitude of the S_0 peak (A_{STD}) for TBP-R1A in solution, within the gel, and exposed to titania within the gel. By comparing the peak amplitude recorded by the STD spectrum of TBP in agarose to the amplitude of the same peptide in agarose with suspended titania nanoparticles, the entanglement interactions between the peptide and the agarose polymer matrix

are subtracted, leaving only the difference in intensity which can be directly attributed to the addition of titania. This practice is very analogous to comparing the DEST profiles of TBP mutants in agarose gel to the same peptides mixed with titania within the same gel matrix. Signal attenuation, or a large ΔA_{STD} would suggest a perturbation in the sidechain dynamics caused by close proximity of the nucleus to the immobilized water layer present on the titania surface. This binding interaction is between a particular residue and a surface not attributed to the interaction between the peptide and the gel matrix. Such strong interactions are observed in the K2 of TBP-R1A, as well as in every residue recorded within TBP-P4A and TBP-D5A.

3.3.3 *NOSEY*

In addition to DEST and STD-NMR experiments, NOSEY spectra were recorded for each mutant in a 20 mM phosphate buffer 90:10 H_2O:D_2O mixture. Crosspeaks in the spectra represent through-space NOE interactions between residues. Two sets of spectra were recorded of the sample: the first neat in buffer, and a second exposed to titania nanoparticles within the agarose matrix. The neat spectra are shown below in Figure 3-7.

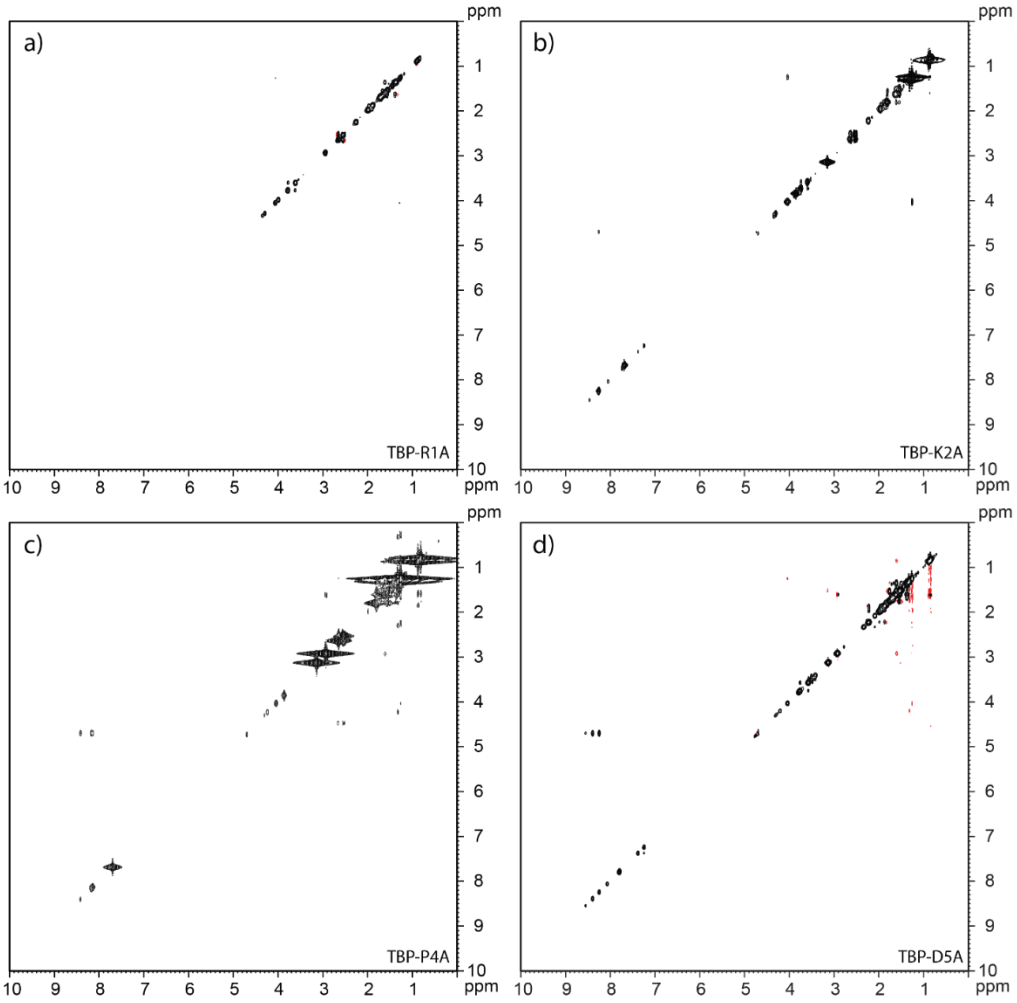

Figure 3-7. NOESY profiles of a) TBP-R1A, b) TBP-K2A, c) TBP-P4A, and d) TBP-D5A recorded in 20 mM phosphate buffer.

Off-diagonal crosspeaks typically represent the presence of through-space spin-lattice cross-relaxation interactions between proximal nuclei, typically as a result of peptide folding. The lack of such peaks as observed in TBP-R1A (a), TBP-K2A (b), and TBP-D5A (d) point to a more random coil construct. While no mutant of TBP showed much secondary structure, the presence of more crosspeaks in the spectrum of TBP-P4A suggests a larger degree of folding in comparison to the other mutants. Of particular interest are the observed interactions between the R1 ^{1}Hγ (1.603 ppm) and the D5 ^{1}Hβ (2.896 ppm) protons, as well as the L3 ^{1}Hδ (0.859 ppm) and the R1 ^{1}Hβ

(1.815 ppm) protons. The proximity of the R1 sidechain protons to protons in the L3 and D5 sidechains suggests a larger degree of packing upon the substitution of the rigid proline for a more flexible alanine in the TBP-P4A mutant. Any crosspeaks observed along 4.7 ppm are attributed to the interaction of the proton with water from the aqueous solution. All observed signals from the crosspeaks share the same positive sign as the backbone, suggesting that their interactions serve to slow down and immobilize the proton dynamics as would be expected in the the case of either the formation of a rigid core structure or upon binding to a larger, slow tumbling surface.

The second recorded series of NOESY spectra of the peptide exposed to titania within agarose are shown in Figure 3-8.

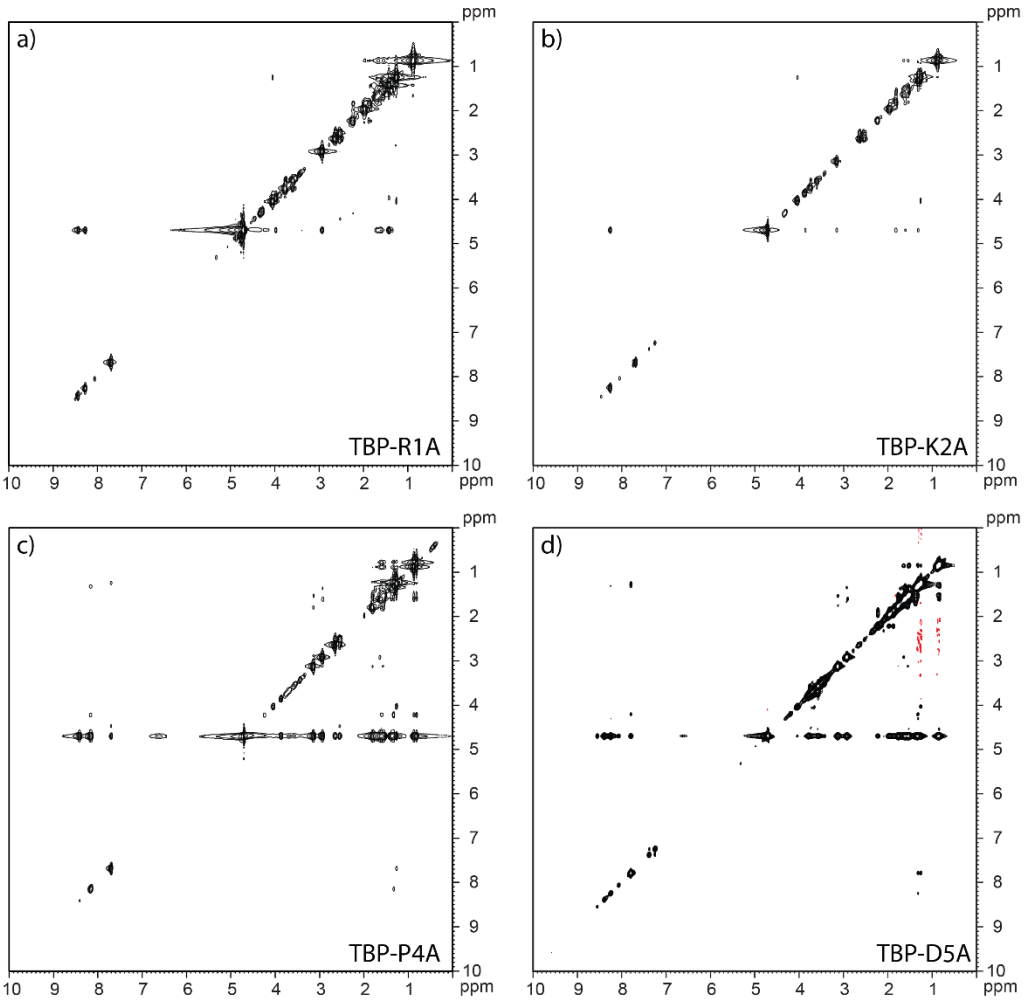

Figure 3-8. NOESY spectra of 3 mM a) TBP-R1A, b) TBP-K2A, c) TBP-P4A, d) TBP-D5A exposed to TiO_2 nanoparticles suspended by an agarose matrix.

The spectrum of TBP-R1A (Figure 3-8 a) contains a significant number of crosspeaks. Positive signals are observed between: A ^{1}Hβ (1.25 ppm) and A ^{1}Hα (4.067 ppm), K2 ^{1}Hγ (1.35 ppm) and K2 ^{1}Hε (2.939 ppm), K2 ^{1}Hδ (1.61 ppm) and K2 ^{1}Hε (2.939 ppm), P4 ^{1}Hγ (1.86 ppm) and P4 ^{1}Hβ (2.239 ppm), P4 ^{1}Hγ (1.99 ppm) and P4 ^{1}Hβ (2.247 ppm), K2 ^{1}Hβ (1.683 ppm) and L3 ^{1}Hδ (0.85 ppm), L3 ^{1}Hδ (0.85 ppm) and L3 ^{1}Hβ (1.581 ppm), K2 ^{1}Hβ (1.683 ppm) and K2 ^{1}Hγ (1.35ppm). However, upon analysis of the NOESY recorded of TBP-R1A in agarose gel (Figure B-6.a), it is apparent that most of these cross peaks occur in that spectrum as well, signaling that these interactions are not due to spin-lattice interactions with the nanoparticle surface, but rather partial

immobilization through interactions with the agarose gel matrix. Additionally, the minimal presence of inter-residue contacts suggests that TBP-R1A remains relatively unstructured even during a binding interaction.

Analysis of the crosspeaks that arise from the NOESY of TBP-K2A is much more straightforward given the lack of crosspeaks observed both in the NOESY of TBP-K2A in agarose as well as in agarose with titania. Positive crosspeaks are observed between: P4 ^{1}Hβ (2.222 ppm) and P4 ^{1}Hγ (1.91 ppm), L3 ^{1}Hγ (1.53 ppm) and L3 ^{1}Hδ (0.85 ppm), P4 ^{1}Hγ (1.88 ppm) and P4 ^{1}Hβ (2.22 ppm), L3 ^{1}Hγ (1.615 ppm) and L3 ^{1}Hβ (1.79 ppm). There are no inter-residue contacts to suggest peptide folding, and very few contacts to suggest a binding interaction on the timescale observable to the NOESY experiment.

The NOESY spectrum of TBP-P4A reveals a large network of crosspeaks in addition to those observed in the NOESY neat peptide: A ^{1}Hβ (1.27 ppm) and K2 ^{1}Hζ (7.66 ppm), L3 ^{1}Hα (4.23 ppm) and L3 ^{1}Hβ (1.598 ppm), L3 ^{1}Hα (4.23 pm) and L3 ^{1}Hδ (0.846 ppm), D5 ^{1}Hα (4.46 ppm) and D5 ^{1}Hβ (2.539 ppm), D5 ^{1}Hα (4.46ppm) and A ^{1}HN (7.699 ppm), A ^{1}Hα (1.262 ppm) and A ^{1}Hβ (4.00 ppm), R1 ^{1}Hβ (1.81 ppm) and R1 ^{1}Hδ (3.11 ppm), R1 ^{1}Hδ (3.11 ppm) and R1 ^{1}Hγ (1.569 ppm). The extent of these strong crosspeaks and the number of inter residue communication suggests a strong binding interaction between the peptide and the surface as well as a tight folding of the peptide itself. Unlike in the case of TBP-R1A, the NOESY of TBP-P4A in agarose reveals very few crosspeaks not associated with the solvent, suggesting that all recorded crosspeaks are the result of TBP-P4A either adopting secondary structure or binding with the titania surface.

Finally, TBP-D5A produces multiple crosspeaks: A ^{1}HN (7.803 ppm) and A ^{1}Hα (4.19 ppm), A ^{1}HN (7.803 ppm) and A ^{1}H β (1.25 ppm), R1 ^{1}Hδ (3.121 ppm) and R1 ^{1}Hγ (1.51 ppm), R1 ^{1}Hδ

(3.121 ppm) and R1 ^{1}Hβ (1.72 ppm), K2 ^{1}Hε (2.917 ppm) and L3 ^{1}Hγ (1.33 ppm), P4 ^{1}Hδ (3.658 ppm) and A ^{1}Hα (1.25 ppm), K2 ^{1}Hε (2.903 ppm) and K2 ^{1}Hδ (1.608 ppm), P4 ^{1}Hβ (2.218 ppm) and P4 ^{1}Hγ, K2 ^{1}Hδ (1.633 ppm) and K2 ^{1}Hε (2.918 ppm), K2 ^{1}Hδ (1.633 ppm) and L3 ^{1}Hδ(0.844 ppm), L3 ^{1}Hδ (0.844 ppm) and R1 ^{1}Hγ (1.517 ppm), L3 ^{1}Hδ (0.844 ppm) and L3 ^{1}Hγ (1.307 ppm), L3 ^{1}Hδ (0.844 ppm) and A ^{1}Hβ (1.241 ppm). The spectrum of this mutant recorded in agarose only produces a few peaks which do not directly correspond to any observed crosspeaks in Figure 3-8.d. Therefore, it can be concluded that the crosspeaks recorded above are the result of changes to secondary structure, as well as surface binding interactions.

3.4 DISCUSSION

3.4.1 *DEST*

DEST experiments have gained traction in recent years for their ability to measure binding interactions of ligand-peptide complexes while dissolved within solution in an expanded timescale to what is offered by STD-NMR and NOESY experiments. Much like in other solution state NMR experiments, the presence of soluble oxides poses an experimental challenge. Unassisted, these nanoparticles will gravitationally settle to the base of the NMR tube, pulling the surface of interest and any attached peptides outside of the 'viewing area' of the coil contained within the probe. Additionally, this settling process would leave a gradient of smaller nanoparticles which would settle slower, skewing the results of the measurement. Agarose gel was used to suspend these particles as described by Egner et al by trapping the nanoparticles within the polysaccharide matrix, while its loose pockets between chains allow the diffusion of smaller ligands and solvent.[103] While invisible to solution NMR experiments due to the stationary nature of the matrix, agarose is not a neutral agent within a sample. Previous literature has shown a positive correlation between the concentration of agarose gel and the measured R1 of water, suggesting that a greater

percentage of water is immobilized by hydrating the matrix as the amount of gel matrix increases. For this reason, it is important that as little agarose gel is used as possible to ensure that the oxide surfaces do not settle.[104] Herein, a relatively low agarose concentration of 1% *w/w* was used, which has been shown experimentally to affect only a minor change in transverse and spin lattice relaxation. However, it would be naïve to assume this interaction with the matrix is limited to just the solvent. DEST profiles, therefore, are measured for the neat peptide, the peptide in agarose, and the peptide exposed to titania within the agarose network. The combination of these three profiles show the unbound behavior of the peptide, and how that changes relative to the environment. Any differences observed between the DEST profiles of the neat peptide and the peptide within the agarose matrix show that a binding interaction is occurring between the peptide and the matrix, and for that reason, analysis focuses on the difference between the DEST profiles of the peptide in agarose and the peptide and titania within the agarose matrix.

Upon quick comparison, the DEST profiles of TBP-P4A and TBP-D5A show significantly more broadening than what is observed in either TBP-R1A and TBP-K2A, suggesting that the binding modes of the former set of peptides adheres to the surface through a stronger interaction than what is observed in the later. Additionally, the DEST profiles of TBP-P4A and TBP-D5A closely mirror prior work by our group investigating the binding of wild-type TBP; very broad peaks were observed across all six residues.

Closer inspection of the DEST profile of TBP-R1A shows broadening of the A ^{1}Hβ and L3 ^{1}Hδ proton profiles. Because resonances for the two arginine residues could not be resolved in any mutant, the combination of spectral contributions of both alanine residues is referred to as simply A without a positional marker. Interestingly, the P4 ^{1}Hδ proton shows broadening upon addition

to agarose with no additional broadening upon the introduction of TBP. This is not observed in any other DEST profile, and the narrow width of the peak suggests that this interaction is not very strong. R1 substitution in binding studies caused a profound decrease in measured peptide binding, therefore it is possible that a binding interaction between TBP-R1A and the agarose matrix could be more favorable than a binding interaction with the titania surface.

Similar inspection of the TBP-K2A profiles show slight unilateral broadening of the R1 $^{1}H\beta$, L3 $^{1}H\delta$, and D5 $^{1}H\beta$ protons. This broadening is not consistent with dark state broadening, but rather with NOE interactions between the proton and proximal nuclei with a negative chemical shift. Therefore, it can be presumed that TBP-K2A is not involved in surface binding with titania. Unlike TBP-R1A, this finding does not match the findings of the early mutation studies. Instead, it corroborates the findings by Suzuki et al who determined through STD-NMR studies that the peptide was most likely binding through its R1 and K2 residues. These DEST profiles show that upon substitution of either the R or K with an alanine residue, the binding is decreased, suggesting that both residues are integral to the ability of TBP to interface with titania. This finding is corroborated by the DEST profiles of both TBP-P4A and TBP-D5A. In both mutants, the R1 and K2 residues are left intact, and both show evidence of strong binding. This suggests that neither the P4 nor the D5 are integral to binding in the regimes that this technique investigates. Once again, these results do not match the findings by Shiba and Sano in their mutation studies, which found that peptide binding drastically fell as a result of P4 and D5 alanine substitution. The discrepancy between these two findings could lie in the nature of the interfacial surface. While our work focused on rutile titania, the titanium used in the quartz crystal microbalance experiments by Shiba and Sano measured the binding of the peptide with titanium particles oxidized by

incubation in hydrogen peroxide at elevated temperatures. No further surface characterization is offered, suggesting that the surface chemistry in each set of experiments could be disparate. As has been shown through MD simulation of amino acids binding to titania, the degree of surface hydroxylation can have a profound difference on the binding behavior and strength of each of the three polar residues within the peptide.[21,23]

3.4.2 *STD-NMR*

As shown throughout literature, difference peaks in STD-NMR spectra have been used to determine the binding mode of peptides to surfaces.[84,87,105,106] In this study, it is used in conjunction with mutation studies to identify the relative importance of different residues on surface binding on a fast timescale. As was discussed in section 3.4.1, the presence of agarose gel necessitates capturing spectra of the peptide within this organic matrix in order to subtract out interactions which may not be attributed to binding interactions between the peptide and the surface.

STD-NMR measurements of TBP-R1A concluded that only the K2 sidechain was in proximity to the surface water layer on the surface of the titania nanoparticle. Previous MD and experimental studies have suggested that both the arginine and lysine residues may compete for binding interactions with the titania surface, therefore it is unsurprising that when arginine is mutated the basic lysine will form a binding interaction with the acidic surface.[20,87] However, the lysine is the only residue which shows evidence of interacting with the titania surface, suggesting a very weak interaction with the surface. Indeed, within the context of the DEST measurements (Figure 3-2), TBP-R1A is shown to be very mobile, suggesting that TBP-R1A could form a transient bond to the titania surface through only its lysine residue. In the case of TBP-K2A, binding interactions

are observed between the agarose and the peptide which are just as strong as those observed when the oxide is added to the matrix. This suggests that upon lysine mutation, it is more favorable for the peptide to bind to the agarose matrix than the oxide surface. However, when both the arginine and lysine sidechains are restored in TBP-P4A and TBP-D5A, strong interaction between the peptide and the surface water layer is observed again. Therefore, these results corroborate the findings of Suzuki et al who found through STD-NMR studies that TBP relies on the R1 and K2 residues for its binding interactions.[87] While these measurements are not able to give a definite mode of binding for the peptide, they do confirm that arginine and lysine support a strong mode of binding in which the entire peptide is held close to the nanoparticle surface.

Compared to other recent STD-NMR work on TBP by Dr. Mengjun Xue, the mutation of the proline and aspartic acid residues may increase the peptide binding by nearly an order of magnitude. This is very contradictory to the findings of Shiba and Sano, who found that mutation of these residues would decrease the overall peptide binding.[22] Other work by Suzuki and coworkers attempt the same analysis, but due to how they normalize the data, a direct comparison to their work is impossible and therefore is not considered in this discussion.[87] The discrepancies observed between the work presented by Shiba and Sano and the work presented herein can be explained through the methods of sample preparation. While high surface area rutile titania nanoparticles were used within this manuscript to study binding, the earlier studies used a battery of protein-containing buffer washes to equalibriate the H_2O_2 oxidized titanium nanoparticles before phage adhesion, suggesting that the two surfaces are not at all comparable.

3.4.3 *NOESY*

Commonly used in determining the structure of proteins in structural biology, NOESY spectra provide information about the secondary and tertiary structure of proteins through the generation of NOE crosspeaks.[107–112] The presence of these peaks signifies the existence of close through-space connections of two heteronuclei found within the same peptide structure. The presence of many cross peaks suggests a high degree of folding, while the lack thereof points to a linear random coil folding pattern. Additionally, the sign of these peaks can be used to determine the rate of motion of measured protons. While negative peaks are indicative of rapid tumbling and reorientations, positive peaks reveal that a particular nucleus is tumbling more slowly. This decrease in local motion can be due to either a folding interaction in which an immobile core is formed, or it can be the result of a binding interaction with a large construct such as a nanoparticle.

The lack of crosspeaks observed in the neat TBP-R1A, TBP-K2A, and TBP-D5A NOESY spectra suggest that all three peptides are linear with very little secondary structure. However, when the proline residue is substituted with an alanine residue in TBP-P4A, the number of crosspeaks increases dramatically, suggesting a radically different secondary structure in which the peptide experiences a greater number of inter-residue contacts. Proline, often referred to in literature as the ‘helix breaker’, is known to force secondary structural changes due to its unique cyclic pyrol functional side chain which encapsulates the backbone amine.[101,102] The replacement of this amino acid with one which permits greater backbone flexibility could therefore result in a more ordered secondary structure, such as what is observed in the NOESY spectrum. The observed interactions between the R1 ^{1}Hγ and the D5 ^{1}Hβ as well as the R1 ^{1}Hβ and L3 ^{1}Hδ would suggest that indeed, this increased flexibility allowed TBP-P4A to adopt increased secondary structure.

In the spectra where oxide is added, after subtracting the contributions of the gel matrix a very similar pattern to what was observed in the STD-NMR and DEST results emerges: TBP-R1A and TBP-K2A do not bind a strongly as TBP-P4A or TBP-D5A. While very few positive crosspeaks are observed upon mutation of the basic residues, crosspeaks which can be assigned to every residue can be located and identified after the basic residues are restored. This would suggest that the lysine and arginine residues facilitate strong peptide binding which immobilizes the entire structure against the slow-tumbling nanoparticle.

3.5 CONCLUSIONS

The work presented herein explores the interaction between the hexapeptide TBP and the rutile titania surface as a function of alanine mutations in order to understand the mechanism of binding. Four alanine mutants were studied through DEST, STD-NMR, and NOESY experiments. DEST studies concluded that TBP-P4A and TBP-D5A both produced a measurable population of surface bound peptides which experience a reduced relaxation rate across their structure. TBP-R1A is only locally tethered at the hydrophobic proline and lysine residues and TBP-K2A appears to experience no binding interactions with the surface. In STD-NMR experiments, binding interactions are observed throughout TBP-P4A and TBP-D5A and at the K2 of TBP-R1A, but no evidence of TBP-K2A interacting with the surface water layer is observed. Finally, NOESY experiments corroborated the other findings, showing that TBP-P4A and TBP-D5A interact with the titania surface, while TBP-R1A and TBP-K2A experience little reduction of their sidechain dynamics. Additionally, NOESY spectra of the neat peptides confirmed the early assertion that the proline residue was constraining the secondary structure. Consequentially, this study has shown the importance of arginine and lysine in TBP binding, and the relative lack of importance of the proline and aspartic acid within this measured timescale of binding.

While the results of these findings are contradictory to those found in earlier works, and with the first chapter of this dissertation, a simple explanation can be offered to tie the sets of experimental data together. Molecular dynamics simulations have shown that as the surface chemistry of the titania changes, so does the preferred mode of peptide binding. Therefore, it is reasonable to assert that in an inhomogeneous landscape such as would be present in a nanoparticle with a high surface area, multiple modes of peptide binding could occur. Earlier work also showed that these different modes of binding would bind with varying strengths, which is captured in different dissociation constants. Because each of the NMR experiments used are only able to detect peptide dissociation within a narrow range of timescales, each experiment is limited in the commentary it is able to provide: STD-NMR and NOESY experiments can only detect rapid transitions on and off of the oxide surface, DEST experiments are best equipped to explore a broader range of timescales from fast to moderately slow, while ΔCS measurements are best suited for static binding modes. Therefore, the discrepancy between the results of the STD-NMR and ΔCS measurements can be interpreted not as a contradiction of one another, but rather the discovery of two discreet modes of peptide binding to the titania surface which occur on different timescales. STD-NMR and NOESY experiments clearly point to a TBP binding mode in which it rapidly exchanges off of the surface using its basic R and K residues as anchors. ΔCS measurements, on the other hand, offer a picture of a very slowly exchanging peptide which binds through its R and D residues.

In short, this study has provided evidence that the adsorption profile of TBP cannot be summed up neatly in a single binding mode. Rather, it paints a picture of binding that is as complicated as the surface it is interacting with. This finding sheds light on the differences observed between the binding isotherms measured on alanine mutations within phage display assays and the current work: differences in surfaces and recorded peptide binding timescales can drastically change the

picture of binding observed. Further work to determine the sidechain dynamics of the amino acid sidechains upon binding can help further isolate a binding profile, while further simulation studies are needed to link the measured structures to a particular surface chemistry.

Chapter 4. SURFACE BINDING OF OSTEOCALCIN

4.1 INTRODUCTION

Osteocalcin (OC) is a small, non-collagenous bone protein which can be found throughout the tissues of most vertebrates.[113–117] While historically this protein has been most closely associated with mineral formation and regulation within bone, dentin, and cementum, a modified form of the protein is often found circulating through the bloodstream and liver tissue, and recent studies have suggested a hormonal function to this mutant.[118–122] The main structural difference between these two species seems to be the presence of γ-carboyglutamic acid (Gla) residues at the 17, 21, and 24 positions, a vitamin K mediated post-translational modification which is acid cleavable in the bone-matrix binding form, while these modifications are largely absent in the free circulating species. While the length and sequence of this peptide varies mildly between species, these modifications are a constant feature, causing this protein to be classified within the family of vitamin K dependant peptides. Throughout this chapter and thesis, only the human species of this peptide is considered, and these two forms of the protein are commonly referred to as carboxylated human osteocalcin (hOC) and decarboxylated human osteocalcin (dhOC).

In humans, hOC is a 49-mer protein which CD measurements have shown to remain largely disordered in aqueous solution apart from a disulphide bridge between Cys23 and Cys29.[42] When calcium salts are added to this solution, however, the protein adopts additional secondary structure. ^{1}H NMR studies have shown the presence of a quasihelical structure between residues 20-26 (α_1), a 3_{10} structure between residues 27-35 (α_2), and a third helix between residues 41-44 (α_3).[123] In the case of hOC, the three Gla residues reside sequestered within the α_1 quasihelix, which X-Ray

Crystallography studies have suggested facilitates an alignment of the Gla functional sidechains which matches the crystal lattice of calcium ions found within the hydroxyapatite (HAP) crystal lattice.[115] This induced conformational re-orientation as well as the alignment of acidic functional sidechains with partially positive centers on the HA surface would suggest that the Gla residues are primarily responsible for HAP interactions.

Recent studies by Scudeller et al investigated the difference in binding affinities and induced structure between hOC and dhOC using a combination of CD measurements, binding assays, and TOF-SIMS analysis of the peptide on the HAP surface.[124] Circular dichroism studies showed that hOC had a higher binding affinity than dhOC, which can most likely be attributed to the reduction in binding moieties between a doubly carboxylated Gla residue and a singly carboxylated Glu. In the case of both proteins, the addition of calcium aided in binding, however, the circular dichroism studies suggest that this increase in binding within dhOC in the presence of calcium is not due to a large conformational change. While hOC undergoes a dramatic change in conformation in the presence of the salt as suggested by previous work, dhOC appears to be more structured in aqueous solution without calcium present, and does not gain much additional structure upon the introduction of the salt. Furthermore, TOF-SIMS measurements suggest that dhOC was more denatured on the surface of HAP than hOC. Together, these two measurements suggest a difference in the mode of binding between these two proteins.

Despite the large body of literature focusing on characterizing this protein, to date there still has not been a study which looks directly at the interactions between hOC and the surface of a mineral. Using a combination of solid and liquid state techniques, this chapter designs the dhOC-α_1 peptide fragment of human osteocalcin (YPDPLEPRREVCELN) as an analogue for the α_1 suspected

binding domain and begins to characterize its method of binding to the surface of HAP and titania. Due to the bulk and complexity as well as its limited commercial availability of both hOC and dhOC, we chose to isolate only the α_1 helical structure and study the binding affinity, structure, and interactions of the peptide with these surfaces. Principally, this chapter is concerned with establishing the viability of dhOC-α1 as a proxy by which to more readily conduct detailed structural and binding studies of the human osteocalcin protein, and further elucidating its interaction with titania to prove the utility of this sequence. CD and ssNMR studies revealed that dhOC-α_1 remained unstructured both in the presence and absence of Ca^{2+} ions, confirming the earlier findings that calcium does not dramatically alter the structure of the decarboxylated peptide. Solid state NMR measurements record the chemical shifts of both the backbone and sidechain chemical shifts. These measurements are used to determine if the peptide undergoes a surface-induced structural rearrangement, and highlights potential candidates for surface binding.

4.2 Experimental Methods

4.2.1 *Materials*

All Fluorenylmethyloxycarbonyl (Fmoc) protected amino acids were purchased from P3 Biosystems (Louisville, KY), and preloaded Fmoc-protected alanine Wang resins were purchased from EMD Millipore (Burlington, MA). Isotopically enriched Fmoc protected residues were purchased from Cambridge Isotope Laboratories (Tewksbury, MA). All other reagents, unless otherwise noted, were purchased from Sigma Aldrich (St. Louis, MO), and used without further purification. All solvents were HPLC grade.

4.2.2 *Peptide Synthesis*

All samples were provided by Dr. Erika Buckle. Arginine residues were double-coupled, with coupling occurring at 25°C for 1500 s. Cysteine residues were single-coupled with coupling occurring at 25°C for 120 s and 50°C for 240 s. All other residues were single-coupled with coupling occurring at 75°C for 15 s and 90°C for 110 s. Peptides were cleaved from the resin using a solution of 88:5:5:2 trifluoroacetic acid (TFA): phenol: water: triisopropylsilane (TIPS); 10 mL of solution was used per 1.0 gram of peptide/resin. The mixture was agitated for 3.5 hours to ensure deprotection of all residues. The resulting filtrate was added drop-wise into 40 mL cold 70:30 ether: hexanes, followed by centrifugation and three rinses of the resulting solids with 40 mL of cold 70:30 ether: hexanes, filtered with a 0.2 µm nylon syringe filter, and purified via HPLC, as described in the subsequent section. Product was confirmed via Electrospray Ionization Mass Spectrometry (ESI-MS).

4.2.3 *Peptide Purification*

Peptides were purified using RP-HPLC (Varian ProStar HPLC, Alltima WP C4 column, 6 mL/min, eluent A: water with 0.2% TFA, eluent B: acetonitrile with 0.2% TFA), using a gradient of 30-50% B over 50 minutes. Chromatograms were generated by observing the UV absorbance at 274 nm, and the analyte was verified by mass spectrometry. The fractions were lyophilized, dissolved in Millipore water, and lyophilized again, resulting in pure peptide.

4.2.4 *ESI-MS*

ESI-MS (Bruker EsquireLC) was used to verify the product and its purity. Analytes were ionized using a positive ESI using the following conditions: 3 kV spray voltage, 350 °C drying gas at 10 L/min, 30 psi nebulizer, 4 kV capillary voltage. Data was collected in full scan mode (mass range

50-2200 m/z) with a scan resolution of 13000 m*sec/z. Ion optic voltages were: 1, 30 V skimmer; 2, 6 V skimmer; 3 V octapole; 100 Vpp octapole RF; 2 V octapole Δ; -5 V lens 1; -60 V lens 2. Bruker Daltonics DataAnlysis software, version 3.0, was used for data acquisition and analysis.

4.2.5 *Preparation of Mineral Oxides*

Both HAP and TiO_2 nanoparticles were pre-treated with a calcium rich solution to promote peptide adhesion as described in previous literature.[125] A stock solution of 100 mM $CaCl_2$ was prepared in water. 30 mg of titania or hydroxyapatite nanoparticles were added to 5 mL of buffer solution, and the mixture was agitated for 30 minutes at room temperature. Samples were centrifuged to form a pellet, the supernatant decanted, and the samples allowed to dry under vacuum overnight.

4.2.6 *Binding Isotherms*

2 mg of calcium treated HAP or titania was weighed into a 1.5 mL microcentrifuge tube and mixed with 1 mL of dhOC-α1 (1, 2, 3, 4, 5, 10, 20, 30, 40, 50, 100 μM) in buffer (20 mM TRIS, 6 mM Ca2+, pH = 7.0). Samples were vortex agitated overnight at room temperature to ensure full binding. A centrifuge was then used to separate the solids into a pellet (13000 xg, 10 minutes), and the supernatant was collected for UV-Vis analysis. A standard curve was prepared of peptide (10, 20, 30, 40, 50, 100 μM), and all spectra were analyzed at λ=274 nm. The amount of bound peptide was calculated by subtracting the measured peptide concentration from the initial concentration, and the results were plotted in Matlab for analysis.

4.2.7 *Circular Dichroism*

All circular dichroism spectra were recorded by Dr. Erika Buckle. Circular dichroism spectra were recorded on a Jasco 720 spectrophotometer at 25° C. Eight scans were recorded within the region

of 190-270 nm at a concentration of 30 μM. Samples recorded in Tris buffer were dissolved in 25 μM Tris, while samples recorded in calcium Tris buffer were dissolved in 25 μM CaCl2 with 25 μM Tris buffer.

4.2.8 *NMR Sample Preparation*

dhOC-α1 was surface adsorbed to titania, and hydroxyapatite in Tris buffer (20 mM, pH=7.0) with 6 mM Ca2+. Mineral oxide was weighed into a 15 mL polypropylene centrifuge tube, and was mixed with the desired amount of dhOC-α1 solution overnight. Samples were then centrifuged at 13000 x g for 10 minutes, the supernatant decanted, and allowed to dry overnight in a vacuum desiccator.

4.2.9 *Solid State NMR Experiments*

All spectra were recorded on a 700 MHz narrow bore spectrometer run by a Bruker Avance III 700 console using either a Bruker TriGamma 3.2 mm HXY MAS probe or a Phoenix 3.2mm wideband HXY MAS probe. The spinning speed for all recorded spectra was 15 kHz ± 5 Hz. ^{13}C spectra were recorded using a ^{1}H 90 pulse length of 3 μs, a contact time between 1-2.5 s, and a recycle delay of 3 s. DARR spectra were recorded with 512-1024 complex points in the direct dimension and 64-128 points in the indirect dimension with mixing times between 15 and 30 ms. Slices were signal-averaged over 512 scans.

4.3 RESULTS

4.3.1 *Binding Isotherms*

Binding of the peptide to both titanium oxide and hydroxyapatite was measured indirectly by recording the UV absorbance of the tyrosine residue of the unbound peptide for an array of starting

peptide concentrations. Fitting of this curve was accomplished using the Langmuir Isotherm model (Equation 1.1), and a confirming a non-cooperative mode of binding. The measured dissociation constants on hydroxyapatite and titania are 0.05 mM and 0.32 mM respectively.

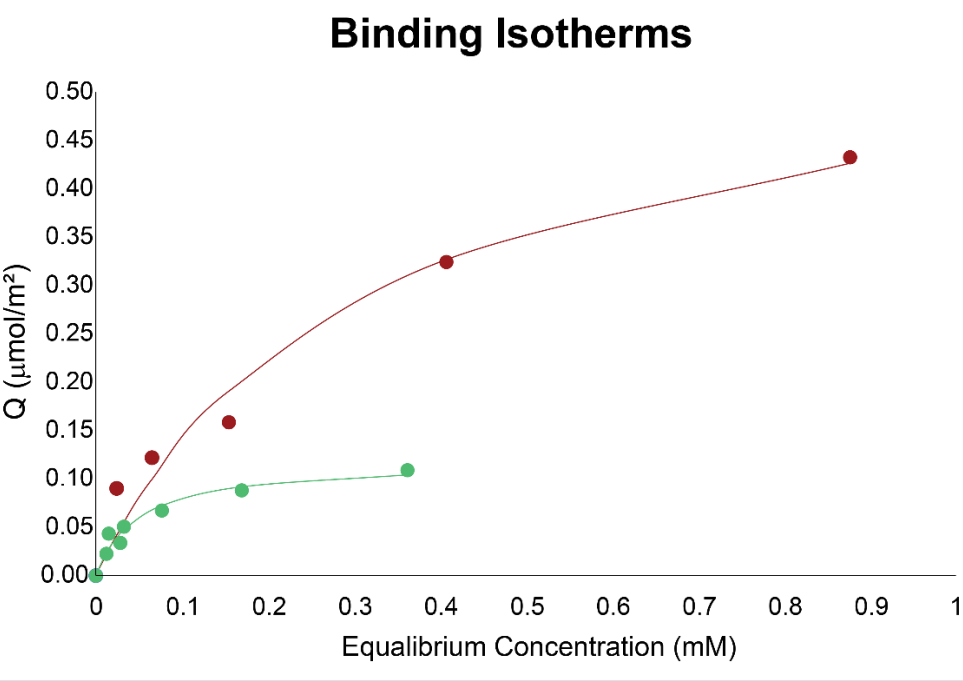

Figure 4-1 dhOC-α_1 binding isotherms on HAP (green) and TiO_2 (red) in the presence of 3mM Ca^{2+}. Data shown are a mean of two repeated measurements, and error bars are too small to be seen. Measured dissociation constants from the fitting are 0.05 mM for HAP and 0.32 mM for TiO_2.

4.3.2 *Circular Dichroism Studies*

The secondary structure of dhOC-α_1 was measured both in the presence and absence of calcium in TRIS-buffered solution using circular dichroism. Much like the reported findings of Schudeller et al, the secondary structure of the protein fragment does not appear to change upon calcium exposure.[124] However, unlike previous findings, this region does not appear to adopt a secondary structure in solution when isolated.

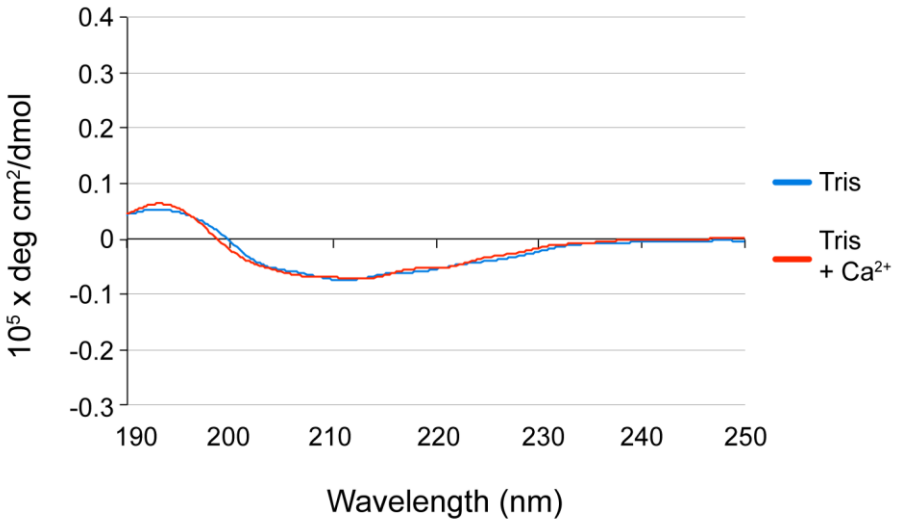

Figure 4-2 Circular Dichroism spectrum of dhOC-a1 in the presence (red) and absence (blue of calcium ions. In both cases, the lack of defined peaks and valleys within the spectrum suggests that the peptide remains random coil in both environments, and that there is no major increase in secondary structure upon the addition of the salt.

4.3.3 *Change in Chemical Shift Analysis*

In order to unambiguously assign chemical shifts and track changes for each residue within the peptide, samples of dhOC-α_1 were synthesized, incorporating up to two ^{13}C isotopically enriched residues as outlined in Table 4-1. The only residues not assigned in this study are the C-terminal N15 and the N-terminal Y1.

Table 4-1 Labeling scheme for dhOC-α_1. Bolded residues proceeded by an asterisk signify the location of uniformly 99.9% ^{13}C enriched residues within the peptide.

Sample Name	Sequence
dhOC-a1(D3L5)	YP***D**P***L**EPRREVCELN
dhOC-a1(P2E6)	Y***P**DPL***E**PRREVCELN
dhOC-a1(R8V11)	YPDPLEP***R**RE***V**CELN
dhOC-a1(R9C12)	YPDPLEPR***R**EV***C**ELN

dhOC-a1(P4E10)	YPD***P**LEPRR***E**VCELN
dhOC-a1(P7E13)	YPDPLE***P**RREVC***E**LN
dhOC-a1(L14)	YPDPLEPRREVCE***L**N

Both 1D ^{13}C CP-MAS and 2D ^{13}C-^{13}C DARR experiments were recorded for each sample, both neat and adsorbed onto TiO_2 nanoparticles. The structures of the investigated amino acids are shown below in Figure 4-3:

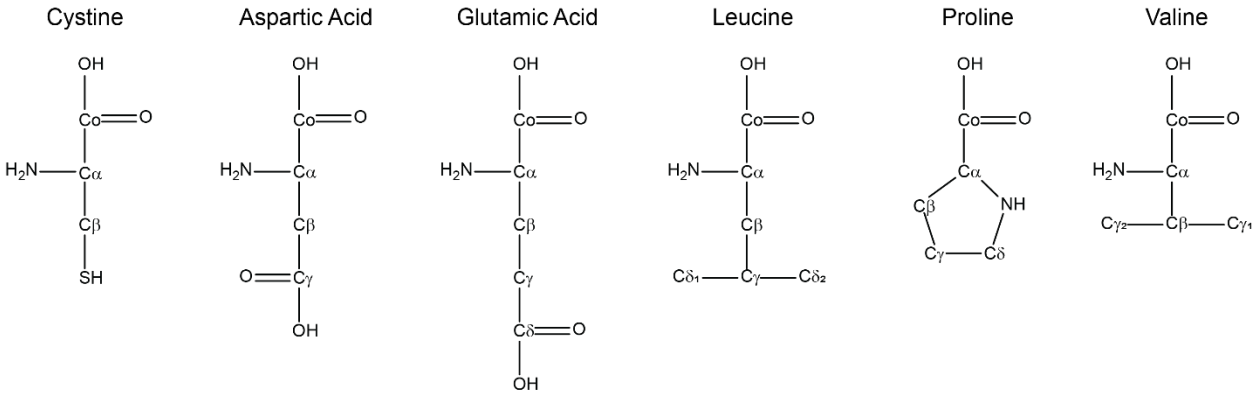

Figure 4-3. Structures of amino acid residues for which chemical shift assignments are made in dhOC-α_1 in neutral conditions (pH=7). Conventional side chain labels are shown.

Recorded DARR spectra of the peptide both neat and surface adsorbed to titania were used to unambiguously assign the resonances of the backbone and sidechain chemical shifts of dhOC-α_1. 2D spectra were used due to its increased resolution from the addition of the indirect dimension. An example of a typical DARR spectrum of a selectively labeled sample is shown below. Traces show how carbon residues were used to ascertain exact resonances.

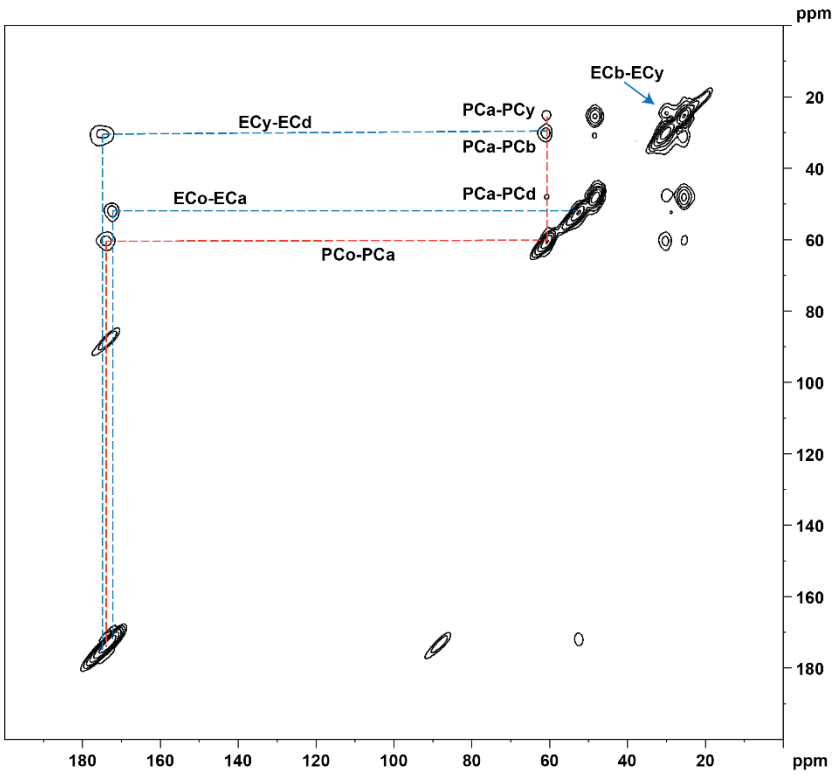

Figure 4-4. ^{13}C-^{13}C DARR spectrum of neat dhOC-α_1-P7E13 showing traces used to assign the ^{13}C spins of the label residues P7 (red) and E13 (blue).

Perturbations of the backbone (Co, Cα, Cβ) chemical shifts between the neat and surface adsorbed samples were recorded and plotted as shown in Figure 4-5. Very large (>5 ppm) upfield perturbations of the E6 $^{13}C\alpha$, E10 $^{13}C\alpha$, C12 ^{13}CO, and E13 $^{13}C\alpha$ are observed. In addition, smaller, but still significant (>1 ppm) upfield shifts of the D3 ^{13}CO and $^{13}C\alpha$, P7 $^{13}C\beta$, R8 ^{13}CO, V11 ^{13}C CO and Cα are observed. In the other direction, very large downfield chemical shifts can be observed in the E6 $^{13}C\beta$, P7 $^{13}C\alpha$, E13 $^{13}C\beta$, and L14 $^{13}C\beta$. Significant downfield shifts are also observed in the P2 ^{13}CO and $^{13}C\alpha$ and $^{13}C\beta$, D3 $^{13}C\beta$, P4 $^{13}C\alpha$ and $^{13}C\beta$, L5 ^{13}CO and $^{13}C\alpha$, E6 ^{13}CO, R8 $^{13}C\alpha$ and $^{13}C\beta$, R9 $^{13}C\alpha$ and $^{13}C\beta$, E10 $^{13}C\beta$, V11 $^{13}C\beta$, C12 $^{13}C\beta$, E13 ^{13}CO, as well as the L14 ^{13}CO and $^{13}C\alpha$. Combined, these large perturbations point to a very significant change in backbone structure upon adsorption to the titania surface.

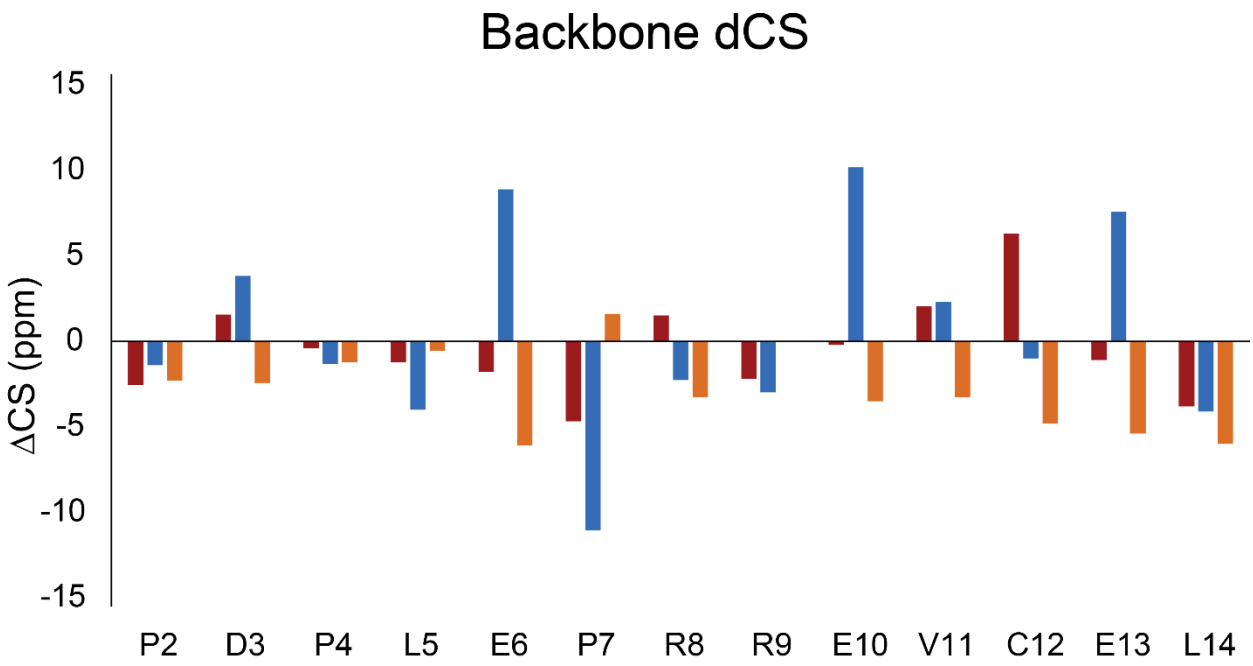

Figure 4-5. Change in chemical shift of the backbone carbons of dhOC-α_1. Peaks in red correspond to the chemical shifts of the ^{13}CO carbons, blue corresponds to the ^{13}Cα carbons, and the orange peaks correspond to the ^{13}Cβ carbons in each assigned residue. Positive changes in chemical shifts correspond to an upfield chemical shift, and likewise, negative changes in chemical shift correspond to a downfield chemical shift.

Similarly, changes in chemical shift were plotted for the side chain residues as shown in Figure 4-6. The E10 ^{13}Cy undergoes a very large upfield chemical shift, and significant upfield chemical shifts can be observed in the D3 ^{13}Cγ, R9 ^{13}Cδ, and E13 ^{13}Cδ. A very large downfield perturbation is observed in the L14 ^{13}Cδ, and the P2 ^{13}Cγ and ^{13}Cδ, P4 ^{13}Cγ, L5 ^{13}Cγ, E6 ^{13}Cγ, P7 ^{13}Cγ and ^{13}Cδ, R8 ^{13}Cγ and ^{13}Cζ, R9 ^{13}Cγ and ^{13}Cζ, V11 ^{13}Cγ, and L14 ^{13}Cγ all experience lesser but still significant downfield perturbations. The very large upfield E10 ^{13}Cγ and significant E13 ^{13}Cδ perturbations could indicate the interactions of these residues with a positively charged surface. This interaction could cause the very large downfield perturbation of the L14 ^{13}Cδ as this residue is pulled into the proximity of a negatively charged deprotonated surface hydroxyl group.

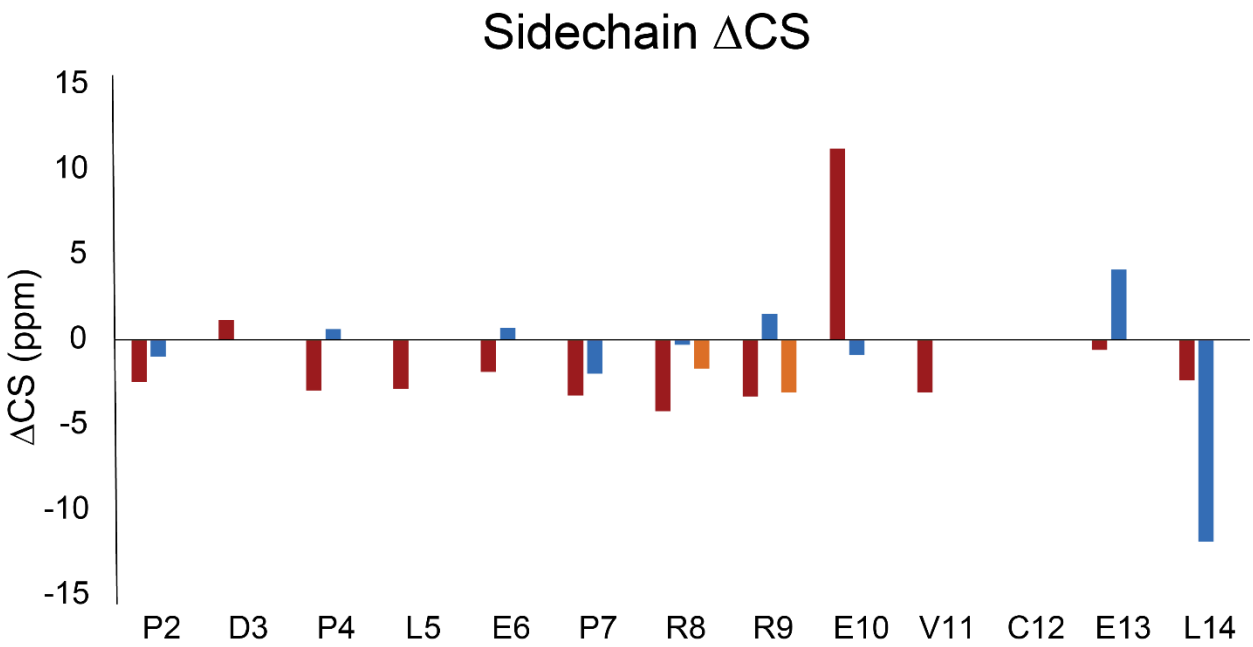

Figure 4-6. Change in chemical shift of the sidechain carbons on dhOC-α_1. Red bars correspond to perturbations in the ^{13}Cγ carbons, blue corresponds to changes in the ^{13}Cδ carbons, and orange shows the changes in chemical shift of the ^{13}Cζ carbons.

4.3.4 *Secondary Structure Visualization*

Chemical shift values of the neat and surface bound peptides were input into the TALOS-N engine, which returned φ/ψ torsion angles for each residue, which were subsequently input into the CHIMERA structural visualization program to produce a three-dimensional rendering of the peptide structure.[79,80] The TALOS-N generated structure for neat dhOC-α_1 is shown in Figure 4-7. All of the φ/ψ torsion angles returned for neat dhOC-α_1 fell outside accepted structural regime values, and therefore are considered to be random coil.

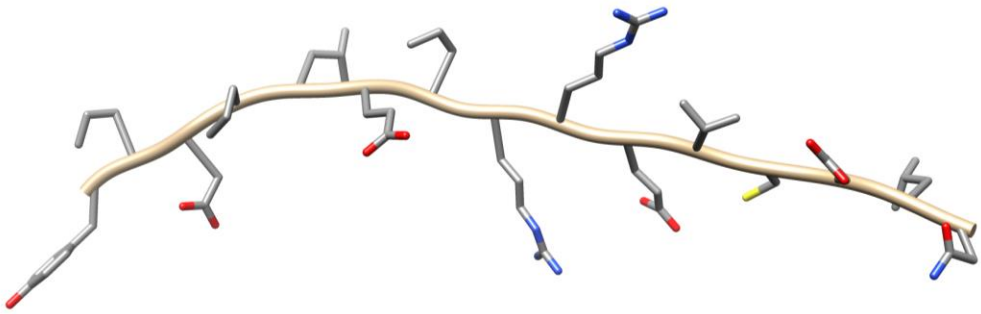

Figure 4-7. Neat solid structure of dhOC-α_1 generated from torsion angles generated by the TALOS-N neural network.

Similar analysis of the returned torsion angles for dhOC-α_1 adsorbed onto titania also return torsion angles which are not indicative of helical or β-sheet character. Visualization of the structure (Figure 4-8) of this peptide based upon these calculated angles reveals a significant perturbation of the backbone chemical shifts, as was suggested by the ΔCS analysis.

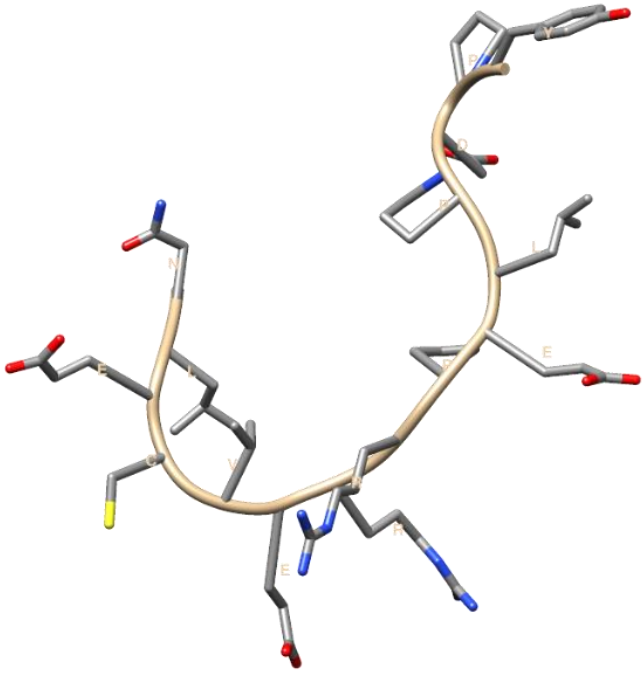

Figure 4-8. CHIMERA visualized structure of dhOC-α_1 bound to titania. Torsion angles were calculated via the TALOS-N neural network.

Upon adsorption to titania, dhOC-α_1 kinks at the E12 and C13 positions, causing the V11 and L14 residues twist inwards and hydrophobically pack. Large perturbations of chemical shift measurements are recorded at these positions. Additionally, backbone rearrangements of the L5 and E6 residues orient the P4 and P7 residues to point towards the packed V11 and L14 residues, creating a hydrophobic core. This folding the polar D3, E6, R8, R8, E10, C12, and E13 residues exposed. Interestingly, only the E6 and E10 sidechains align along the backbone, while the kink at V11 and C12 orients the E13 sidechain away from the other glutamic acid residues.

4.4 DISCUSSION

In order to move forward with the analysis of how dhOC-α_1 binds to a surface, it was first imperative to establish that the peptide fragment behaves in a similar manor to the wild type protein. While circular dichroism studies reveal a more linear backbone structure than what previous studies have reported, fragmentation of the sequence can sometimes cause unraveling due to the lack of constraints which would drive folding in the native sequence. Recent published molecular dynamics structural calculations of the same fragment report a similar unraveling of the backbone structure[126]. The authors attribute this change in secondary structure to an interplay of coulombic and Van der Waals interactions with the surface, as well as the absence of a stabilizing disulfide interaction between the α_1 and α_2 helices present in the full peptide. More importantly, the measured K_d rate constants match those reported in previous literature. Scudeller et al. report a maximum coverage of ~0.4 μmol/m^2 for dhOC in the presence of 3 mM Ca^{2+} and ~0.25 μmol/m^2 in the absence of Ca^{2+} ions.[124] Binding isotherms show that dhOC-α_1 adsorbed to Ca^{2+} soaked titania in the presence of 3 mM Ca^{2+} recorded a maximal coverage of ~0.4 μmol/m^2, while dhOC-α_1 adsorbed to HAP in the presence of 3 mM Ca^{2+} only reached a surface coverage of ~0.10

μmol/m^2. Reduction in surface coverage suggests that the binding mode of dhOC-α_1 is not perfectly analogous to that of the native dhOC protein, let alone a substitute for the carboxylated form. However, recent work has shown the importance of dhOC in biological processes, suggesting that understanding its binding to oxide surfaces may play a role in understanding pathology.[121] Additionally, continuing to study this system will lay the groundwork for future research to benchmark conformational changes against, and for these reasons we decided to proceed with our investigation of this system.

Chemical shift measurements of the backbone (^{13}Co, ^{13}Cα, and ^{13}Cβ) carbons suggest that dhOC-α_1 adopts an extended structure both neat and adsorbed to rutile titania. Large downfield perturbations of the L5 ^{13}Cα (-4.02 ppm), P7 ^{13}Co (-4.69 ppm) and ^{13}Cα (-11.06 ppm) in conjunction with a sizeable upfield chemical shift of the E6 ^{13}Cα suggest a large change in the backbone structure upon adsorption to titania. This supposition is confirmed through visualization of the calculated φ/ψ torsion angles, which show a large bend in the peptide backbone around these residues. Additionally, a second noticeable fold is observed around the C12 and E13 positions. Corresponding chemical shifts are observed in the C12 ^{13}Co (6.30 ppm), the E13 ^{13}Cα (7.56 ppm), as well as the L14 ^{13}Cα (-4.10 ppm) and ^{13}Cβ (-6.00 ppm). Both of these structural rearrangements appear to centralize the hydrophobic L14, V11, P7, and P4 sidechains towards the center of the folded peptide, exposing the more hydrophilic polar residues to interactions with the polar titania surface. It is possible that this rearrangement facilitates such an interaction.

Previous work on osteocalcin has shown a helical structure within the region studied within this work. However, CD measurements (Figure 4-2), neat structure derived from recorded chemical

shift measurements (Figure 4-7), as well as solution NOESY (Figure C-18) measurements unanimously confirm that dhOC-α_1 adopts a linear structure both in the presence and absence of calcium ions. This difference to the native protein could be a result of the fragmentation of the protein, which removed the ability for the peptide to form the disulphide bond and hydrophobic core which have been recorded in previous studies. Without these structural constraints, it is possible that the α_1 region of this protein is unable to form the coiled structure which was postulated to facilitate binding by aligning the glutamic acid residues along a single plane. Lack of such a structure upon interfacing with titania indicates that such a secondary structure may not be advantageous for surface binding. Work by Alamdari and Pfaendtner suggest that when extended, the α_1 fragment can form many interactions between the polar sidechains and the hydroxyl surface of titania.[126]

Change in chemical shift measurements of the sidechain carbon molecules reveal large chemical shifts in the R8 $^{13}C\zeta$ (-1.69 ppm) and R9 $^{13}C\zeta$ (-3.10 ppm). Previous literature has observed binding interactions of peptides with negatively charged oxide surfaces through a salt intermediate which are evidenced by arginine $^{13}C\zeta$ chemical shifts of equal magnitude and sign.[9] Additionally, large sidechain perturbations are observed at the E10 $^{13}C\gamma$ (11.20 ppm) and $^{13}C\delta$ (-0.9 ppm), as well as at the E13 $^{13}C\delta$ (4.10 ppm) and L14 $^{13}C\delta$ (-11.87 ppm) positions. The sign of these changes in chemical shift lend themselves readily to an electrostatic interaction interpretation: a negative ΔCS value would indicate that a carbon is in proximity to an electron-donating negatively charged surface, while a positive ΔCS value would indicate that the residue was approaching an electron-poor positively charged surface. Therefore, in an electrostatic binding interaction for a basic arginine residue we would expect to observe a negative chemical shift, and a positive chemical

shift for an electrostatic binding interaction of an acidic glutamic acid residue. This is observed in the recorded ΔCS measurements of R8, R9, E10, and E13. A similar phenomenon is observed in the D5 $^{13}C\gamma$ residue of TBP as discussed in Chapter 2.3, and has been previously recorded in literature.[127,128] In the case of TBP, it was postulated that the downfield chemical shift resulted from the aspartic acid being tethered to the surface via a Na^{2+} mediated ionic binding interaction. Further molecular dynamics and density functional theory research may confirm the exact nature of the aspartic acid interaction with titania which could produce such ΔCS results. The very large upfield chemical shift observed in the L3 $^{13}C\delta$ is particularly interesting. Leucine is not generally considered a candidate for surface binding due to its hydrophobic sidechain that lacks a pi electron network which can facilitate the interaction of delocalized electrons with the oxide surface.[19,129] The large perturbation of this chemical shift, therefore, is most likely due to its proximity to a negatively charged surface, such as titania. Negative deflections of both the backbone and sidechain ΔCS values suggest that the leucine is experiencing significant conformational rearrangement along the backbone as well as the sidechain. This structural change may force the sidechain into close proximity to an acidic center, or could be the result of a binding interaction between the neighboring E13 residue with the surface.

Folding of the peptide backbone around the V11 residue limits the peptide to only being able to bind through two glutamic residues at any given time. The negative ΔCS values recorded for the R8 and R9 $^{13}C\zeta$ resonances suggest that both residues are directly coupling with the titania surface. Additionally, the large positive ΔCS of the E13 $^{13}C\delta$ suggests a binding interaction between the glutamic acid and the titania facilitated by the presence of a Na^{2+} ion introduced upon adjusting the pH of the TRIS buffer. These binding interactions forbid the interaction of the E6 residue with

the surface, resulting in the very small ΔCS of the E6 $^{13}C\zeta$. E10 also experiences a small ΔCS in its $^{13}C\zeta$, however a large change in chemical shift of the neighboring $^{13}C\gamma$ suggests that this could be due to a sidechain deflection. Nearest neighbor interaction effects have been shown to inhibit the ability of otherwise attractive binding residues to adhere to surfaces.[130] Additionally, these interactions have been shown to drive conformational shifts upon adsorption.[131] Due to the proximity of E10 to two sequential basic residues which show evidence of electrostatic binding with the surface, the recorded ΔCS measurements can be explained by these effects.

4.1 CONCLUSIONS

In this work, a novel peptide fragment of the human osteocalcin protein (dhOC-α_1) is designed and is proven to bind to TiO_2 and hydroxyapatite with equal affinity as what has been previously observed in the native protein, establishing dhOC-α_1 as a viable analogue by which to study the decarboxylated form of human osteocalcin adsorption on oxide surfaces. Furthermore, circular dichroism studies have highlighted significant differences in structure between the native peptide and its fragment within the domain of interest. ΔCS measurements suggest that dhOC-α_1 binds electrostatically to the titania surface through the $^{13}C\zeta$ of R8 and R9, as well as the E13 $^{13}C\delta$ through an ionic intermediate. Calculated torsion angles derived from chemical shift measurements confirm the results of the circular dichroism study, and suggest that the peptide folds upon adsorption to titania as a result of nearest neighbor interactions.

While this investigation makes great strides at understanding the binding interactions of dhOC-α_1 to an oxide surface, an analogous investigation of this system adhered to HAP and SiO_2 are required to tie these findings to the literature. Furthermore, this work could be strengthened

through the interpretation of ΔCS measurements by MD and DFT simulations which produce plausible sidechain orientations from experimental input.

CHAPTER 5. CONCLUSIONS

The growing prosthetic and dental implant industries necessitate the understanding of protein-surface interactions in order to arrest degradation processes that lead to device failure. Integral to understanding these processes, though, is an intimate understanding of the interplay between functional sidechains and the topography of the surfaces they interact with. Solid state NMR has proven to be a crucial tool in understanding these interactions because of its ability to investigate the structure of organic structures both neat and adsorbed on insoluble oxides. This thesis expands upon these techniques, using solution state NMR techniques which are able to study these binding interactions on a fast timescale to compliment the ssNMR findings and paint a wholistic picture of the interactions of peptides across a complex surface. In particular, this work presents a broad picture of TBP interactions with the rutile titania surface through the use of multiple solid and solution state NMR techniques, as well as a solid state study of dhOC-α_1 binding to titania.

Chapter 2 presented a ssNMR study of the interaction of TBP with the titania surface. Binding isotherm studies confirmed the adhesion ability of TBP to titania, and ΔCS measurements ascertained that the peptide was binding to the surface through the aspartic acid via ionic bridging as well as the arginine via electrostatic interactions. The resulting model corroborated earlier findings.

Chapter 3 investigated previous mutation studies on TBP using STD-NMR, NOESY, and DEST solution state NMR techniques to ascertain the relative importance of each residue on peptide binding to titania. All three techniques converged on the conclusion that both the arginine and lysine residues are crucial to TBP binding, while the proline and aspartic acid residues do not

contribute within this faster dynamic timescale. The results of this chapter, when combined with those from Chapter 2 illustrate the affect that a heterogenous surface can have on the binding modes available to a peptide. TBP is interacting with the titania surface by both fast interactions in which its R1 and K2 sidechains form a binding domain, and slow interactions in which it binds through its R1 and D5 functional sidechains.

Finally, chapter 4 introduces the dhOC-α_1 fragment of human osteocalcin as a viable model by which to study the binding interactions of the native peptide. This study proves the binding ability of the fragments and uses circular dichroism measurements to show its lack of structure in solution. Furthermore, ssNMR techniques identify a conformational shift of the peptide upon binding and highlight residues which show evidence of forming the binding domain of the peptide.

In summary, this thesis highlights the versatility of NMR as a tool to study a broad range of systems and their interactions with surfaces through a range of timescales. ssNMR was used to study both the secondary structure and sidechain interactions with inorganic surfaces or buffer salts in the absence of a dynamic medium. STD, NOESY, and DEST experiments successfully studied the dynamic behavior of peptide systems in the presence of a transport medium. The combination of these two classes of techniques captured the complexity of peptide behavior on an inhomogeneous surface, and highlight the necessity of: 1) probing peptide behavior on multiple timescales, 2) understanding how the surface chemistry of an oxide can change the dominant binding mode, and 3) understanding the complexity of surfaces in a research setting.

BIBLIOGRAPHY

(1) Mao, C. M.; Sampath, J.; Sprenger, K. G.; Drobny, G.; Pfaendtner, J. Molecular Driving Forces in Peptide Adsorption to Metal Oxide Surfaces. *Langmuir* **2019**. https://doi.org/10.1021/acs.langmuir.8b01392.

(2) Horinek, D.; Serr, A.; Geisler, M.; Pirzer, T.; Slotta, U.; Lud, S. Q.; Garrido, J. A.; Scheibel, T.; Hugel, T.; Netz, R. R. Peptide Adsorption on a Hydrophobic Surface Results from an Interplay of Solvation, Surface, and Intrapeptide Forces. *Proc. Natl. Acad. Sci. U. S. A.* **2008**. https://doi.org/10.1073/pnas.0707879105.

(3) Wu, C.; Skelton, A. A.; Chen, M.; Vlček, L.; Cummings, P. T. Modeling the Interaction between Integrin-Binding Peptide (RGD) and Rutile Surface: The Effect of Cation Mediation on Asp Adsorption. *Langmuir* **2012**. https://doi.org/10.1021/la204329d.

(4) Langmuir, I. The Adsorption of Gases on Plane Surfaces of Glass, Mica and Platinum. *J. Am. Chem. Soc.* **1918**. https://doi.org/10.1021/ja02242a004.

(5) HILL, A. The Possible Effects of the Aggregation of the Molecules of Haemoglobin on Its Dissociation Curves. *J Physiol* **1910**.

(6) Hruby, V. J.; Mosberg, H. I. Conformational and Dynamic Considerations in Peptide Structure-Function Studies. *Peptides* **1982**, *3* (3), 329–336. https://doi.org/https://doi.org/10.1016/0196-9781(82)90095-X.

(7) Shaw, W. J. Solid-State NMR Studies of Proteins Immobilized on Inorganic Surfaces. *Solid State Nuclear Magnetic Resonance*. 2015. https://doi.org/10.1016/j.ssnmr.2014.10.003.

(8) Buckle, E. L.; Prakash, A.; Bonomi, M.; Sampath, J.; Pfaendtner, J.; Drobny, G. P. Solid-State NMR and MD Study of the Structure of the Statherin Mutant SNa15 on Mineral Surfaces. *J. Am. Chem. Soc.* **2019**. https://doi.org/10.1021/jacs.8b10990.

(9) Buckle, E. L.; Roehrich, A.; Vandermoon, B.; Drobny, G. P. Comparative Study of Secondary Structure and Interactions of the R5 Peptide in Silicon Oxide and Titanium Oxide Coprecipitates Using Solid-State NMR Spectroscopy. *Langmuir* **2017**, *33* (40), 10517–10524. https://doi.org/10.1021/acs.langmuir.7b01048.

(10) Zane, A. C.; Michelet, C.; Roehrich, A.; Emani, P. S.; Drobny, G. P. Silica Morphogenesis by Lysine-Leucine Peptides with Hydrophobic Periodicity. *Langmuir* **2014**. https://doi.org/10.1021/la501444t.

(11) Lu, J. X.; Xu, Y. S.; Buchko, G. W.; Shaw, W. J. Mineral Association Changes the Secondary Structure and Dynamics of Murine Amelogenin. *J. Dent. Res.* **2013**. https://doi.org/10.1177/0022034513504929.

(12) Shaw, W. J.; Ferris, K. Structure, Orientation, and Dynamics of the C-Terminal Hexapeptide of LRAP Determined Using Solid-State NMR. *J. Phys. Chem. B* **2008**. https://doi.org/10.1021/jp808012g.

(13) Sprenger, K. G.; Prakash, A.; Drobny, G.; Pfaendtner, J. Investigating the Role of Phosphorylation in the Binding of Silaffin Peptide R5 to Silica with Molecular Dynamics Simulations. *Langmuir* **2018**, *34* (3). https://doi.org/10.1021/acs.langmuir.7b02868.

(14) LEVINE, M. J. Salivary Macromolecules: A Structure/Function Synopsis. *Ann. N. Y. Acad. Sci.* **1993**. https://doi.org/10.1111/j.1749-6632.1993.tb18337.x.

(15) Luo, M.; Gao, Y.; Yang, S.; Quan, X.; Sun, D.; Liang, K.; Li, J.; Zhou, J. Computer Simulations of the Adsorption of an N-Terminal Peptide of Statherin, SN15, and Its Mutants on Hydroxyapatite Surfaces. *Phys. Chem. Chem. Phys.* **2019**.

https://doi.org/10.1039/c9cp01638d.
(16) Roehrich, A.; Drobny, G. Solid-State NMR Studies of Biomineralization Peptides and Proteins. *Acc. Chem. Res.* **2013**, *46* (9), 2136–2144. https://doi.org/10.1021/ar300321e.
(17) Li, K.; Emani, P. S.; Ash, J.; Groves, M.; Drobny, G. P. A Study of Phenylalanine Side-Chain Dynamics in Surface-Adsorbed Peptides Using Solid-State Deuterium NMR and Rotamer Library Statistics. *J. Am. Chem. Soc.* **2014**. https://doi.org/10.1021/ja504677d.
(18) Gibson, J. M.; Popham, J. M.; Raghunathan, V.; Stayton, P. S.; Drobny, G. P. A Solid-State NMR Study of the Dynamics and Interactions of Phenylalanine Rings in a Statherin Fragment Bound to Hydroxyapatite Crystals. *J. Am. Chem. Soc.* **2006**. https://doi.org/10.1021/ja056731m.
(19) Sultan, A. M.; Hughes, Z. E.; Walsh, T. R. Binding Affinities of Amino Acid Analogues at the Charged Aqueous Titania Interface: Implications for Titania-Binding Peptides. *Langmuir* **2014**, *30* (44), 13321–13329. https://doi.org/10.1021/la503312d.
(20) Skelton, A. A.; Liang, T.; Walsh, T. R. Interplay of Sequence, Conformation, and Binding at the Peptide?Titania Interface as Mediated by Water. *ACS Appl. Mater. Interfaces* **2009**, *1* (7), 1482–1491. https://doi.org/10.1021/am9001666.
(21) Sampath, J.; Kullman, A.; Gebhart, R.; Drobny, G.; Pfaendtner, J. Molecular Recognition and Specificity of Biomolecules to Titanium Dioxide from Molecular Dynamics Simulations. *npj Comput. Mater.* **2020**. https://doi.org/10.1038/s41524-020-0288-7.
(22) Sano, K. I.; Shiba, K. A Hexapeptide Motif That Electrostatically Binds to the Surface of Titanium. *J. Am. Chem. Soc.* **2003**, *125* (47), 14234–14235. https://doi.org/10.1021/ja038414q.
(23) xue, mengjun; Sampath, J.; Gebhart, R.; Haugen, H. J.; Lyngstadaas, S. P.; Pfaendtner, J.; Drobny, G. P. Studies of Dynamic Binding of Amino Acids to TiO2 Nanoparticle Surfaces by Solution NMR and Molecular Dynamics Simulations. *Langmuir* **2020**. https://doi.org/10.1021/acs.langmuir.0c01256.
(24) Fernandez, V. L.; Reimer, J. A.; Denn, M. M. Magnetic Resonance Studies of Polypeptides Adsorbed on Silica and Hydroxyapatite Surfaces. *J. Am. Chem. Soc.* **1992**, *114* (24), 9634–9642. https://doi.org/10.1021/ja00050a051.
(25) Razvag, Y.; Gutkin, V.; Reches, M. Probing the Interaction of Individual Amino Acids with Inorganic Surfaces Using Atomic Force Spectroscopy. *Langmuir* **2013**, *29* (32), 10102–10109. https://doi.org/10.1021/la4015866.
(26) Gao, Q.; Xu, W.; Xu, Y.; Wu, D.; Sun, Y.; Deng, F.; Shen, W. Amino Acid Adsorption on Mesoporous Materials: Influence of Types of Amino Acids, Modification of Mesoporous Materials, and Solution Conditions. *J. Phys. Chem. B* **2008**, *112* (7), 2261–2267. https://doi.org/10.1021/jp0763580.
(27) Ndao, M.; Ash, J. T.; Breen, N. F.; Goobes, G.; Stayton, P. S.; Drobny, G. P. A 13C{ 31P} REDOR NMR Investigation of the Role of Glutamic Acid Residues in Statherin-Hydroxyapatite Recognition. *Langmuir* **2009**. https://doi.org/10.1021/la901647n.
(28) Shaw, W. J.; Long, J. R.; Dindot, J. L.; Campbell, A. A.; Stayton, P. S.; Drobny, G. P. Determination of Statherin N-Terminal Peptide Conformation on Hydroxyapatite Crystals. *J. Am. Chem. Soc.* **2000**. https://doi.org/10.1021/ja9842823.
(29) Gibson, J. M.; Raghunathan, V.; Popham, J. M.; Stayton, P. S.; Drobny, G. P. A REDOR NMR Study of a Phosphorylated Statherin Fragment Bound to Hydroxyapatite Crystals. *J. Am. Chem. Soc.* **2005**. https://doi.org/10.1021/ja050910m.
(30) Buckle, E. L.; Lum, J. S.; Roehrich, A. M.; Stote, R. E.; Vandermoon, B.; Dracinsky, M.;

Filocamo, S. F.; Drobny, G. P. Serine–Lysine Peptides as Mediators for the Production of Titanium Dioxide: Investigating the Effects of Primary and Secondary Structures Using Solid-State NMR Spectroscopy and DFT Calculations. *J. Phys. Chem. B* **2018**, *122* (17), 4708–4718. https://doi.org/10.1021/acs.jpcb.8b00745.

(31) Roehrich, A.; Drobny, G. Solid-State NMR Studies of Biomineralization Peptides and Proteins. *Acc. Chem. Res.* **2013**. https://doi.org/10.1021/ar300321e.

(32) Ceccon, A.; Tugarinov, V.; Clore, G. M. TiO 2 Nanoparticles Catalyze Oxidation of Huntingtin Exon 1-Derived Peptides Impeding Aggregation: A Quantitative NMR Study of Binding and Kinetics. *J. Am. Chem. Soc.* **2019**. https://doi.org/10.1021/jacs.8b11441.

(33) Zhang, Y.; Xu, H.; Parsons, A. M.; Casabianca, L. B. Examining Binding to Nanoparticle Surfaces Using Saturation Transfer Difference (STD)-NMR Spectroscopy. *J. Phys. Chem. C* **2017**. https://doi.org/10.1021/acs.jpcc.7b08828.

(34) Raghunathan, V.; Gibson, J. M.; Goobes, G.; Popham, J. M.; Louie, E. A.; Stayton, P. S.; Drobny, G. P. Homonuclear and Heteronuclear NMR Studies of a Statherin Fragment Bound to Hydroxyapatite Crystals. *J. Phys. Chem. B* **2006**. https://doi.org/10.1021/jp056644g.

(35) Raj, P. A.; Johnsson, M.; Levine, M. J.; Nancollas, G. H. Salivary Statherin. Dependence on Sequence, Charge, Hydrogen Bonding Potency, and Helical Conformation for Adsorption to Hydroxyapatite and Inhibition of Mineralization. *J. Biol. Chem.* **1992**.

(36) Notman, R.; Walsh, T. R. Molecular Dynamics Studies of the Interactions of Water and Amino Acid Analogues with Quartz Surfaces. *Langmuir* **2009**. https://doi.org/10.1021/la803324x.

(37) Egner, T. K.; Naik, P.; An, Y.; Venkatesh, A.; Rossini, A. J.; Slowing, I. I.; Venditti, V. 'Surface Contrast' NMR Reveals Non-Innocent Role of Support in Pd/CeO2 Catalyzed Phenol Hydrogenation. *ChemCatChem* **2020**. https://doi.org/10.1002/cctc.202000608.

(38) Weidner, T.; Dubey, M.; Breen, N. F.; Ash, J.; Baio, J. E.; Jaye, C.; Fischer, D. A.; Drobny, G. P.; Castner, D. G. Direct Observation of Phenylalanine Orientations in Statherin Bound to Hydroxyapatite Surfaces. *J. Am. Chem. Soc.* **2012**. https://doi.org/10.1021/ja301711w.

(39) Koutsopoulos, S.; Dalas, E. Inhibition of Hydroxyapatite Formation in Aqueous Solutions by Amino Acids with Hydrophobic Side Groups. *Langmuir* **2000**. https://doi.org/10.1021/la000057z.

(40) Goobes, G.; Goobes, R.; Schueler-Furman, O.; Baker, D.; Stayton, P. S.; Drobny, G. P. Folding of the C-Terminal Bacterial Binding Domain in Statherin upon Adsorption onto Hydroxyapatite Crystals. *Proc. Natl. Acad. Sci. U. S. A.* **2006**. https://doi.org/10.1073/pnas.0607193103.

(41) Dowd, T. L.; Li, L.; Gundberg, C. M. The 1H NMR Structure of Bovine Pb2+-Osteocalcin and Implications for Lead Toxicity. *Biochim. Biophys. Acta - Proteins Proteomics* **2008**. https://doi.org/10.1016/j.bbapap.2008.08.010.

(42) Atkinson, R. A.; Evans, J. S.; Hauschka, P. V; Levine, B. A.; Meats, R.; Triffitt, J. T.; Virdi, A. S.; Wiliams, R. J. P. Conformational Studies of Oosteocalcin in Solution. *Eur. J. Biochem.* **1995**, *232* (2), 515–521. https://doi.org/10.1111/j.1432-1033.1995.515zz.x.

(43) Cook, S. D.; Thomas, K. A.; Kay, J. F.; Jarcho, M. Hydroxyapatite-Coated Titanium for Orthopedic Implant Applications. *Clinical Orthopaedics and Related Research*. 1988. https://doi.org/10.1097/00003086-198807000-00030.

(44) Latysh, V.; Krallics, G.; Alexandrov, I.; Fodor, A. Application of Bulk Nanostructured

Materials in Medicine. In *Current Applied Physics*; 2006. https://doi.org/10.1016/j.cap.2005.07.053.

(45) Li, Y.; Yang, C.; Zhao, H.; Qu, S.; Li, X.; Li, Y. New Developments of Ti-Based Alloys for Biomedical Applications. *Materials*. 2014. https://doi.org/10.3390/ma7031709.

(46) Allen, N. S.; Edge, M.; Verran, J.; Stratton, J.; Maltby, J.; Bygott, C. Photocatalytic Titania Based Surfaces: Environmental Benefits. *Polym. Degrad. Stab.* **2008**. https://doi.org/10.1016/j.polymdegradstab.2008.04.015.

(47) Ismail, A. A.; Bahnemann, D. W. Mesoporous Titania Photocatalysts: Preparation, Characterization and Reaction Mechanisms. *Journal of Materials Chemistry*. 2011. https://doi.org/10.1039/c1jm10407a.

(48) Davis, R. J.; Liu, Z. Titania-Silica: A Model Binary Oxide Catalyst System. *Chemistry of Materials*. 1997. https://doi.org/10.1021/cm970314u.

(49) Bagheri, S.; Muhd Julkapli, N.; Bee Abd Hamid, S. Titanium Dioxide as a Catalyst Support in Heterogeneous Catalysis. *Scientific World Journal*. 2014. https://doi.org/10.1155/2014/727496.

(50) Hadjiivanov, K. I.; Klissurski, D. G. Surface Chemistry of Titania (Anatase) and Titania-Supported Catalysts. *Chem. Soc. Rev.* **1996**. https://doi.org/10.1039/cs9962500061.

(51) Vittadini, A.; Casarin, M.; Selloni, A. Chemistry of and on TiO2-Anatase Surfaces by DFT Calculations: A Partial Review. *Theor. Chem. Acc.* **2007**. https://doi.org/10.1007/s00214-006-0191-4.

(52) Henderson, M. A. Structural Sensitivity in the Dissociation of Water on TiO2 Single-Crystal Surfaces. *Langmuir* **1996**. https://doi.org/10.1021/la960360t.

(53) Blomquist, J.; Walle, L. E.; Uvdal, P.; Borg, A.; Sandell, A. Water Dissociation on Single Crystalline Anatase TiO2(001) Studied by Photoelectron Spectroscopy. *J. Phys. Chem. C* **2008**. https://doi.org/10.1021/jp805664b.

(54) Fahmi, A.; Minot, C. A Theoretical Investigation of Water Adsorption on Titanium Dioxide Surfaces. *Surf. Sci.* **1994**. https://doi.org/10.1016/0039-6028(94)91345-5.

(55) Mahdavi-Shakib, A.; Husremovic, S.; Ki, S.; Glynn, J.; Babb, L.; Sempel, J.; Stavrinoudis, I.; Arce-Ramos, J. M.; Nelson, R.; Grabow, L. C.; Schwartz, T. J.; Frederick, B. G.; Austin, R. N. Titania Surface Chemistry and Its Influence on Supported Metal Catalysts. *Polyhedron* **2019**. https://doi.org/10.1016/j.poly.2019.05.012.

(56) Bourikas, K.; Kordulis, C.; Lycourghiotis, A. Titanium Dioxide (Anatase and Rutile): Surface Chemistry, Liquid-Solid Interface Chemistry, and Scientific Synthesis of Supported Catalysts. *Chemical Reviews*. 2014. https://doi.org/10.1021/cr300230q.

(57) Roddick-Lanzilotta, A. D.; McQuillan, A. J. An in Situ Infrared Spectroscopic Study of Glutamic Acid and of Aspartic Acid Adsorbed on TiO2: Implications for the Biocompatibility of Titanium. *J. Colloid Interface Sci.* **2000**. https://doi.org/10.1006/jcis.2000.6864.

(58) Roddick-Lanzilotta, A. D.; Connor, P. A.; McQuillan, A. J. An in Situ Infrared Spectroscopic Study of the Adsorption of Lysine to TiO2 from an Aqueous Solution. *Langmuir* **1998**. https://doi.org/10.1021/la980425n.

(59) Alan, B. O.; Barisik, M.; Ozcelik, H. G. Roughness Effects on the Surface Charge Properties of Silica Nanoparticles. *J. Phys. Chem. C* **2020**. https://doi.org/10.1021/acs.jpcc.0c00120.

(60) Abbas, Z.; Labbez, C.; Nordholm, S.; Ahlberg, E. Size-Dependent Surface Charging of Nanoparticles. *J. Phys. Chem. C* **2008**. https://doi.org/10.1021/jp709667u.

(61) Lundqvist, M.; Sethson, I.; Jonsson, B. H. Protein Adsorption onto Silica Nanoparticles: Conformational Changes Depend on the Particles' Curvature and the Protein Stability. *Langmuir* **2004**. https://doi.org/10.1021/la0484725.
(62) Shang, W.; Nuffer, J. H.; Muñiz-Papandrea, V. A.; Colón, W.; Siegel, R. W.; Dordick, J. S. Cytochrome c on Silica Nanoparticles: Influence of Nanoparticle Size on Protein Structure, Stability, and Activity. *Small* **2009**. https://doi.org/10.1002/smll.200800995.
(63) Levitt, M. H. *Spin Dynamics : Basics of Nuclear Magnetic Resonance*; 2000.
(64) Sørensen, O. W. James Keeler. Understanding NMR Spectroscopy. *Magn. Reson. Chem.* **2006**. https://doi.org/10.1002/mrc.1798.
(65) Bax, A.; Davis, D. G. MLEV-17-Based Two-Dimensional Homonuclear Magnetization Transfer Spectroscopy. *J. Magn. Reson.* **1985**. https://doi.org/10.1016/0022-2364(85)90018-6.
(66) Hwang, T. L.; Shaka, A. J. Water Suppression That Works. Excitation Sculpting Using Arbitrary Wave-Forms and Pulsed-Field Gradients. *J. Magn. Reson. - Ser. A* **1995**. https://doi.org/10.1006/jmra.1995.1047.
(67) Anthis, N. J.; Clore, G. M. Visualizing Transient Dark States by NMR Spectroscopy. *Q. Rev. Biophys.* **2015**. https://doi.org/10.1017/S0033583514000122.
(68) Magic Angle Spinning in Solid State n.m.r. Spectroscopy. *Philos. Trans. R. Soc. London. Ser. A, Math. Phys. Sci.* **1981**. https://doi.org/10.1098/rsta.1981.0032.
(69) Duer, M. J. *Solid-State NMR Spectroscopy Principles and Applications*; 2007. https://doi.org/10.1002/9780470999394.
(70) Takegoshi, K.; Nakamura, S.; Terao, T. 13C-1H Dipolar-Assisted Rotational Resonance in Magic-Angle Spinning NMR. *Chem. Phys. Lett.* **2001**, *344* (5–6), 631–637. https://doi.org/10.1016/S0009-2614(01)00791-6.
(71) Takegoshi, K.; Nakamura, S.; Terao, T. 13C-1H Dipolar-Driven 13C-13C Recoupling without 13C Rf Irradiation in Nuclear Magnetic Resonance of Rotating Solids. *J. Chem. Phys.* **2003**. https://doi.org/10.1063/1.1534105.
(72) Hovmöller, S.; Zhou, T.; Ohlson, T. Conformations of Amino Acids in Proteins. *Acta Crystallogr. Sect. D Biol. Crystallogr.* **2002**. https://doi.org/10.1107/S0907444902003359.
(73) De Dios, A. C.; Pearson, J. G.; Oldfield, E. Secondary and Tertiary Structural Effects on Protein NMR Chemical Shifts: An Ab Initio Approach. *Science (80-.).* **1993**. https://doi.org/10.1126/science.8502992.
(74) Wishart, D. S.; Sykes, B. D. The 13C Chemical-Shift Index: A Simple Method for the Identification of Protein Secondary Structure Using 13C Chemical-Shift Data. *J. Biomol. NMR* **1994**. https://doi.org/10.1007/BF00175245.
(75) Wishart, D. S. Interpreting Protein Chemical Shift Data. *Progress in Nuclear Magnetic Resonance Spectroscopy*. 2011. https://doi.org/10.1016/j.pnmrs.2010.07.004.
(76) Saitô, H. Conformation-dependent 13C Chemical Shifts: A New Means of Conformational Characterization as Obtained by High-resolution Solid-state 13C NMR. *Magnetic Resonance in Chemistry*. 1986. https://doi.org/10.1002/mrc.1260241002.
(77) Spera, S.; Bax, A. Empirical Correlation between Protein Backbone Conformation and Cα and Cβ 13C Nuclear Magnetic Resonance Chemical Shifts. *J. Am. Chem. Soc.* **1991**. https://doi.org/10.1021/ja00014a071.
(78) Robustelli, P.; Stafford, K. A.; Palmer, A. G. Interpreting Protein Structural Dynamics from NMR Chemical Shifts. *J. Am. Chem. Soc.* **2012**. https://doi.org/10.1021/ja300265w.
(79) Shen, Y.; Bax, A. Protein Backbone and Sidechain Torsion Angles Predicted from NMR

Chemical Shifts Using Artificial Neural Networks. *J. Biomol. NMR* **2013**, *56* (3), 227–241. https://doi.org/10.1007/s10858-013-9741-y.

(80) Pettersen, E. F.; Goddard, T. D.; Huang, C. C.; Couch, G. S.; Greenblatt, D. M.; Meng, E. C.; Ferrin, T. E. UCSF Chimera - A Visualization System for Exploratory Research and Analysis. *J. Comput. Chem.* **2004**. https://doi.org/10.1002/jcc.20084.

(81) Jones, F. H. Teeth and Bones: Applications of Surface Science to Dental Materials and Related Biomaterials. *Surface Science Reports*. 2001. https://doi.org/10.1016/S0167-5729(00)00011-X.

(82) Vallee, A.; Humblot, V.; Pradier, C. M. Peptide Interactions with Metal and Oxide Surfaces. *Acc. Chem. Res.* **2010**. https://doi.org/10.1021/ar100017n.

(83) Sultan, A. M.; Hughes, Z. E.; Walsh, T. R. Effect of Calcium Ions on Peptide Adsorption at the Aqueous Rutile Titania (110) Interface. *Biointerphases* **2018**. https://doi.org/10.1116/1.5046531.

(84) Mirau, P. A.; Naik, R. R.; Gehring, P. Structure of Peptides on Metal Oxide Surfaces Probed by NMR. *J. Am. Chem. Soc.* **2011**, *133* (45), 18243–18248. https://doi.org/10.1021/ja205454t.

(85) Puddu, V.; Slocik, J. M.; Naik, R. R.; Perry, C. C. Titania Binding Peptides as Templates in the Biomimetic Synthesis of Stable Titania Nanosols: Insight into the Role of Buffers in Peptide-Mediated Mineralization. *Langmuir* **2013**. https://doi.org/10.1021/la401777x.

(86) Hayashi, T.; Sano, K. I.; Shiba, K.; Iwahori, K.; Yamashita, I.; Hara, M. Critical Amino Acid Residues for the Specific Binding of the Ti-Recognizing Recombinant Ferritin with Oxide Surfaces of Titanium and Silicon. *Langmuir* **2009**, *25* (18), 10901–10906. https://doi.org/10.1021/la901242q.

(87) Suzuki, Y.; Shindo, H.; Asakura, T. Structure and Dynamic Properties of a Ti-Binding Peptide Bound to TiO 2 Nanoparticles As Accessed by 1 H NMR Spectroscopy. *J. Phys. Chem. B* **2016**, *120* (20), 4600–4607. https://doi.org/10.1021/acs.jpcb.6b03260.

(88) Coin, I.; Beyermann, M.; Bienert, M. Solid-Phase Peptide Synthesis: From Standard Procedures to the Synthesis of Difficult Sequences. *Nat. Protoc.* **2007**, *2* (12), 3247–3256. https://doi.org/10.1038/nprot.2007.454.

(89) R Development Core Team. R: A Language and Environment for Statistical Computing. *R Found. Stat. Comput. Vienna Austria* **2016**. https://doi.org/10.1038/sj.hdy.6800737.

(90) Bennett, A. E.; Rienstra, C. M.; Auger, M.; Lakshmi, K. V.; Griffin, R. G. Heteronuclear Decoupling in Rotating Solids. *J. Chem. Phys.* **1995**, *103* (16), 6951–6958. https://doi.org/10.1063/1.470372.

(91) Morcombe, C. R.; Zilm, K. W. Chemical Shift Referencing in MAS Solid State NMR. *J. Magn. Reson.* **2003**, *162* (2), 479–486. https://doi.org/10.1016/S1090-7807(03)00082-X.

(92) Gullion, T.; Schaefer, J. Rotational-Echo Double-Resonance NMR. *J. Magn. Reson.* **1989**, *81* (1), 196–200. https://doi.org/10.1016/0022-2364(89)90280-1.

(93) Soto, C.; Castano, E. M.; Frangione, B.; Inestrosa, N. C. The α-Helical to β-Strand Transition in the Amino-Terminal Fragment of the Amyloid β-Peptide Modulates Amyloid Formation. *J. Biol. Chem.* **1995**. https://doi.org/10.1074/jbc.270.7.3063.

(94) Gkountelias, K.; Tselios, T.; Venihaki, M.; Deraos, G.; Lazaridis, I.; Rassouli, O.; Gravanis, A.; Liapakis, G. Alanine Scanning Mutagenesis of the Second Extracellular Loop of Type 1 Corticotropin-Releasing Factor Receptor Revealed Residues Critical for Peptide Binding. *Mol. Pharmacol.* **2009**. https://doi.org/10.1124/mol.108.052423.

(95) Koole, C.; Wootten, D.; Simms, J.; Savage, E. E.; Miller, L. J.; Christopoulos, A.; Sexton,

P. M. Second Extracellular Loop of Human Glucagon-like Peptide-1 Receptor (GLP-1R) Differentially Regulates Orthosteric but Not Allosteric Agonist Binding and Function. *J. Biol. Chem.* **2012**. https://doi.org/10.1074/jbc.M111.309369.

(96) Ahn, K. H.; Bertalovitz, A. C.; Mierke, D. F.; Kendall, D. A. Dual Role of the Second Extracellular Loop of the Cannabinoid Receptor 1: Ligand Binding and Receptor Localization. *Mol. Pharmacol.* **2009**. https://doi.org/10.1124/mol.109.057356.

(97) Drummer, H. E.; Poumbourios, P. Hepatitis C Virus Glycoprotein E2 Contains a Membrane-Proximal Heptad Repeat Sequence That Is Essential for E1E2 Glycoprotein Heterodimerization and Viral Entry. *J. Biol. Chem.* **2004**. https://doi.org/10.1074/jbc.M405098200.

(98) Carter, P. H.; Shimizu, M.; Luck, M. D.; Gardella, T. J. The Hydrophobic Residues Phenylalanine 184 and Leucine 187 in the Type-1 Parathyroid Hormone (PTH) Receptor Functionally Interact with the Amino- Terminal Portion of PTH-(1-34). *J. Biol. Chem.* **1999**. https://doi.org/10.1074/jbc.274.45.31955.

(99) Dickinson, C. D.; Kelly, C. R.; Ruf, W.; Huber, R. *Identification of Surface Residues Mediating Tissue Factor Binding and Catalytic Function of the Serine Protease Factor VIIa (Coagulation Cascadealanine Scanning Mutagenesis)*; 1996.

(100) Paramonov, S. E.; Jun, H. W.; Hartgerink, J. D. Self-Assembly of Peptide-Amphiphile Nanofibers: The Roles of Hydrogen Bonding and Amphiphilic Packing. *J. Am. Chem. Soc.* **2006**. https://doi.org/10.1021/ja060573x.

(101) Yaron, A.; Naider, F.; Scharpe, S. Proline-Dependent Structural and Biological Properties of Peptides and Proteins. *Crit. Rev. Biochem. Mol. Biol.* **1993**. https://doi.org/10.3109/10409239309082572.

(102) Piela, L.; Nemethy, G.; Harold, A. Proline-Induced Constraints in a-Helices. *Biopolymers* **1987**.

(103) Egner, T. K.; Naik, P.; Nelson, N. C.; Slowing, I. I.; Venditti, V. Mechanistic Insight into Nanoparticle Surface Adsorption by Solution NMR Spectroscopy in an Aqueous Gel. *Angew. Chemie - Int. Ed.* **2017**. https://doi.org/10.1002/anie.201704471.

(104) Davies, E.; Huang, Y.; Harper, J. B.; Hook, J. M.; Thomas, D. S.; Burgar, I. M.; Lillford, P. J. Dynamics of Water in Agar Gels Studied Using Low and High Resolution 1H NMR Spectroscopy. *Int. J. Food Sci. Technol.* **2010**. https://doi.org/10.1111/j.1365-2621.2010.02448.x.

(105) Angulo, J.; Enríquez-Navas, P. M.; Nieto, P. M. Ligand-Receptor Binding Affinities from Saturation Transfer Difference (STD) NMR. *Chem. - A Eur. J.* **2010**. https://doi.org/10.1002/chem.200903528.

(106) Maity, S.; Gundampati, R. K.; Kumar, T. K. S. NMR Methods to Characterize Protein-Ligand Interactions. *Natural Product Communications*. 2019. https://doi.org/10.1177/1934578X19849296.

(107) Mumenthaler, C.; Güntert, P.; Braun, W.; Wüthrich, K. Automated Combined Assignment of NOESY Spectra and Three-Dimensional Protein Structure Determination. *J. Biomol. NMR* **1997**. https://doi.org/10.1023/A:1018383106236.

(108) Satake, M.; Ishida, S.; Yasumoto, T.; Murata, M.; Utsumi, H.; Hinomoto, T. Structural Confirmation of Maitotoxin Based on Complete 13C NMR Assignments and the Three-Dimensional PFG NOESY-HMQC Spectrum. *J. Am. Chem. Soc.* **1995**. https://doi.org/10.1021/ja00131a032.

(109) Jee, J. G.; Güntert, P. Influence of the Completeness of Chemical Shift Assignments on

NMR Structures Obtained with Automated NOE Assignment. *J. Struct. Funct. Genomics* **2003**. https://doi.org/10.1023/A:1026122726574.

(110) Cavalli, A.; Salvatella, X.; Dobson, C. M.; Vendruscolo, M. Protein Structure Determination from NMR Chemical Shifts. *Proc. Natl. Acad. Sci. U. S. A.* **2007**. https://doi.org/10.1073/pnas.0610313104.

(111) Nilges, M. Calculation of Protein Structures with Ambiguous Distance Restraints. Automated Assignment of Ambiguous NOE Crosspeaks and Disulphide Connectivities. *J. Mol. Biol.* **1995**. https://doi.org/10.1006/jmbi.1994.0053.

(112) Schmidt, E.; Güntert, P. Reliability of Exclusively NOESY-Based Automated Resonance Assignment and Structure Determination of Proteins. *J. Biomol. NMR* **2013**. https://doi.org/10.1007/s10858-013-9779-x.

(113) Ingram, R. T.; Clarke, B. L.; Fisher, L. W.; Fitzpatrick, L. A. Distribution of Noncollagenous Proteins in the Matrix of Adult Human Bone: Evidence of Anatomic and Functional Heterogeneity. *J. Bone Miner. Res.* **1993**. https://doi.org/10.1002/jbmr.5650080902.

(114) Simes, D. C.; Williamson, M. K.; Schaff, B. J.; Gavaia, P. J.; Ingleton, P. M.; Price, P. A.; Cancela, M. L. Characterization of Osteocalcin (BGP) and Matrix Gla Protein (MGP) Fish Specific Antibodies: Validation for Immunodetection Studies in Lower Vertebrates. *Calcif. Tissue Int.* **2004**. https://doi.org/10.1007/s00223-003-0079-4.

(115) Hoang, Q. Q.; Sicheri, F.; Howard, A. J.; Yang, D. S. C. Bone Recognition Mechanism of Porcine Osteocalcin from Crystal Structure. *Nature* **2003**, *425* (6961), 977–980. https://doi.org/10.1038/nature02079.

(116) Gundberg, C. M.; Anderson, M.; Dickson, I.; Gallop, P. M. "Glycated" Osteocalcin in Human and Bovine Bone. The Effect of Age. *J. Biol. Chem.* **1986**.

(117) Hauschka, P. V.; Frenkel, J.; DeMuth, R.; Gundberg, C. M. Presence of Osteocalcin and Related Higher Molecular Weight 4-Carboxyglutamic Acid-Containing Proteins in Developing Bone. *J. Biol. Chem.* **1983**.

(118) Ferron, M.; Wei, J.; Yoshizawa, T.; Del Fattore, A.; DePinho, R. A.; Teti, A.; Ducy, P.; Karsenty, G. Insulin Signaling in Osteoblasts Integrates Bone Remodeling and Energy Metabolism. *Cell* **2010**. https://doi.org/10.1016/j.cell.2010.06.003.

(119) Lee, N. K.; Sowa, H.; Hinoi, E.; Ferron, M.; Ahn, J. D.; Confavreux, C.; Dacquin, R.; Mee, P. J.; McKee, M. D.; Jung, D. Y.; Zhang, Z.; Kim, J. K.; Mauvais-Jarvis, F.; Ducy, P.; Karsenty, G. Endocrine Regulation of Energy Metabolism by the Skeleton. *Cell* **2007**. https://doi.org/10.1016/j.cell.2007.05.047.

(120) Oury, F.; Sumara, G.; Sumara, O.; Ferron, M.; Chang, H.; Smith, C. E.; Hermo, L.; Suarez, S.; Roth, B. L.; Ducy, P.; Karsenty, G. Endocrine Regulation of Male Fertility by the Skeleton. *Cell* **2011**. https://doi.org/10.1016/j.cell.2011.02.004.

(121) Ferron, M.; McKee, M. D.; Levine, R. L.; Ducy, P.; Karsenty, G. Intermittent Injections of Osteocalcin Improve Glucose Metabolism and Prevent Type 2 Diabetes in Mice. *Bone* **2012**. https://doi.org/10.1016/j.bone.2011.04.017.

(122) Zoch, M. L.; Clemens, T. L.; Riddle, R. C. New Insights into the Biology of Osteocalcin. *Bone*. 2016, pp 42–49. https://doi.org/10.1016/j.bone.2015.05.046.

(123) Dowd, T. L.; Rosen, J. F.; Li, L.; Gundberg, C. M. The Three-Dimensional Structure of Bovine Calcium Ion-Bound Osteocalcin Using 1H NMR Spectroscopy. *Biochemistry* **2003**, *42* (25), 7769–7779. https://doi.org/10.1021/bi034470s.

(124) Scudeller, L. A.; Srinivasan, S.; Rossi, A. M.; Stayton, P. S.; Drobny, G. P.; Castner, D.

G. Orientation and Conformation of Osteocalcin Adsorbed onto Calcium Phosphate and Silica Surfaces. *Biointerphases* **2017**, *12* (2), 02D411. https://doi.org/10.1116/1.4983407.

(125) Ellingsen, J. E. A Study on the Mechanism of Protein Adsorption to TiO2. *Biomaterials* **1991**. https://doi.org/10.1016/0142-9612(91)90057-H.

(126) Alamdari, S.; Pfaendtner, J. Impact of Glutamate Carboxylation in the Adsorption of the α-1 Domain of Osteocalcin to Hydroxyapatite and Titania. *Mol. Syst. Des. Eng.* **2020**. https://doi.org/10.1039/c9me00158a.

(127) Fernandez, V. L.; Reimer, J. A.; Denn, M. M. Magnetic Resonance Studies of Polypeptides Adsorbed on Silica and Hydroxyapatite Surfaces. *J. Am. Chem. Soc.* **1992**, *114* (24), 9634–9642. https://doi.org/10.1021/ja00050a051.

(128) Shir, I. Ben; Kababya, S.; Amitay-Rosen, T.; Balazs, Y. S.; Schmidt, A. Molecular Level Characterization of the Inorganic-Bioorganic Interface by Solid State NMR: Alanine on a Silica Surface, a Case Study. *J. Phys. Chem. B* **2010**. https://doi.org/10.1021/jp100114v.

(129) Weidner, T.; Dubey, M.; Breen, N. F.; Ash, J.; Baio, J. E.; Jaye, C.; Fischer, D. A.; Drobny, G. P.; Castner, D. G. Direct Observation of Phenylalanine Orientations in Statherin Bound to Hydroxyapatite Surfaces. *J. Am. Chem. Soc.* **2012**. https://doi.org/10.1021/ja301711w.

(130) Schweitzer-Stenner, R.; Toal, S. E. Anticooperative Nearest-Neighbor Interactions between Residues in Unfolded Peptides and Proteins. *Biophys. J.* **2018**. https://doi.org/10.1016/j.bpj.2018.01.022.

(131) Jha, A. K.; Colubri, A.; Zaman, M. H.; Koide, S.; Sosnick, T. R.; Freed, K. F. Helix, Sheet, and Polyproline II Frequencies and Strong Nearest Neighbor Effects in a Restricted Coil Library. *Biochemistry* **2005**. https://doi.org/10.1021/bi0474822.

APPENDIX A

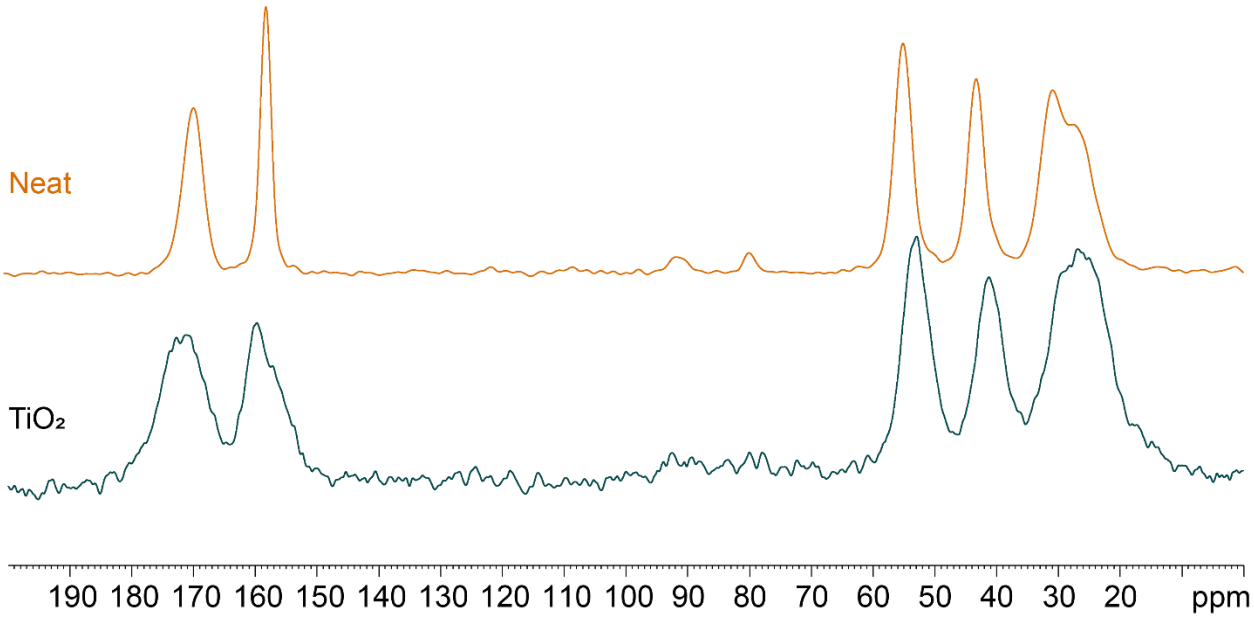

Figure A-1. Stacked 1D spectra of TBP-R neat (orange) and adsorbed to titania (green)

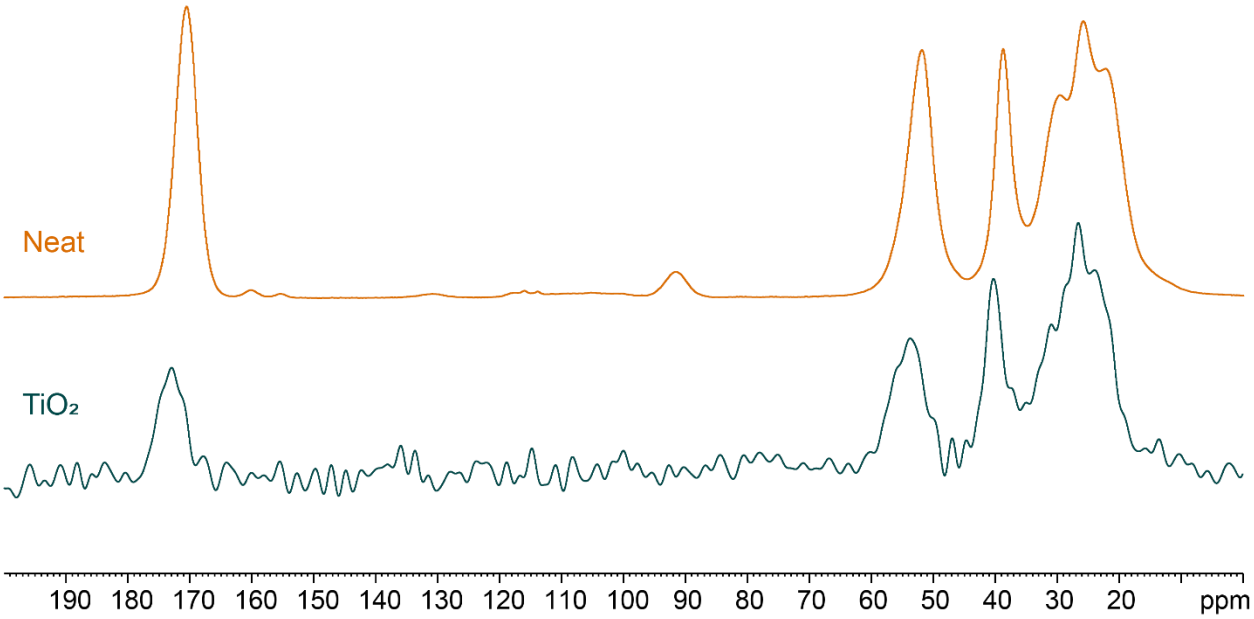

Figure A-2. Stacked 1D spectra of TBP-K neat (orange) and adsorbed to titania (green)

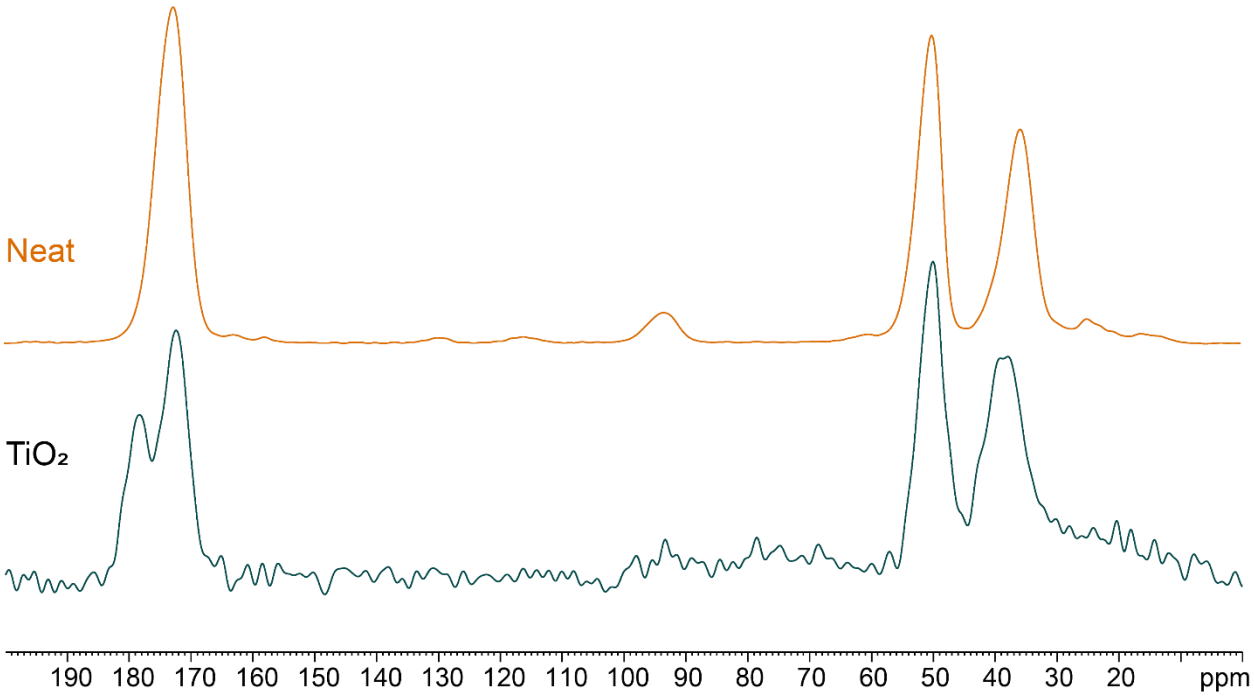

Figure A-3. Stacked 1D spectra of TBP-D neat (orange) and adsorbed to titania (green)

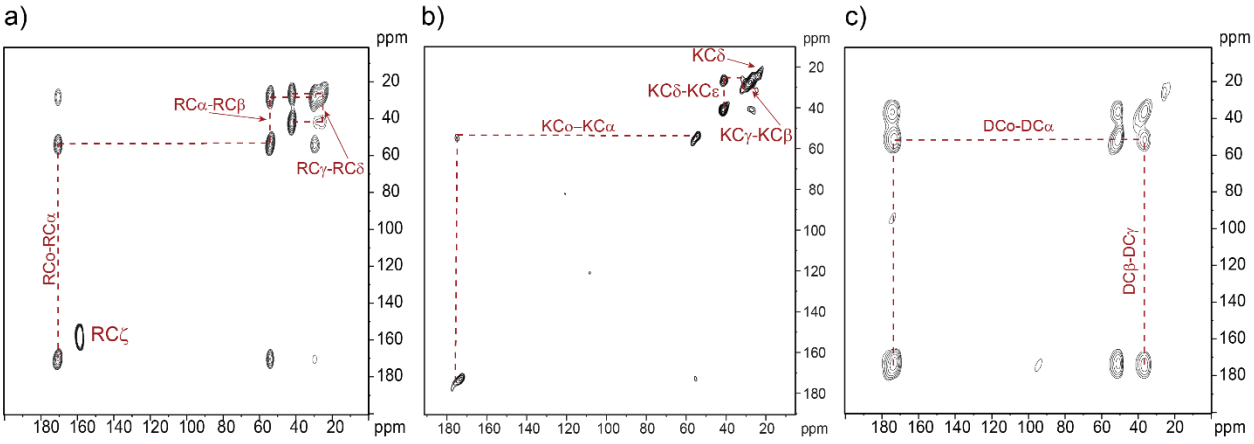

Figure A-4. 13C-13C DARR spectra of a) TBP-R, b) TBP-K, and c) TBP-D neat.

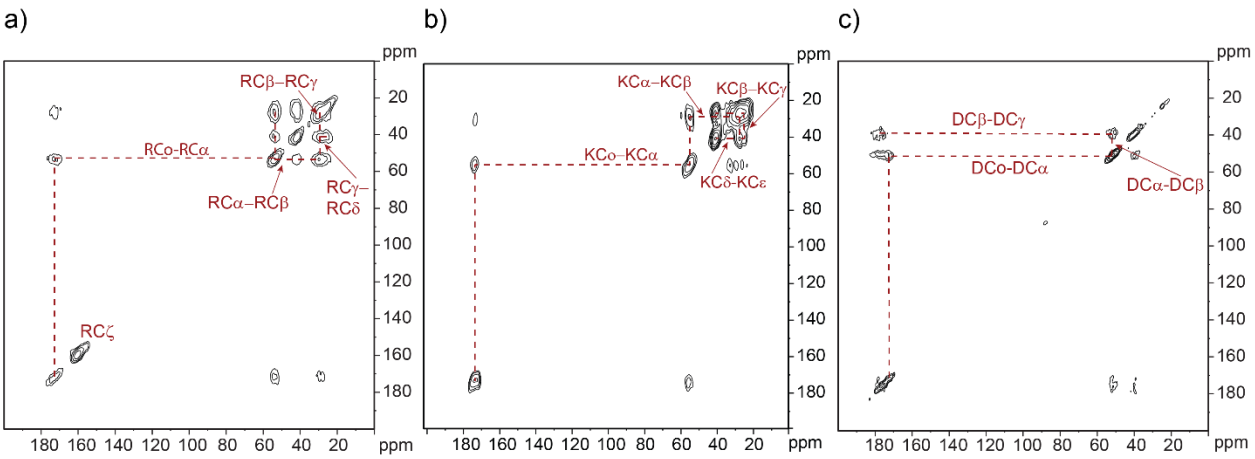

Figure A-5. 2D ^{13}C-^{13}C DARR spectra of a) TBP-R, b) TBP-K, and c) TBP-D adsorbed to titania nanoparticles.

Table A-1. ^{13}C backbone chemical shift assignments for neat TBP (ppm)

Residue	CO	Cα	Cβ
R1	169.8	53.6	27.3
K2	173.2	53.8	31.3
D5	172.9	50.5	35.8

Table A-2. ^{13}C backbone chemical shift assignments for TBP bound to TiO_2 (ppm)

Residue	CO	Cα	Cβ
R1	172.2	53.9	27.8
K2	173.6	55.1	29.1
D5	173.9	50.3	41.6

Table A-3. ^{13}C sidechain chemical shift assignments for neat TBP (ppm)

Residue	Cγ	Cδ	Cε	Cζ
R1	**26.6**	**41.8**	**--**	**158.3**
K2	**23.8**	**27.2**	**40.5**	**--**
D5	**173.7**	**--**	**--**	**--**

Table A-4. ^{13}C sidechain chemical shift assignments for TBP bound to TiO_2 (ppm)

Residue	Cγ	Cδ	Cε	Cζ
R1	**26.7**	**42.1**	**--**	**160.3**
K2	**24.8**	**27.3**	**40.9**	**--**
D5	**179.1**	**--**	**--**	**--**

APPENDIX B

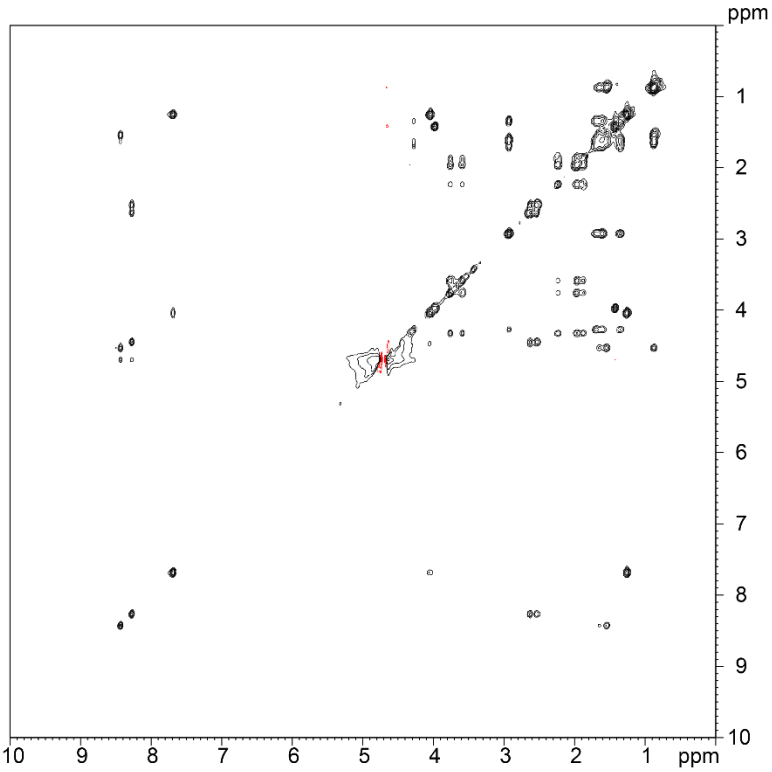

Figure B-1. DIPSI spectrum of TBP-R1A in the presence of titania

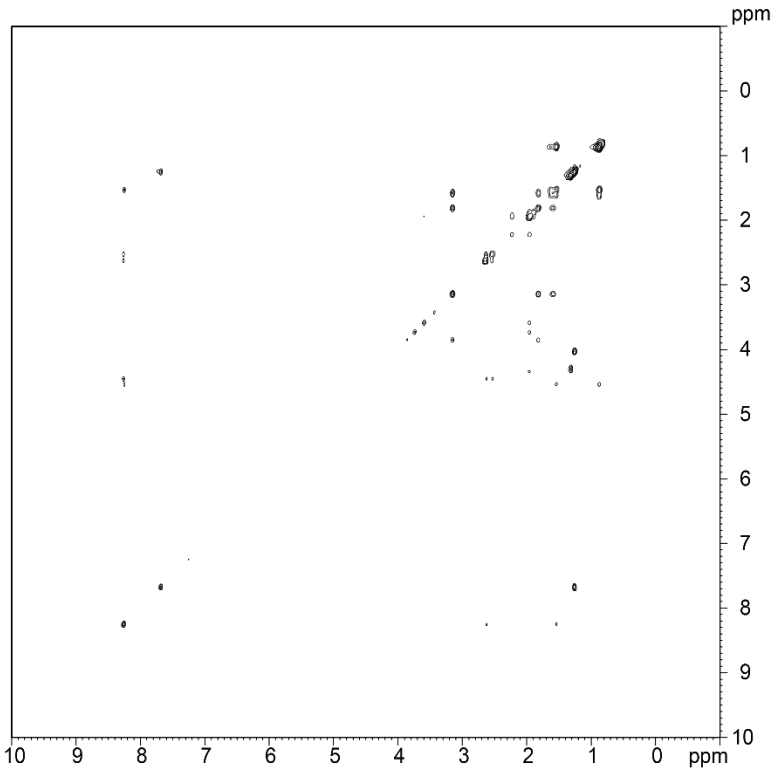

Figure B-2. DIPSI of TBP-K2A

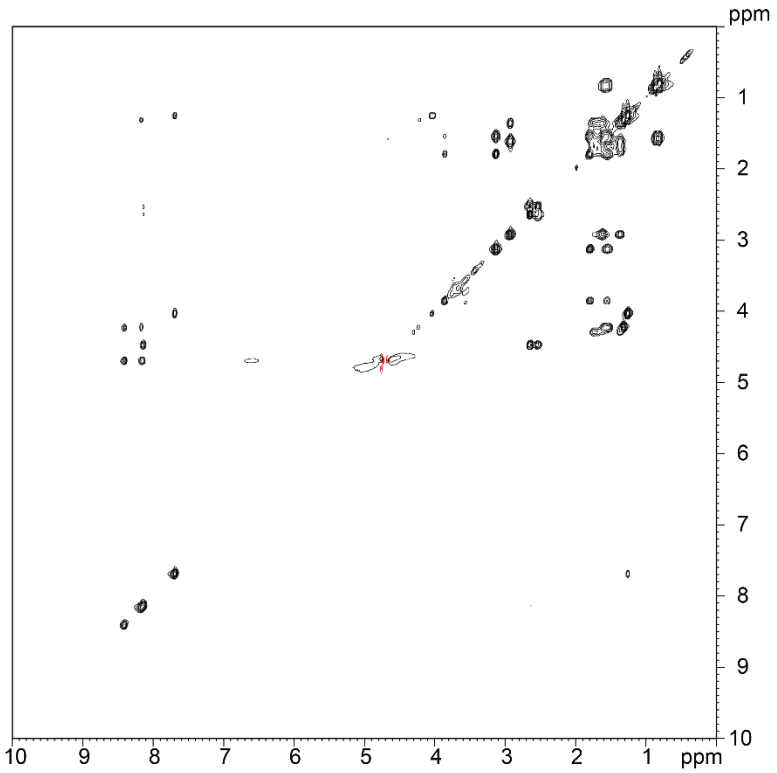

Figure B-3. DIPSI spectrum of TBP-P4A on titania.

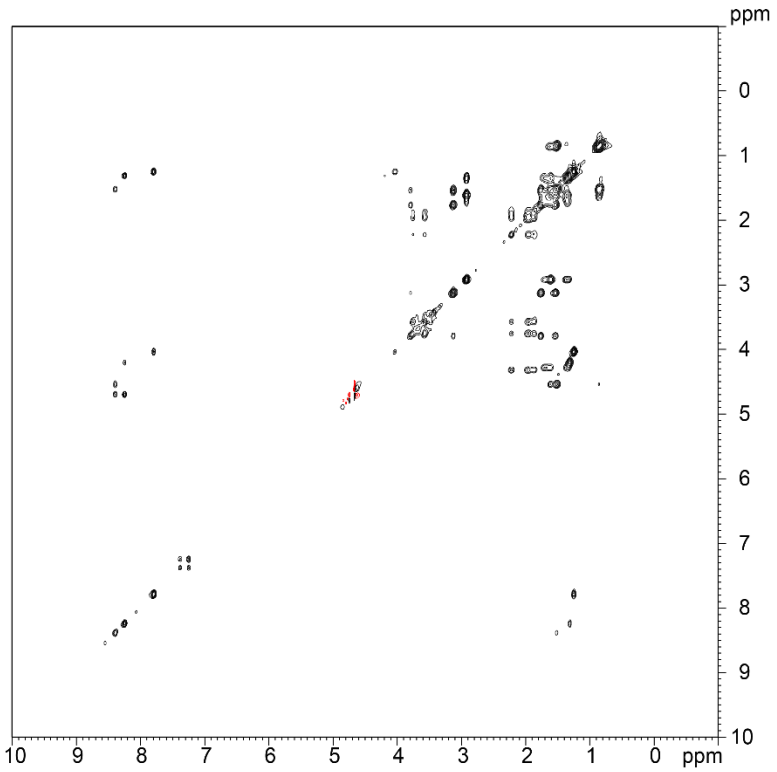

Figure B-4. DIPSI of TBP-D5A

Probably proton chemical shifts

Table B-1. Proton chemical shifts of TBP-R1A.

Residue	^{1}HN	^{1}Hα	^{1}Hβ	^{1}Hγ	^{1}Hδ	^{1}Hε
K2		4.28	1.682	1.352	1.601	2.929
L3			1.536/1.648	1.392	0.72/0.86	
P4	8.06	4.335	2.231	1.91	3.76	
D5	8.30	4.462/4.428	2.526/2.633			
A	7.70	4.048	1.26			

Table B-2. Proton chemical shift assignments of TBP-K2A

Residue	^{1}HN	^{1}Hα	^{1}Hβ	^{1}Hγ	^{1}Hδ
R1	8.25	4.69	1.83	1.6	3.15
L3	8.27	4.548	1.623	1.543	0.87
P4	8.05	4.345	2.223	1.923	3.594/3.741
D5	8.28	4.456	2.621/2.54		

A	7.71	4.035	1.255		

Table B-3. Proton chemical shifts of TBP-P4A neat in solution.

Residue	^{1}HN	^{1}Hα	^{1}Hβ	^{1}Hγ	^{1}Hδ	^{1}Hε
R1	8.42	4.67	1.792	1.547	3.134	
K2		4.30	1.77	1.36	1.62	2.933
L3	8.41	3.86	1.573		0.803/0.865	
D5	8.137	4.47	2.63/2.55			
A	7.70	4.03	1.25			

Table B-4. Proton chemical shift assignments of neat TBP-D5A in solution.

Residue	^{1}HN	^{1}Hα	^{1}Hβ	^{1}Hγ	^{1}Hδ	^{1}Hε
R1	8.40	4.53	1.78	1.54	3.13	
K2	8.41	4.54	1.78	1.36	1.61	2.92
L3	8.40	4.54	1.59	1.37	0.86	
P4			2.22	1.87/1.96	3.57	
A	7.80	4.04	1.25			

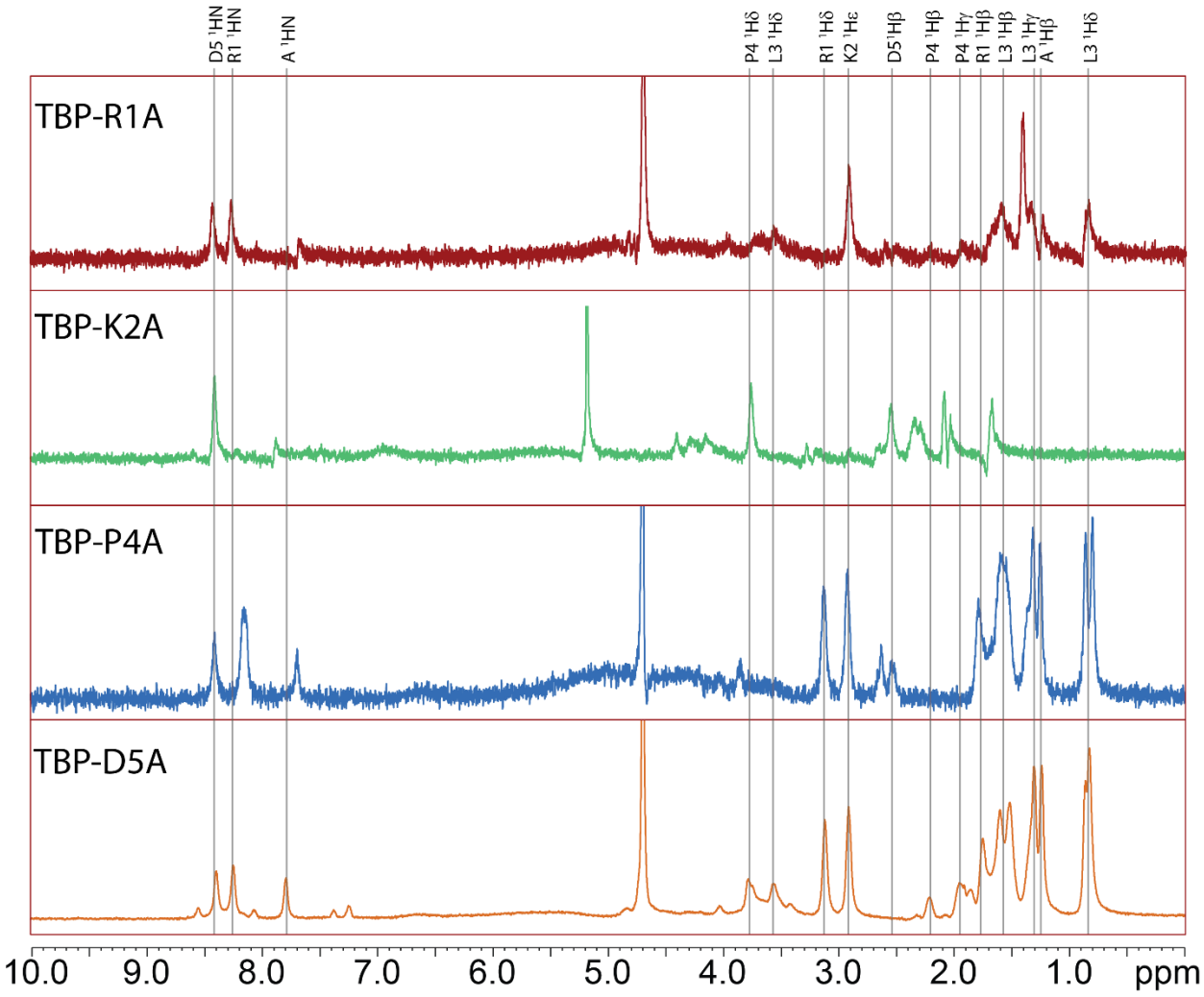

Figure B-5. Stacked STD spectra of mutants prepared in an agarose-titania matrix. The four spectra are shown stacked, and the label of the proton corresponding to the resonance is shown along the top axis and demarcated with a vertical line. Binding interactions often cause a change in chemical shift as discussed at length in Chapter 2, so slight shifts of the resonances is not considered to be a cause for concern. The large peak noticed at 4.7 ppm corresponds to water signal which is not fully dampened by the Watergate suppression method.

Table B-5. A_{STD} for TBP-R1A.

Residue	Observed Proton	A_{STD} Agarose	A_{STD} Agarose + TiO_2	ΔA_{STD}

K2	1He	N/A	0.2405	0.2405
L3	1Hd	0.0013	0.0434	0.0434
P4	1Hd	0.2025	0.01515	-0.0510
D5	1Hb	-0.0369	-0.0168	N/A
A	1Hb	0.0105	0.0598	0.0493

TableB-6. A_{STD} of TBP-K2A

Residue	Observed Proton	A_{STD} Agarose	A_{STD} Agarose + TiO_2	ΔA_{STD}
R1	1Hd	-0.0373	0.2408	0.02408
L3	1Hd	-0.0050	0.0678	0.0678
P4	1Hb	-0.0859	-0.0670	N/A
D5	1Hb	-0.0435	-0.0233	N/A
A	1Hb	0.0093	0.0754	0.0660

Table B-7. A_{STD} of TBP-P4A

Residue	Observed Proton	A_{STD} Agarose	A_{STD} Agarose + TiO_2	ΔA_{STD}
R1	1Hd	0.0315	0.4724	0.4408

K2	1He	0.0367	0.4968	0.4601
L3	1Hd	-0.0078	0.3328	0.3328
D5	1Hb	0.0003	0.2232	0.2228
A	1Hb	-0.0219	0.2892	0.2892

Table B-8. A_{STD} of TBP-D5A

Residue	Observed Proton	A_{STD} Agarose	A_{STD} Agarose + TiO_2	ΔA_{STD}
R1	1Hd	0.0616	0.4004	0.3389
K2	1He	0.0611	0.4613	0.4001
L3	1Hd	0.0122	0.3446	0.3325
P4	1Hb	0.0134	0.1380	0.1246
A	1Hb	-0.0009	0.3359	0.3359

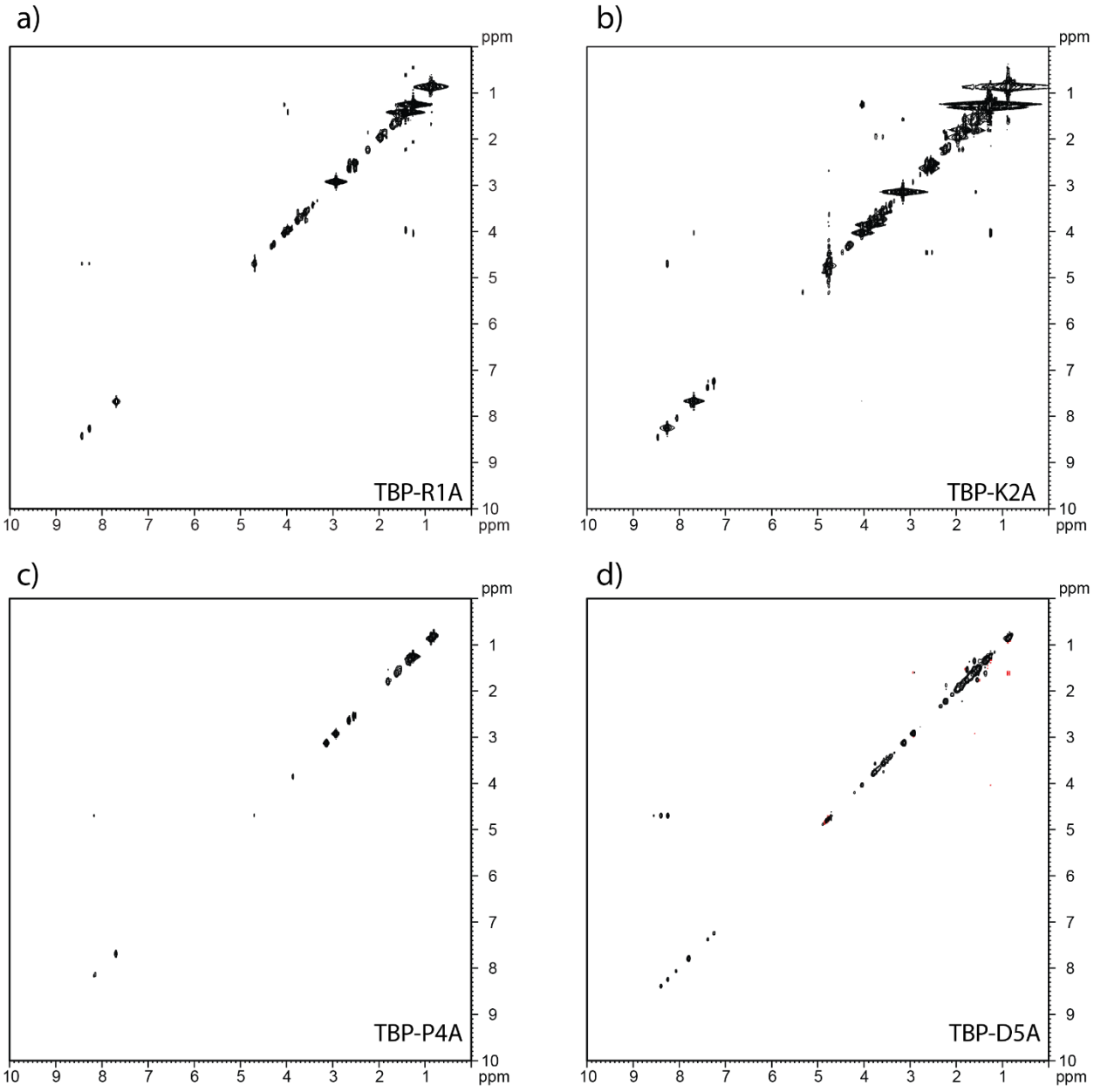

Figure B-6. NOESY spectra of TBP mutants in agarose gel

APPENDIX C

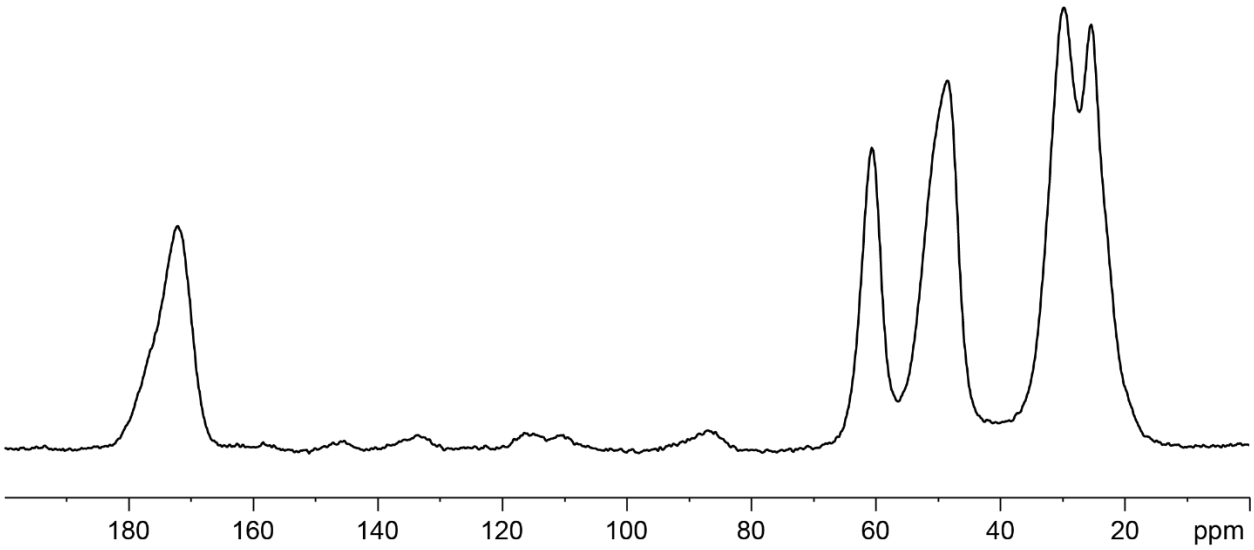

Figure C-1. CP Spectrum of dhOC-α_1-P2E6 neat.

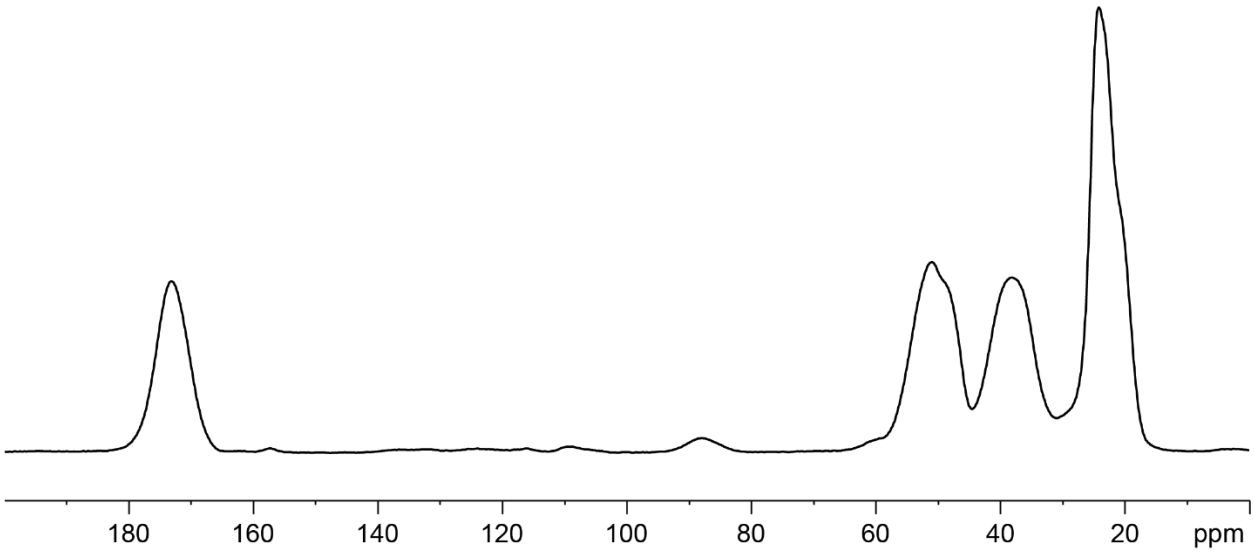

Figure C-2. CP Spectrum of dhOC-α_1-D3L5 neat.

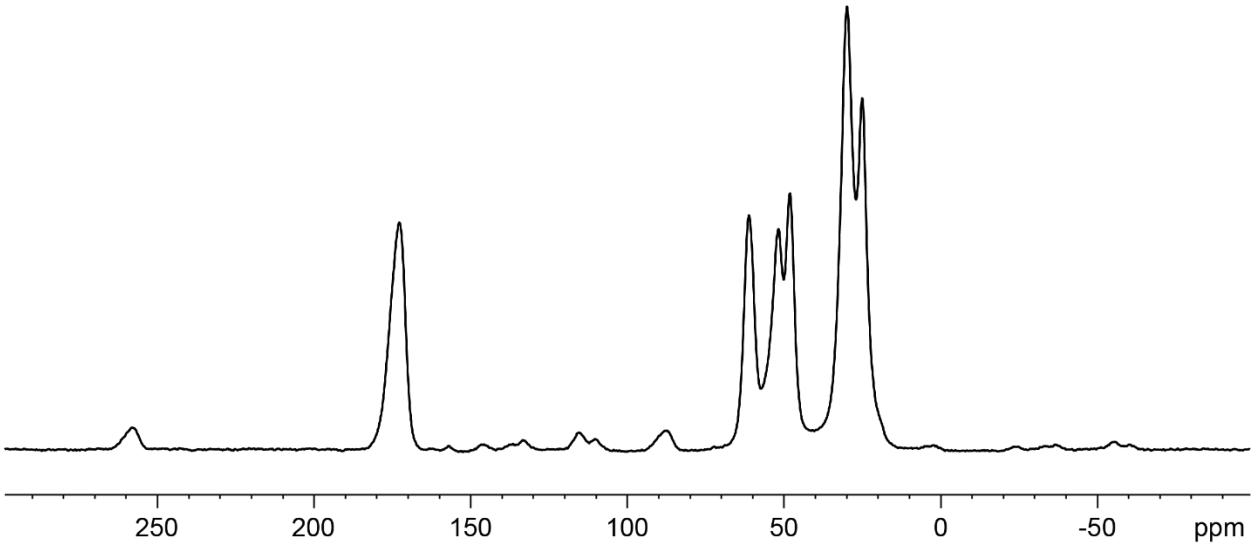

Figure C-3. CP Spectrum of dhOC-α_1-P4E10 neat.

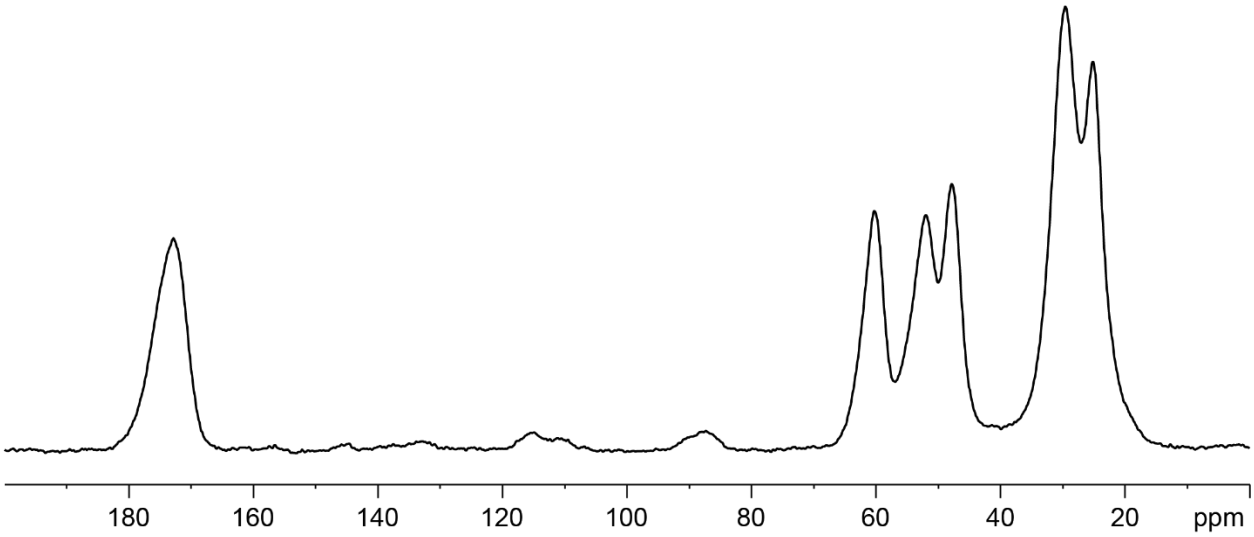

Figure C-4. CP Spectrum of dhOC-α_1-P7E13 neat.

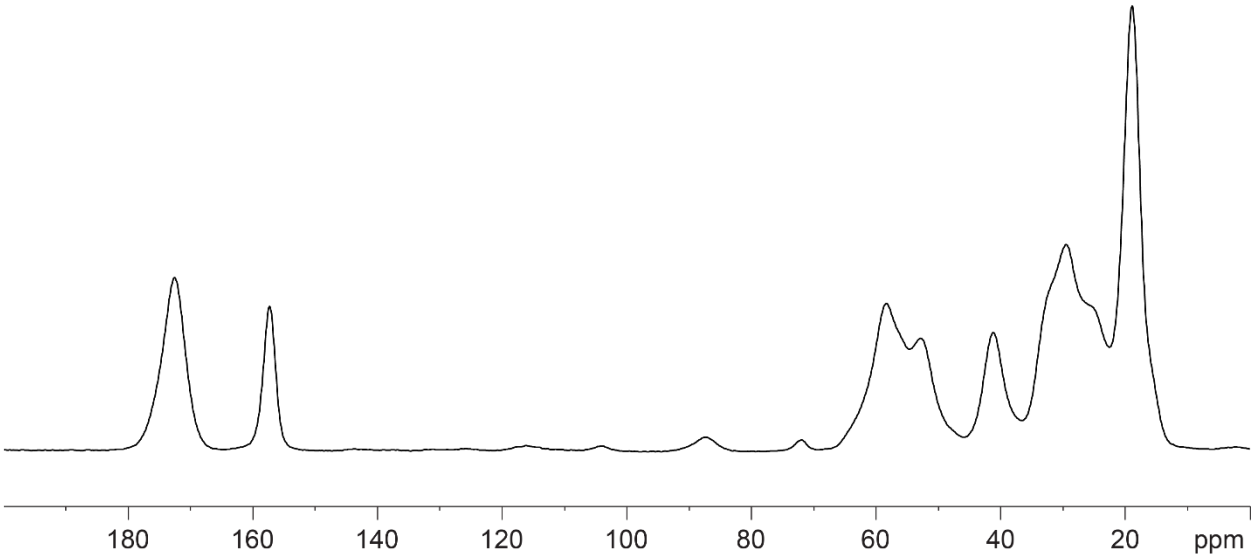

Figure C-5. CP Spectrum of dhOC-α_1-R8V11 neat.

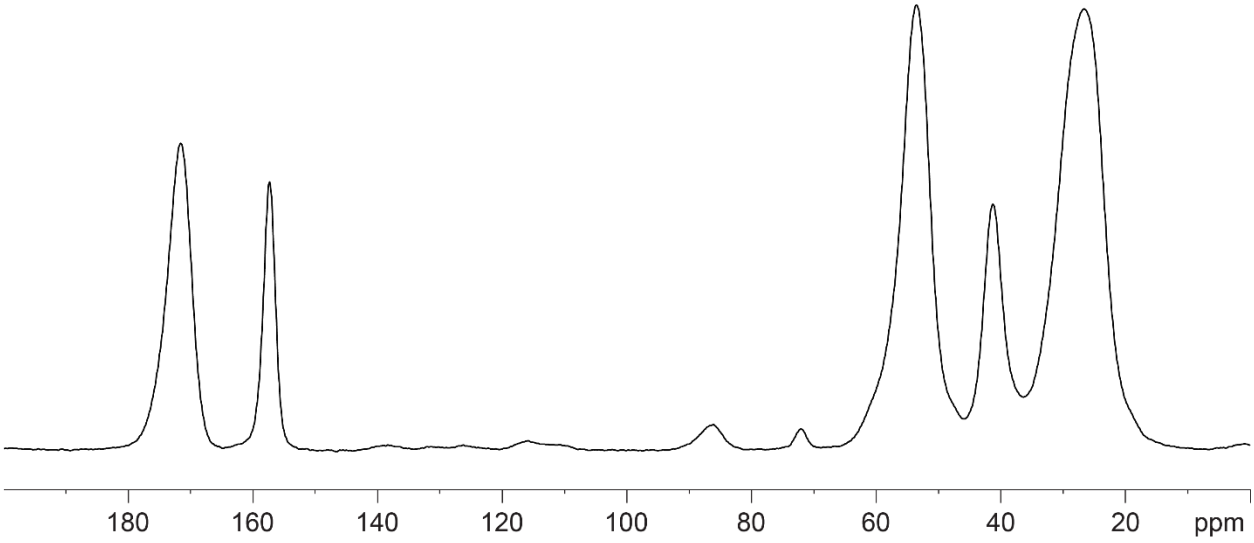

Figure C-6. CP Spectrum of dhOC-α_1-R9C12 neat.

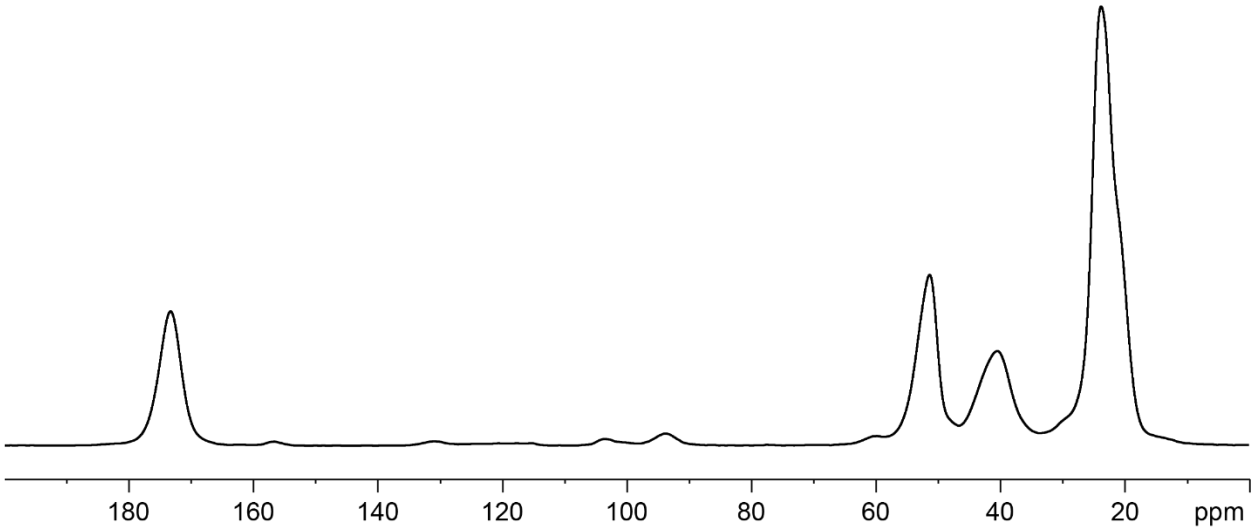

Figure C-7. CP Spectrum of dhOC-α_1-L14 neat.

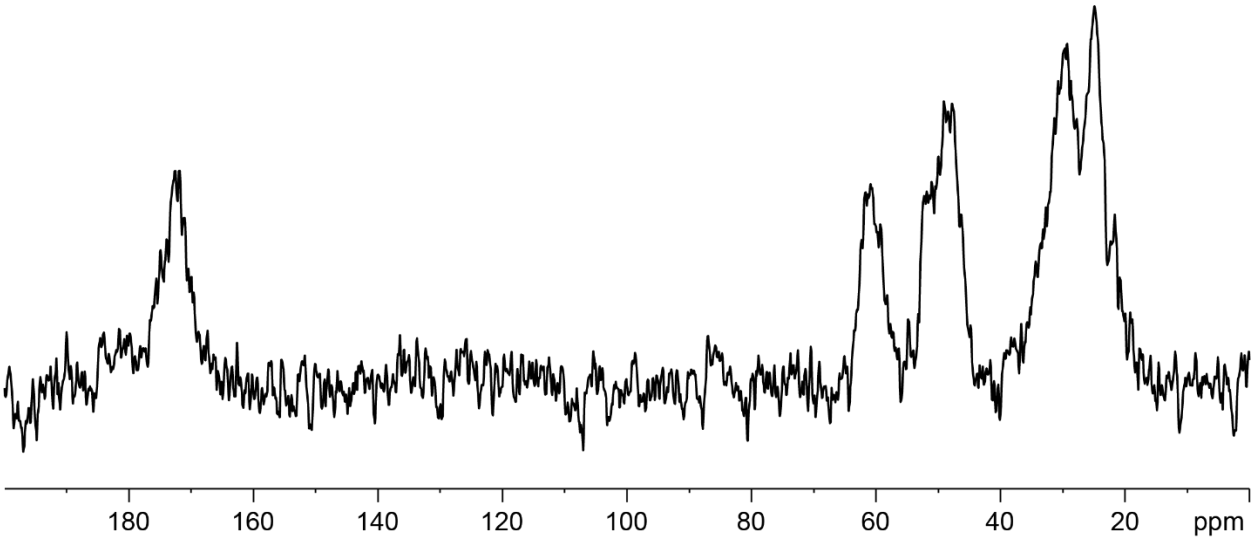

Figure C-8. CP Spectrum of dhOC-α_1-P2E6 mixed with TiO_2.

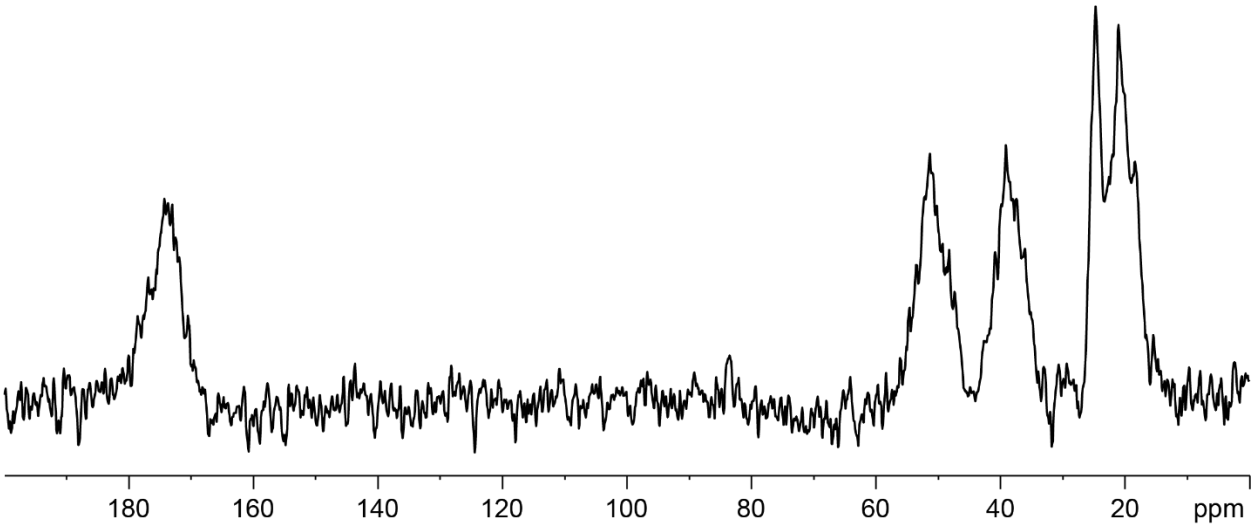

Figure C-9. CP Spectrum of dhOC-α_1-D3L5 mixed with TiO_2.

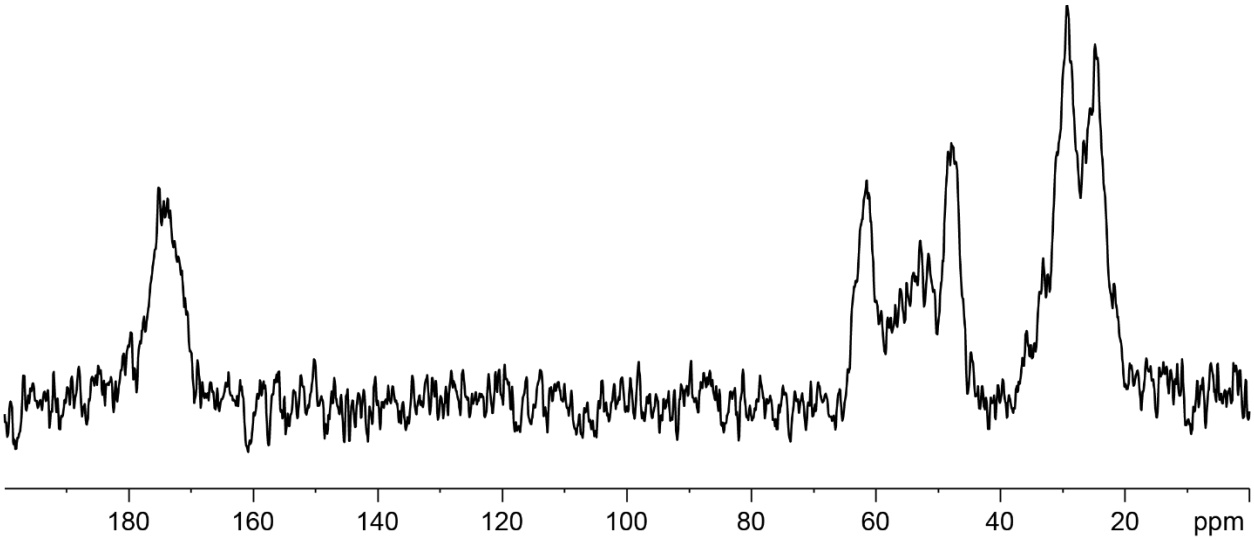

Figure C-10. CP Spectrum of dhOC-α_1-P4E10 mixed with TiO_2.

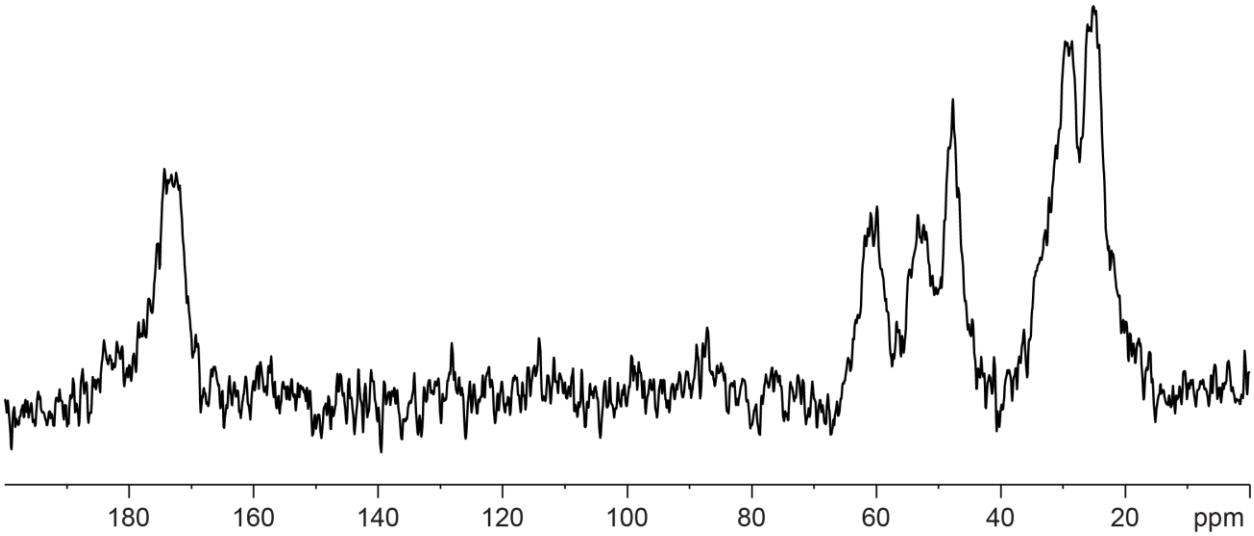

Figure C-11. CP Spectrum of dhOC-α_1-P7E13 mixed with TiO_2.

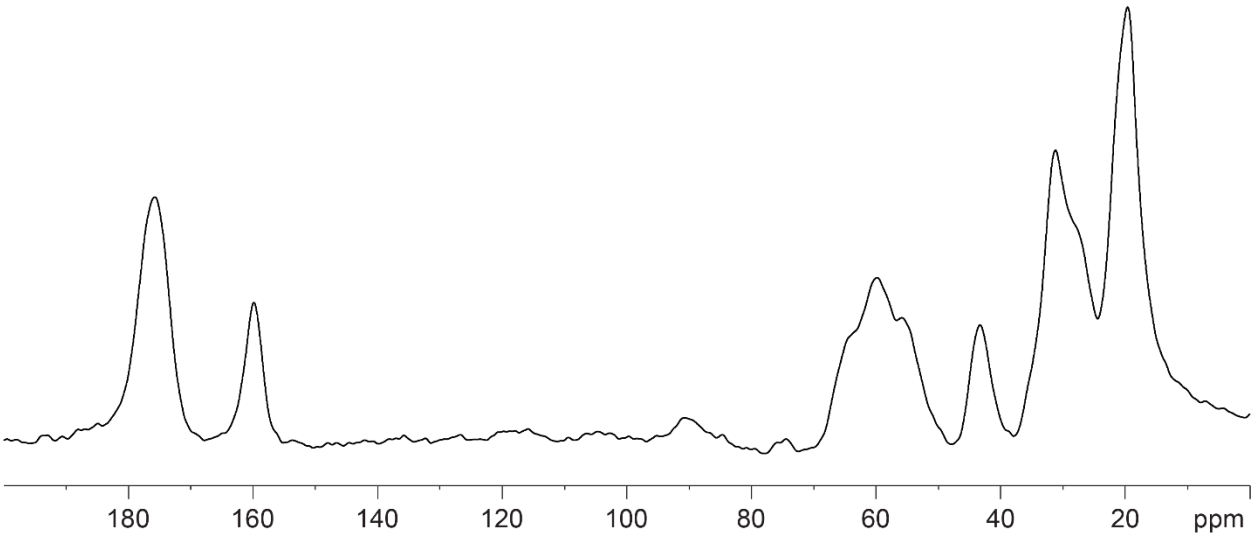

Figure C-12. CP Spectrum of dhOC-α_1-R8V11 mixed with TiO_2.

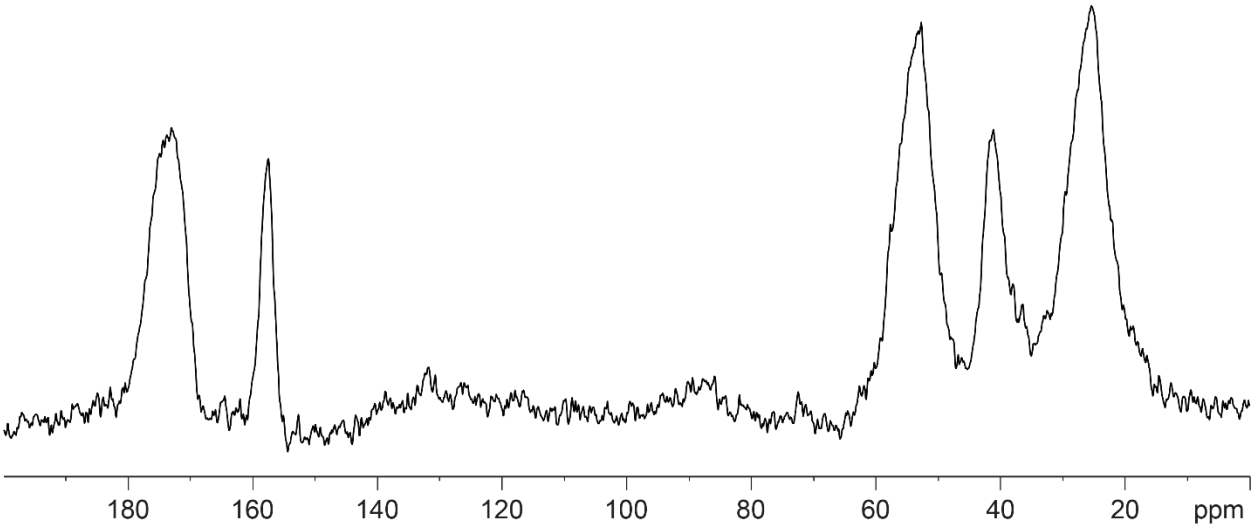

Figure C-13. CP spectrum of dhOC-α_1-R9C12 mixed with TiO_2.

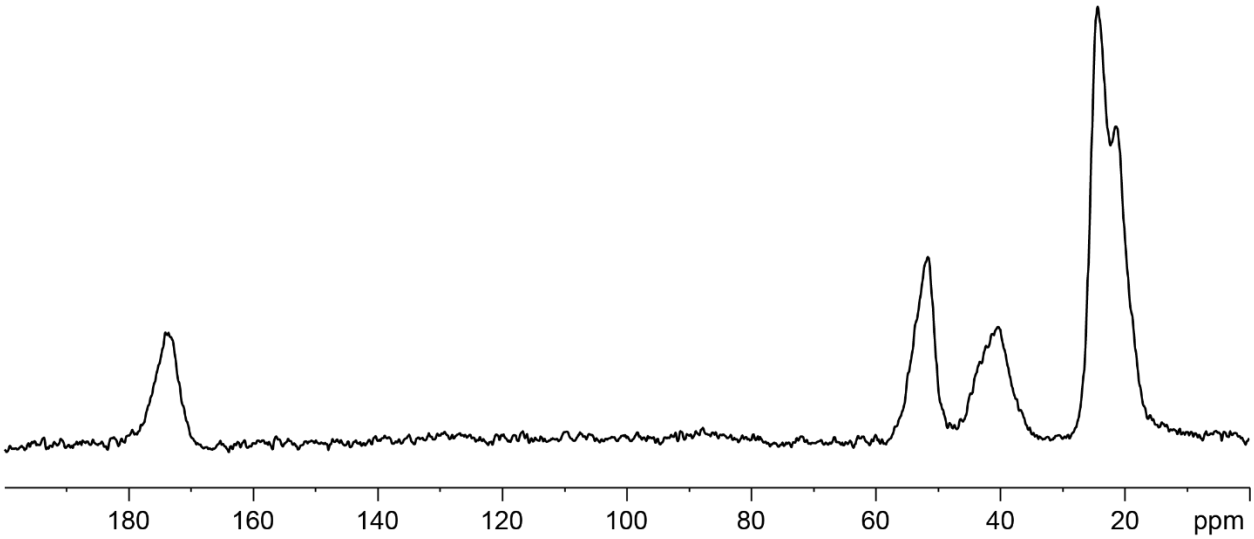

Figure C-14. CP Spectrum of dhOC-α_1-L14 mixed with TiO_2.

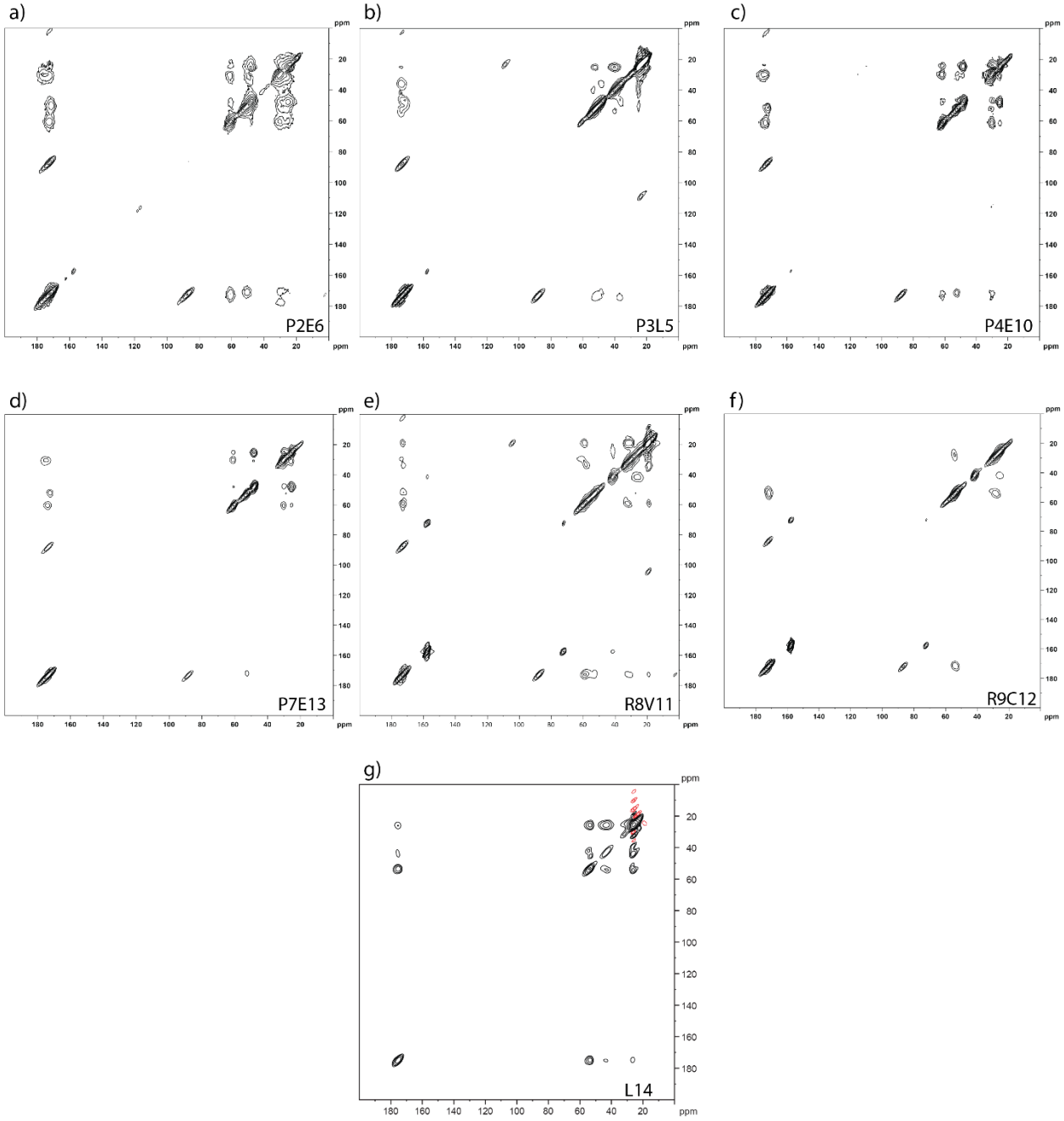

Figure C-15. Neat DARR spectra of dhOC-α_1.

[DARR of dhOC-a1 on TiO2]

Table C-1. ^{13}C backbone chemical shift assignments for neat dhOC-α_1 (ppm)

Residue	Co	Cα	Cβ
P2	172.9	60.7	30.2

D3	171.6	47	36.8
P4	173.8	61.3	29.9
L5	173.8	52.5	40.2
E6	171.4	50.3	29.6
P7	174.1	60	30.5
R8	172.3	53.3	30.1
R9	171.5	54.5	27.2
E10	172.2	51.6	30.8
V11	173	59.1	32.9
C12	171.1	53.5	29.7
E13	172.4	52.2	29
L14	175.4	53.7	45.6

Table C.2. ^{13}C backbone chemical shift assignments for dhOC-α_1 adsorbed to TiO_2 (ppm)

Residue	Co	Cα	Cβ
P2	170.4	59.3	27.9
D3	173.2	50.8	34.4
P4	173.4	60.0	28.7
L5	172.6	48.5	39.7
E6	169.6	59.2	23.5
P7	169.4	48.9	32.1
R8	173.8	51.0	26.8
R9	169.3	51.5	
E10	172.0	61.8	27.3
V11	175.0	61.4	29.6
C12	177.4	52.5	24.9
E13	171.3	59.8	23.6
L14	171.6	49.6	39.6

Table C.3. ^{13}C sidechain chemical shift assignments for neat dhOC-α_1 (ppm)

Residue	Cγ1	Cγ2	Cδ1	Cδ2	Cε	Cζ
P2	24.8	--	47.8	--	--	--
D3	174.1	--	--	--	--	--
P4	24.2	--	47	--	--	--
L5	25.1	25.1	25.1			--
E6	30.5	--	176.3			--
P7	25.5	--	48.1			--
R8	26.2	--	41.7			157.6
R9	25.4	--	41.8			157.7
E10	29.9	--	174.8			--
V11	19.1	--	18.9			--
C12		--				--
E13	31.1	--	175.2			--
L14	25.6	--	32.1	32.1		--

Table C.4. ^{13}C sidechain chemical shift assignments for dhOC-α_1 adsorbed to TiO_2 (ppm)

Residue	Cγ	Cδ	Cε	Cζ
P2	22.3	46.8		
D3	175.3			
P4	21.2	47.6		
L5	22.2	?		
E6	28.6	177		
P7	22.2	46.1		
R8	22	41.4		155.9
R9	22.07	43.3		154.6
E10	41.1	173.9		
V11	16			
C12				
E13	30.5	179.3		
L14	23.2	20.2		

TALOS-N torsion angles

Table C.5. TALOS-N generated torsion angles for neat dhOC-α_1

Residue	ϕ	ψ
D3	-91.5±19.9	134.6±24.7
P4	-66.6±8.3	151.6±10.5
L5	-90.7±18.0	122.8±17.7
E6	-130.8±25.1	113.1±40.8
P7	-68.1±9.8	149.1±13.7
R8	-102.0±26.7	122.8±16.9
R9	-106.6±20.2	126.2±45.5
E10	-119.4±26.4	130.5±19.4
V11	-121.0±14.3	129.5±15.9
C12	-118.2±19.6	137.3±18.9
E13	-123.0±16.0	135.1±21.0
L14	-102.1±23.7	138.8±16.2

Table C.5. TALOS-N generated torsion angles for dhOC-α_1 adsorbed to titania

Residue	ϕ	ψ
D3	-94.011±30.155	134.766±26.295
P4	-63.760±9.496	142.968±13.638
L5	-103.867±26.829	135.159±16.845
E6	48.44±5.421	54.903±5.599
P7	-65.410±6.978	146.270±7.712
R8	-84.901±19.718	129.564±16.835
R9	-84.133±23.233	158.534±75.239
E10	57.035±8.195	41.397±15.444
V11	-97.736±24.009	135.265±20.437

C12	-74.236±21.407	142.297±10.554
E13	59.606±7.440	38.189±11.809
L14	-94.875±8.323	109.633±22.869

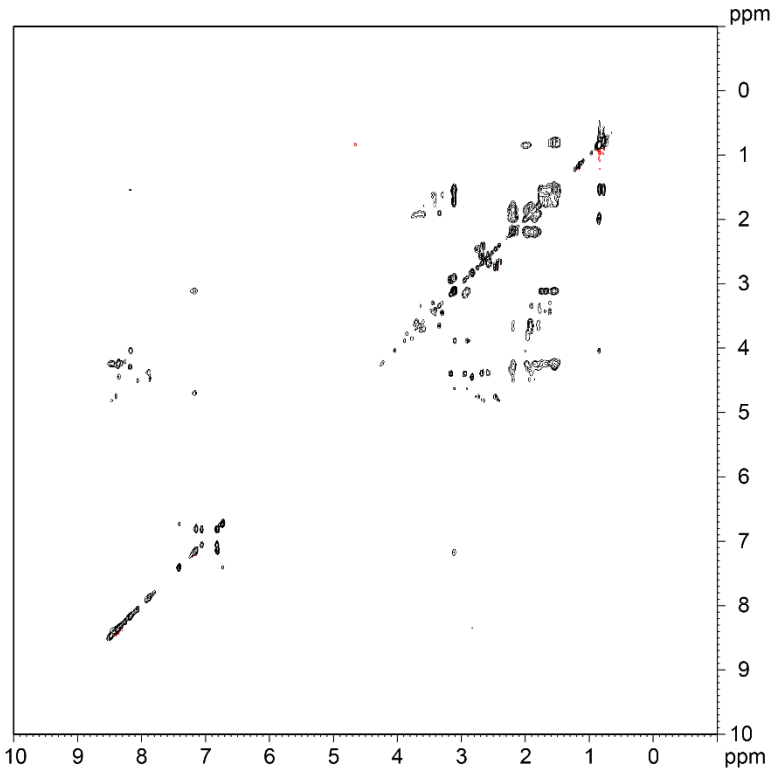

Figure C-17. DIPSI of dhOC-a1 Neat

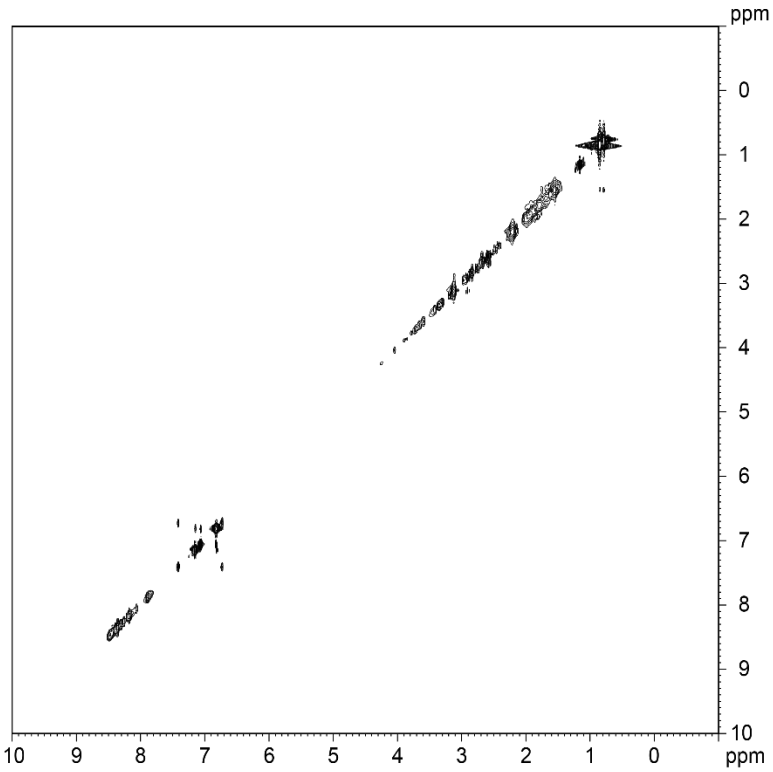

Figure C-18. NOESY of dhOC-a1 Neat

VITA

Rachel Gebhart was born in Huntsville, Alabama, moving to Washington State with her family in grade school. She started college at Franklin W. Olin College of Engineering, before returning to Washington to complete pre-requisites at Bellevue College before transferring to the University of Washington. There she began undergraduate research under Prof. Miqin Zhang, graduated with her B.S. in Chemistry, then began her graduate research with Prof. Gary Drobny. To relax, Rachel enjoys hiking, backpacking, snowshoeing, bouldering, carnicross, and moving livestock around with her dogs.